Order Number 9325166

A search for low-mass short-lived states coupling to the electron and the positron and a study of the single-quantum annihilation of positrons

Wu, XiaoYe, Ph.D.

City University of New York, 1993

U·M·I
300 N. Zeeb Rd.
Ann Arbor, MI 48106

A SEARCH FOR
LOW-MASS SHORT-LIVED STATES
COUPLING TO THE ELECTRON AND THE POSITRON

AND

A STUDY OF
THE SINGLE-QUANTUM ANNIHILATION OF POSITRONS

by

XiaoYe Wu

A dissertation submitted to the Graduate Faculty in Physics in partial fulfillment of the requirement for the degree of Doctor of Philosophy, The City University of New York

1993

This manuscript has been read and accepted for the Graduate Faculty in Physics in satisfaction of the dissertation requirement for the degree of Doctor of Philosophy.

March 5, 1993
Date

Leonard. O. Roellig Leonard O. Roellig
Chair of Examining Committee

March 16, 1993
Date

Joseph B. Krieger Joseph B. Krieger
Executive Officer

Kelvin G. Lynn Kelvin G. Lynn

Michael S. Lubell

Marvin H. Mittleman Marvin H. Mittleman

Carl M. Shakin Carl Shakin

Supervisory Committee

The City University of New York

ABSTRACT

A SEARCH FOR LOW-MASS SHORT-LIVED STATES COUPLING TO e^+e^- AND A STUDY OF THE SINGLE-QUANTUM ANNIHILATION OF POSITRONS

by

XiaoYe Wu

Advisors: Dr. Kelvin G. Lynn and Prof. L. O. Roellig

Two experiments performed at Brookhaven National Laboratory, using a 3 MeV energy-tunable, mono-energetic positron beam, are described in this thesis.

i) **A Search for Low-Mass Short-Lived States Coupling to e^+e^-.** The experimental search for a previously unobserved light neutral particle in the mass (1560 keV $\lesssim M_{X^0} \lesssim$ 1860 keV) — lifetime ($\tau \lesssim 3.5 \times 10^{-13}$ sec) region was motivated by the observations of anomalous mono-energetic e^+ and e^- emissions in heavy-ion atom collisions near the Coulomb barrier at Gesellschaft für Schwerionenforschung (GSI), Germany. Resonances in the Bhabha (e^+e^-) scattering cross section have been investigated in the beam energy range 1350 to 2350 keV. A thin ($\sim$ 3 keV energy loss) lithium target was used to achieve a minimum electron-momentum spread to enhance the resonance signal. The detector system employed in this experiment consisted of multi-wire proportional chambers (MWPC's) and plastic scintillators for the complete kinematic reconstruction of the e^+e^-scattering events. Within experimental uncertainties (0.27 %), no evidence was observed for deviations from the smooth Bhabha scattering cross section, over the energy region suggested by the GSI data. On average, this experiment precludes at 90% confidence level the existence of an elementary or a composite particle ($J = 0$) with a lifetime shorter than 3.3×10^{-13} sec.

ii) **Single-Quantum Annihilation of Positrons with Shell-Bound Atomic**

Electrons. The single-quantum annihilation of positrons was studied experimentally in a thin lead target (3.52 mg/cm^2), at energies of 1 MeV and higher. Photo-peaks corresponding to the annihilation of the incident positrons with K, L, and M shell electrons were resolved and observed clearly for the first time. The cross section ratios L/K and M/K were determined. An analysis of the L peak profile yielded the $(L_{II} + L_{III})/L$ ratio. The first measurements were also made of the directional distribution of the annihilation quanta of the three individual electron shells. The results were in good agreement with theory. These observations indicate the potential for applying the phenomenon to the development of a tunable, highly directional gamma-ray source.

Acknowledgements

I would like to give my appreciation to my advisors Dr. K.G. Lynn and Prof. L.O. Roellig for their invaluable advise throughout a number of experiments that I was involved in, as well as their help in solving problems that I encountered in the past four years. I want to express my deep gratitude to Prof. J.S. Greenberg for his insightful guidance throughout the course of the experiment searching for the resonance in the e^+e^- scattering and his great effort of making this project successful. I thank the rest members of the committee, Prof. M.S. Lubell, Prof. M.H. Mittleman, Prof. C.M. Shakin, for their careful reading of the manuscript and helpful comments. I had a beneficial experience working in the positron group at Brookhaven National Laboratory and truly enjoyed the academic environment provided by the people in the group. I will certainly miss working with them.

I would like to thank Dr. S.D. Henderson, Dr. P. Asok-kumar, Dr. B.F. Phlips, and Prof. J.C. Palathingal for important discussions and suggestions on the experiment. Also, I appreciate H. Hacker for his technical support and valuable friendship.

I want to express my deepest appreciation to my wife Hongbin Ge for her love and continuous support, and my daughter Ann Wu for bringing me a great joy. I am grateful to my parents for their invaluable help in my academic years.

Thank God!

Preface

Two topics are presented in this thesis.

In part 1, an experiment performed at Brookhaven National Laboratory, using the Dynamitron accelerator to search for a previously unobserved neutral particle, is discussed. This experiment started in 1988, after the successful construction of a 3-MeV positron beam, and was finished in the summer of 1990. There were two stages to this experiment. The first stage, which was described in the Ph.D thesis of S.D. Henderson, Yale university, 1991, was aimed at exploring the long-lived resonance states of e^+e^- by utilizing an active target to suppress the non-resonant Bhabha background for extended lifetime sensitivity. The second stage searched for short-lived states, employing a thin lithium target. The latter experiment will be the main topic of this thesis. With these two experiments, most of the open regions in mass-lifetime for the existence of this hypothetical particle, suggested by the GSI heavy-ion experiments, have been investigated experimentally.

In part 2, another experiment using the same accelerator to observe the single-quantum annihilation (SQA) of positrons with shell-bound atomic electrons is discussed. This experiment, for the first time, clearly resolved the annihilation photo-peaks from electrons of K, L, and M atomic shells.

The thesis is arranged as following: In chapter 1, the general background of the

heavy-ion experiments at GSI which motivated the search for the e^+e^- resonance states is reviewed. Chapter 2 describes details of the e^+e^- elastic scattering, as well as the experimental apparatus employed and the properties of the positron beam, which played an essential part in accomplishing the research. Chapter 3 discusses the data analysis for extracting the lower limits of lifetimes for this hypothetical particle. Discussion is given at the end of the chapter. In chapter 4, the SQA process and its experimental observation are described, and possible applications of the SQA phenomenon are pointed out.

To my dear wife Hongbin Ge

and my lovely daughter Ann Wu

Contents

List of Tables

List of Figures

Part I

A Search for Low-Mass Short-Lived States Coupling to e^+e^-

Chapter 1

Introduction

1.1 Motivation

Our systematic search for a previously unobserved neutral particle with a mass around 2 MeV was motivated by repeated observations of an anomalous production of sharp positron lines which appeared at a few energies in experiments performed at Gesellschaft für Schwerionenforschung (GSI), Germany, to search for spontaneous positron production in heavy-ion collisions near the Coulomb barrier. Shortly after these observations, it was found that the heavy-ion data were inconsistent with the expected broad spectrum of positrons due to the short-lived supercritical fields produced by the super-heavy nucleus. Two major groups, EPOS and ORANGE, observed nearly identical results, using different experimental setups. The EPOS collaboration consisted of Yale University, GSI, the University of Frankfurt, the University of Mainz and the University of Heidelberg, while the ORANGE collaboration had only two groups, from GSI and T.U. München.

In the latter experiments, these mono-energetic positrons were measured in coincidence with electrons. The results showed several sharp positron-electron sum-energy lines. The source responsible for the spatial and energy-correlated emission of these mono-energetic position-electron pairs could not be identified as spontaneous positron production from the vacuum in the environment of the supercritical field nor could the phenomenon be explained by any conventional physical mechanism. It has remained a puzzle since the first anomalous positron peaks were observed in U+Cm collisions in 1983, with the EPOS spectrometer [Sch83] at GSI, and then also found in other collision systems by both EPOS [Sch85] and ORANGE collaborations [Cle84]. Consequently, the existence of a new particle (this hypothetical low-mass particle will be denoted by X^0), which might be formed during the period of the collision and subsequently decay into e^+e^-outside the Coulomb field of the heavy ions, was proposed. If such a particle existed, the decay of this particle in the C.M. system of heavy-ion collisions would match the kinematics of the e^+e^- pairs found in the experiments.

In view of the implications of the heavy-ion experiments, an experiment was performed at BNL to search for this light neutral object through its time-reversed process. In Chapter 1 to 3 of this thesis, this experiment is discussed in detail.

1.2 The Heavy-ion Experiments

In 1976, the EPOS and ORANGE groups started the experimental exploration of spontaneous positron production, which was predicted to occur in a nuclear system with the combined nuclear charge $Z > 173$ [Gre85]. In such a super-heavy atom with an empty K shell, the K-shell electron binding energy will exceed $2mc^2$, causing the $1s$ energy level to "dive" into the antiparticle continuum (see figure 1.1). Because the energy of such a bound state is more negative than the energy of electrons in the

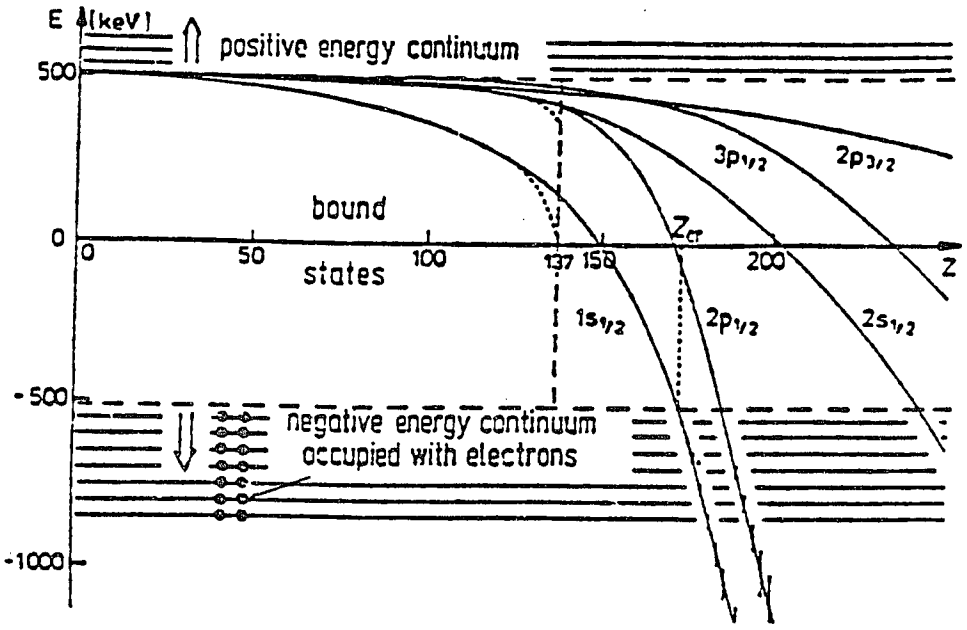

Figure 1.1: Ground state of the Dirac equation for a point-like nucleus. The eigenenergy of the ground state to dive into the Dirac sea when $Z > 173$, reference [Gre85]

Dirac sea, an e^+e^- pair will be created from the vacuum so that the system can move to a lower potential bound state. As a result, the nucleus will capture the electron, and the positron will be expelled from the nucleus by the Coulomb field. Thus, a stable super-heavy atom with a K-shell vacancy will cause the emission of a monoenergetic positron having energy $T_+ = |E_{1s}| - 2mc^2$. However, in nature, atoms with nuclear charge more than 173 do not exist. With modern heavy-ion accelerators, it is possible for these super-heavy atoms to be formed momentarily by bombarding a high Z target with high-energy heavy-ions. If the the two combined nuclei can stay together long enough to induce the spontaneous positron production, the emitted positrons should be observed in the experiment. Hence, the collision of very heavy ions at energies close to the Coulomb barrier constitutes a unique tool with which to study the behavior of the electron-positron field in the presence of strong electromagnetic fields. Such strong electric fields, extending over a sufficiently large region of space, can produce e^+e^- pairs. However, in addition the complexity of the environment in

the heavy-ion collisions, the super-heavy atoms created by heavy ions bombarding a high Z target are unstable. The rapid variation of the strong Coulomb field during the period of the collision will excite the antiparticle continuum. This production process of atomic positrons introduces a broad background in the positron spectrum. Moreover, because the supercritical field exists only transiently during the period of collision, typically with a lifetime of $\tau \simeq 2 \times 10^{-21}$ sec, it is not expected that sharp positron lines would be seen in such a short-lived system. Rather, these candidate positrons will exhibit themselves as a broad structure above the background with a predicted width of $\sim$ 300 keV at a mean energy of a few hundred keV, depending on the combined nuclear charge.

In the first stage of the heavy-ion experiments, the existence of a K vacancy was verified by X-ray characterization, and also, the background positron production due to atomic processes was studied. The first experiment [Sch83] to search for spontaneous pair production was carried out in the U+Cm system with a combined nuclear charge $Z_u = 188$ near the Coulomb barrier. As expected, a structure was observed in the positron spectrum, at an energy of $E_{e^+} = 316 \pm 10$ keV with a width of $\sim$ 80 keV, dominated by Doppler broadening. This narrow line-width was only 1/4 of the theoretical value ($\sim$ 300 keV) for spontaneous positron production, and it suggested that the emitting system had to exist for a time period longer than $\sim 10^{-20}$ sec. The positron line only showed up when certain kinematic cuts (see figure 1.2) in the backward elastic scattering ($100° < \theta_{CM} < 130°$) were applied. This sharp positron peak disappeared when the kinematic cut was made in the forward direction ($50° < \theta_{CM} < 80°$). In fact, considering the possibility of a metastable nuclear complex which would provide such a time delay, this resonant-like sharp positron peak could be the result of spontaneous positron production. Furthermore, the data

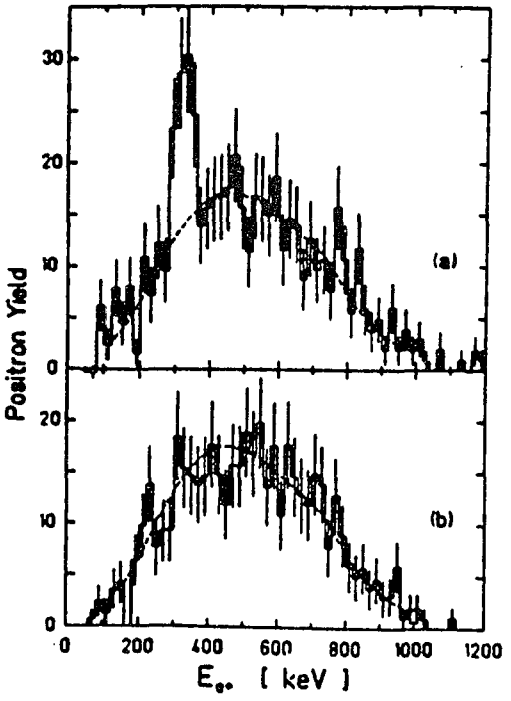

Figure 1.2: First observation of narrow positron line from U + Cm collision at 6.05 MeV/u. Two positron spectrums are shown here with different kinematic cuts: (a) $100° < \theta_{CM} < 130°$ (b) $50° < \theta_{CM} < 80°$. This figure is reproduced from reference [Sch83].

were very convincing because the mean peak energy of the e^+ line coincided with the kinetic energy calculated for spontaneous creation for the U+Cm system. Later, this same line was again observed in the U+U system. This observation was verified by another group [Cle84] in U+U and U+Th collisions.

Initially, the observations made by the EPOS and ORANGE collaborations created a great deal of enthusiasm, mainly because most of the features seen in the heavy-ion experiment were consistent with the interpretation of spontaneous decay of the neutral vacuum into the charged vacuum. Experiments were carried out to measure the e^+ energy dependence on the combined nuclear charge Z_u. The theory predicted that for spontaneous positron emission the energy of the positron had a $\sim Z_u^{20}$ dependence on the nuclear charge. A series of systems, ranging from the sub-critical Th+Ta ($Z_u = 163$) to the supercritical U+Cm system ($Z_u = 188$) were investigated. The results then confused the issue. The narrow positron line appeared in all the collision systems studied, even in the sub-critical Th+Ta system. Besides this unexpected result, surprisingly, no Z_u^{20} dependence was observed (see figure 1.3). Instead, the mean positron peak-energies remained nearly the same in all the systems. This discovery challenged the previously attractive explanation of spontaneous positron production. At this time, it seemed that the mechanism of spontaneous positron creation could not be a candidate for the source of the sharp positron line.

In 1985, the EPOS group made another important discovery which finally led to the particle hypothesis. In their new measurements with a modified detector system, positrons were detected in coincidence with electrons, and the data [Cow86] showed a narrow e^+e^- sum-energy line at 760 keV in the U+Th collision system. The positrons and electrons shared almost the same energy in the heavy-ion CM system. As further studies with improved energy resolution continued [Cow88], another two

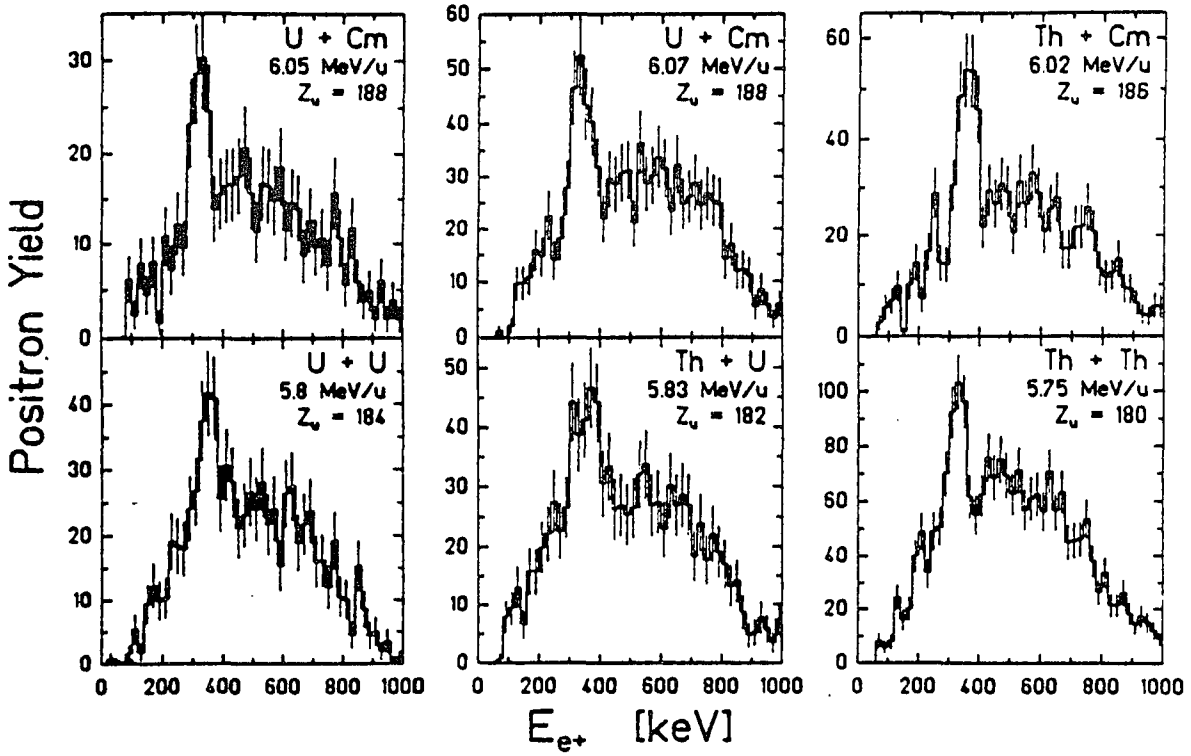

Figure 1.3: Sharp positron peaks showed up in all the six experimental systems. No clear Z_u dependence was observed (Figure reproduced from [Hen88]).

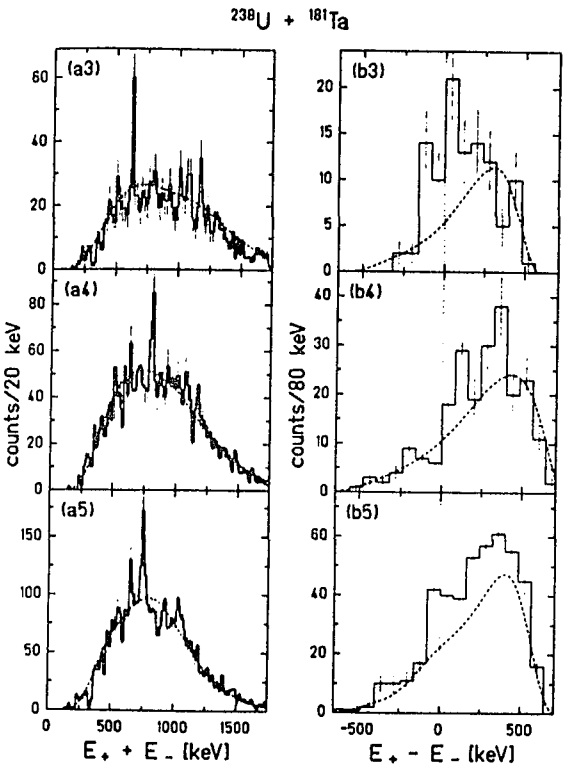

Figure 1.4: EPOS results obtained in U+Ta systems after kinematic cuts. For details, see reference [Sal90]. Three sum-energy lines were observed at $\sim$ 610 keV, $\sim$ 750 keV and $\sim$ 810 keV. They are shown in panels 3, 5 and 4, respectively. The sum-energy lines are much narrower than the difference-energy lines, suggesting a back-to-back two body decay process.

lines at 612 $\pm$ 4 KeV and 817 $\pm$ 5 keV were revealed in the U+Th collision. In the most recent EPOS data [Sal90], again, three consistent sum-energy peaks were observed at 616 $\pm$ 6 keV, 750 $\pm$ 8 keV, and 807 $\pm$ 6 keV. These results are shown in figure 1.4. The sum-energy ($E_{e+} + E_{e-}$) lines were much narrower than the difference-energy ($E_{e+} - E_{e-}$) lines. The narrowness of the sum-energy lines seemed to suggest Doppler cancellation of a back-to-back emission of the positron-electron pair, which was especially clear for the 810 keV line. Many features of the EPOS data were later confirmed by the ORANGE collaboration.

Since then, many explanations have been proposed for the narrow sum-energy

lines, but they have all failed to interpret the detailed features of the heavy-ion data. Barring a situation where some combined complex nuclear and atomic phenomena can be devised to explain these observations, no known processes can account for these narrow peak structures. For lack for conventional explanations, a particle scenario was suggested to explain the implications of the heavy-ion experiments. Thus it was pointed out that a previously unobserved neutral object could be responsible for these positron-electron lines. This object could be formed during the collision, move slowly in the heavy-ion center-of-mass system, and later decay back-to-back into positron and electron pairs. However, it should be noted in this connection that data on energy sharing between the e^+ and e^- and information on their opening angle, as well as other aspects of the data, indicate that the situation is more complex than the possible decay of a *free* particle. Even within the context of a two-body decay scenario, the perturbing influences of the heavy ions or secondary collisions with target atoms on the e^+e^- opening angle, energy sharing and even the lifetime may have to be incorporated into any detailed picture.

Now, the question is, if the object were to exist, would it be possible to produce such an object through the time-reversed process, i.e., the e^+e^- collision. Then, a resonance should be seen in the s-channel e^+e^- (Bhabha) scattering in a much "cleaner" environment than the heavy-ion experiments. It is worth emphasizing that in such an experiment, the resonance energy could be different from the sum-energy observed in heavy-ion experiments, in which a strong time-varying Coulomb field was present. The constraints on the lifetime of the object obtained from present theory and experiments will be discussed in the following sections.

1.3 Constraints on the Lifetime of the Unobserved Light Neutral Object

From the existing experimental data, it is possible to put constraints on this hypothetical object. First, due to the finite GSI detector volume and the heavy-ion e^+e^- sum-energy linewidth, limits on the lifetime of the object can be deduced. Second, introducing such a new particle with a mass in the MeV range would modify the g factor of the electron. Therefore, the strength of the coupling of such X^0 particles to electrons and positrons must be very weak; otherwise they would have already shown up in the virtual process underlying the precision tests of QED. This will put stringent bounds on the lower lifetime limits.

1.3.1 GSI Fiducial Volume

The narrow width of the electron-positron sum-energy lines provides the lower limit on lifetimes for the source of the e^+e^- pair, simply by the Heisenberg uncertainty principle. In this way, lifetimes shorter than 10^{-19} sec are excluded. Furthermore, the EPOS spectrometer is only sensitive to particles that decay close to the target position. The detector efficiency drops quickly for particles travelling distances larger than 1 cm for positrons and 2 cm for electrons. In this connection, the EPOS spectrometer would not be able to detect an e^+e^- source with a lifetime greater than 1 ns, thus restricting the lifetime of the decaying source to less than 10^{-9} sec. So the heavy-ion experiment confines the lifetime of the object to be in the range $10^{-19} \lesssim \tau \lesssim 10^{-9}$ sec.

1.3.2 Precision Measurement of Anomalous Magnetic Moment of the Electron

One of the great successes of Quantum Electrodynamics (QED) is that it predicts the anomalous magnetic moment of the electron with surprising precision. The theoretical value is in agreement with experiments to an accuracy of 10^{-10}. In Dirac's theory, the magnetic moment is proportional to its spin, and it can be expressed as $\vec{\mu_e} = -g\mu_B\vec{s}$, where $\mu_B = e\hbar/2mc$ (the Bohr Magneton), s is the spin of the electron, and g is a constant called the Landé g-factor. For the electron, the $g-$factor should be exactly equal to 2 without the radiative correction. The experimentally measured g-factor for the electron is about 2% higher than this theoretical value, which can be attributed to the fact that real electrons are not bare and are always surrounded by virtual photons in the electromagnetic field. This coupling leads to an increased charge-to-mass ratio. Normally, the deviation from 2 for the g-factor is expressed in terms of the anomalous magnetic moment of the electron with

$$a = \frac{g-2}{2}. \tag{1.1}$$

Considering the correction to the ordinary coupling γ_μ at the $e^+e^-\gamma$ vertex, the QED calculation [Kin81, Kin87] (up to the order of α^4) has given

$$a_{QED} = 1159652302 \times 10^{-12}. \tag{1.2}$$

The latest experimental value for the anomaly [Dyc84] is

$$a_{exp} = 1159652194 \times 10^{-12}. \tag{1.3}$$

There is a very small discrepancy between the QED value and the experimental data

$$\Delta a = a_{QED} - a_{exp} \simeq 2 \times 10^{-10}. \tag{1.4}$$

Introducing a hypothetical particle with an invariant mass of around 2 MeV will contribute to the radiative correction underlying the precision test of QED. If the present level of disagreement, Δa, between theory and experiment, comes from the contribution of the virtual X^0 exchange, then the weak coupling of X^0 to electrons and positrons can be used to derive a lifetime limit.

Reinhardt [Rei87] et al. attempted to set the lifetime bounds for the new particle from the $g-2$ discrepancy. In their work, the most stringent limits on the lifetime of a neutral particle X^0 coupling to e^+e^- were obtained. The lower limits on lifetime were of the order of 10^{-13} sec, depending on the specific coupling. Assuming that Δa is contributed by X^0 - electron coupling , the additional magnetic moment is

$$\Delta a = \frac{\alpha_i}{2\pi} K_i(\rho), \tag{1.5}$$

where the index i = S, P, V, A, denotes scalar, pseudoscalar, vector, and axial vector, respectively. α_i is the coupling of the X^0 to the electron. With the definition of $\rho = m_{X^0}/m$, the functions K_i are given as

$$K_i(\rho) = \int_0^1 \frac{f_i(z)}{z^2 + \rho(1-z)} dz, \tag{1.6}$$

with

$$\begin{aligned} f_S &= z^2(2-z) \\ f_P &= -z^3 \\ f_V &= 2z^2(1-z) \\ f_A &= -\left(z(1-z)(4-z) + 2(\tfrac{1}{\rho})^2 z^3\right). \end{aligned} \tag{1.7}$$

Therefore, the limits on the coupling strength α_i can be obtained. The decay width of the resonance is then [Rei87, Sch88a]

$$\Gamma_i = \alpha_i m G_i(\rho), \tag{1.8}$$

Coupling	α_i	$\Gamma^i_{e^+e^-}$	$\tau^i_{e^+e^-}$
S	$< 7 \times 10^{-9}$	$< 3.0 \times 10^{-3}$ eV	$> 2 \times 10^{-13}$ s
P	$< 1 \times 10^{-8}$	$< 6.8 \times 10^{-3}$ eV	$> 1 \times 10^{-13}$ s
V	$< 3 \times 10^{-8}$	$< 1.6 \times 10^{-2}$ eV	$> 4 \times 10^{-14}$ s
A	$< 5 \times 10^{-9}$	$< 1.4 \times 10^{-3}$ eV	$> 5 \times 10^{-13}$ s

Table 1.1: Bounds set for the light neutral particles X^0 from $g-2$ precision test.

where

$$\begin{aligned} G_S(\rho) &= \tfrac{1}{2}\tfrac{(\rho^2-4)^{\frac{3}{2}}}{\rho^2} \\ G_P(\rho) &= \tfrac{1}{2}(\rho^2-4)^{\frac{1}{2}} \\ G_V(\rho) &= \tfrac{1}{3}\tfrac{(\rho^2-4)^{\frac{1}{2}}}{\rho^2}(\rho^2-2) \\ G_A(\rho) &= \tfrac{1}{3}\tfrac{(\rho^2-4)^{\frac{3}{2}}}{\rho^2}. \end{aligned} \tag{1.9}$$

The bounds on the particle for each coupling are listed in table 1.1.

It is important to note that the calculations presented above are only valid for a pointlike particle. For an extended object, the coupling vertices contain a form factor. Unfortunately, without a detailed knowledge of the particle, it is impossible to set a precise bound for an extended particle. So far, the $g-2$ has provided a very stringent bound on any new particle coupling to the electron, but one problem remains: The GSI heavy-ion data have more than one sum-energy line. This fact seems to suggest that the X^0 has a few states. As we can see, the coefficients K_i have different values in the four couplings; therefore they may cancel each other and give a small value of Δa_i. Hence, the $g-2$ constraint can be removed if both a scalar and a pseudoscalar particle exist with similar masses and lifetimes.

1.3.3 Level Shifts in Positronium Hyperfine Structure

The energy-level structure of positronium is similar to that of the hydrogen atom. The distinction is that positronium is a bound state of a positron and an electron instead of

a proton and an electron. The energy-levels of the positronium bound-state also provide an important test of QED, because the interaction can be completely described by a pure electromagnetic force between the two particles. Therefore, QED should provide precise information about the level spacings. However, there are still discrepancies between theory and experiment. The energy level shift between the singlet 1^1S_0 and the triplet 1^3S_1 (called the hyperfine structure, or HFS) has been measured experimentally to an accuracy of 3.6 ppm, $\Delta\nu = 203.38910(74)$ GHz, whereas a recent theoretical calculation [Kin84, Bod85] gave $\Delta\nu = 203.40251$ GHz, a discrepancy of approximately 10 MHz. Excluding any possible inaccuracy in the calculations and assigning this discrepancy to the existence of a new particle, the bounds on the X^0 coupling could also be estimated.

Schäfer et al. calculated the contribution of the X^0 coupling with a vertex of the type $i = S, P, V, A$ to positronium FHS [Sch86, Sch89], obtaining an additional level shift

$$\Delta E = 4\pi\alpha_i\left(\frac{A_i}{m_{X^0}^2 - 4m^2} - \frac{B_i}{m_{X^0}^2}\right). \tag{1.10}$$

In the non-relativistic limit, parameters A_i and B_i are obtained depending on the spin of the X^0,

$$\begin{aligned} A_S &= 0 & B_S &= |\phi(0)|^2 \\ A_P &= \tfrac{1}{2}(1 - \langle\sigma_1\sigma_2\rangle)|\phi(0)|^2 & B_P &= 0 \\ A_V &= -\tfrac{1}{2}(3 + \langle\sigma_1\sigma_2\rangle)|\phi(0)|^2 & B_V &= |\phi(0)|^2 \\ A_A &= \tfrac{1}{2}(1 - \langle\sigma_1\sigma_2\rangle)|\phi(0)|^2 & B_A &= \langle\sigma_1\sigma_2\rangle|\phi(0)|^2. \end{aligned} \tag{1.11}$$

The spin factors have values $\langle\sigma_1\sigma_2\rangle = -3$ for the singlet state, and $\langle\sigma_1\sigma_2\rangle = 1$ for the triplet states. $\phi(0)$ denotes the non-relativistic positronium ground state wavefunction at the origin. With the resonance mass $M_{X^0} = 1.7$ MeV and by assigning

the discrepancy of 10 MHz to the existence of the X^0, the constraints are

$$\begin{aligned} \alpha_P &< 10^{-6} \qquad \tau_P > 10^{-15} s \\ \alpha_V &< 10^{-6} \qquad \tau_V > 1.2 \times 10^{-15} s \\ \alpha_A &< 7 \times 10^{-7} \quad \tau_A > 3.0 \times 10^{-15} s. \end{aligned} \tag{1.12}$$

There is no limit on the scalar, simply because the energy shift due to the contribution from a scalar is identical for the singlet and triplet states. As it is shown, the bounds set for P, V, and A are not as stringent as the one for $g-2$, but there is no change of sign for different parity and spin. Therefore, in this case, no cancellation between contributions of different X^0 couplings can occur.

1.4 Theoretical Models

Since the observations of the GSI sum-energy lines, made by EPOS and ORANGE collaborations, many studies have speculated on the sources responsible for the anomalous electron-positron peaks. Here, a few models based on the particle scenario, related to the search for the e^+e^- resonance, are discussed.

1.4.1 Is It the Axion?

The mysterious axion became the first candidate for the explanation of the GSI observations. The standard axion is a light pseudoscalar Goldstone boson which was put forth to explain the T and P invariance of the strong interaction [Wil78]. This light boson was first suggested by Peccei and Quinn [Pec77]. It is particularly attractive that the experimentally observed C, P, T conservation by strong interactions arises naturally from quantum chromodynamics (QCD). But there is one problem;

by considering the consequences of the weak and electromagnetic as well as strong interactions, the existence of instanton solutions for non-Abelian gauge fields allows for additional terms in the Lagrangian. These terms can produce strong P,T and CP symmetry violations, which is obviously in contradiction with experiments. There have been a few suggestions to eliminate these terms. The P and T invariance can be restored by having at least one of the quark masses equal to zero, at the cost of disagreeing with current-algebra quark-mass estimates, or by requiring that the Lagrangian has an overall global $U(1)$ symmetry, but this requirement will bring in a new boson which was later named the axion [Pec77]. According to the Peccei-Quinn model, the mass of the axion is expressed as,

$$m_a = 75(x + \frac{1}{x})\ keV, \tag{1.13}$$

where x is the ratio of two vacuum expectation values of the Higgs fields. Thus, the mass is expected to be in the range of 200 keV to a few MeV, which coincides with the mass range of the hypothetical particle suggested by the GSI experiments. The small mass for the axion is reasonable because it arises from symmetry breaking.

After the GSI observations, beam-dump experiments (discussed in the later section of this chapter) were performed to search for this axion, and the results turned out to be negative in the lifetime - mass region suggested by the heavy-ion data.

1.4.2 Is It a Composite Object?

All the experiments performed thus far seem to exclude the possibility of the X^0 being an elementary point-like particle. Besides a number of points of evidence against an elementary particle with invariant mass in the region of interest (1 MeV to 2 MeV), the multi-line structure of the GSI data (the most recent EPOS data [Sal90] showed

three lines at 616 $\pm$ 5, 750 $\pm$ 5, and 807 $\pm$ 6 keV) implies that the narrow e^+e^- lines could be from the decay of a composite object which has a few excited states. In this case, a few sum-energy lines would be expected. However, if this assumption does not stand, it is possible, but very difficult, to accept the fact that a new family of elementary bosons describes the multiple structures of the GSI data.

Müller [Mül86] suggested a composite model, consisting of a few e^+e^- pairs assembled into a $(e^+e^-)^n$ cluster, where n is an integer. This poly-positronium structured system has excited states. Although these states have the properties required to explain the multi sum-energy lines of GSI data, lack of information about the force responsible for binding the e^+e^- pairs is obviously a severe problem. Later, Ionescu [Ion88] was able to prove that the binding force required for such a system would be too large, and if it existed, it would have already been seen in atomic precision-test experiments.

1.4.3 Two-Body Final States vs Multi-Body Final States

The occurrences of the narrower sum-energy e^+e^- peaks, the wider difference-energy peaks, and especially, the nearly equal energy for the positron and the electron arise quite naturally from a two-body decay process. If some other participants were involved in the final state, the kinematics would have appeared totally different. The extra body will take momentum and energy. In this case, the GSI sum-energy lines would be very broad, ranging from 0 to some maximum value; also the electron and the positron would have different energies. This situation is obviously in contradiction with the observed data. Although due to the complexity of the heavy-ion experiments, the multi-body final states are not necessarily excluded, our search for

this new object mainly focuses on the two-body decay scenario. Further, the detectors employed in our experiment were designed only to accommodate two-body decay kinematics. Multi-body decay channels were also investigated and are discussed at the end of the thesis, however, it is worth emphasizing that this was not our initial goal.

1.5 Previous Experimental Searches for a Neutral Object

Since the GSI observation, a number of experiments have been performed to search for this new object, with results ranging from positive to negative. To date, there are no convincing experimental results showing the existence of the X^0. Some of the experiments have set bounds on the particle in a small portion of the mass region suggested by the GSI data. Most of them had sensitivities below the limits given by the $g-2$ precision test. In this chapter, A few of these experiments will be discussed. There is a large mass-lifetime region in which the existence of the X^0 remains uninvestigated mainly due to the lack of a well-characterized, tunable monoenergetic positron beam at an energy of a few MeV.

1.5.1 Creation of X^0 Through Bremsstrahlung

In relating the GSI X^0 to the axion, the first set of experiments performed to search for the neutral object (X^0 or axion) suggested by the heavy-ion collision data used electron, muon, and proton beam-dumps. Because the GSI data suggested that the X^0 decays into an electron and a positron, predominant coupling of X^0 to electrons and positrons is assumed. The coupling constant can be uniquely determined as

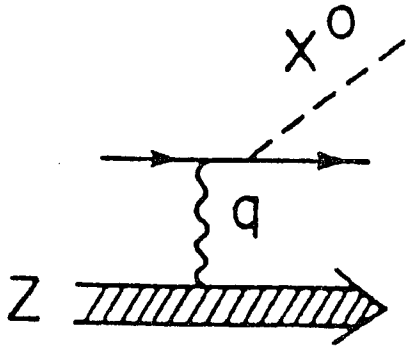

Figure 1.5: X^0 bremsstrahlung production mechanism.

[Tsa86]

$$\alpha_X = \frac{2}{\tau}(m_{X^0}^2 - 4m_e^2)^{-\frac{1}{2}}, \tag{1.14}$$

where m_{X^0} is the assumed mass for X^0 and τ is the intrinsic lifetime. The X^0 production mechanism is depicted in figure 1.5. X^0's are created via bremsstrahlung or the Primakoff effect when the incident high-energy electrons (or other particles) are slowed down and stopped in the target. In principle, the X^0's can be created by protons, pions or muons as well as electrons and positrons. However, even in the proton dump, most of the X^0's are likely created by the bremsstrahlung from electrons and positrons in the dump. The first generation of particles will create electrons, and the X^0's are produced via the process $e + Z \rightarrow e + Z + X^0$.

Y.S. Tsai [Tsa86] made the first theoretical calculation of the expected axion production rate as well as the energy-angle distribution and the energy distribution from electron scattering on an atomic target using the generalized Weizsacher-Williams method. The angular distribution of the X^0 is sharply forward-peaked, which is quite different from that of the photon. Based on the calculation, a number of electron beam-dump experiments were able to rule out the existence of a non-interacting

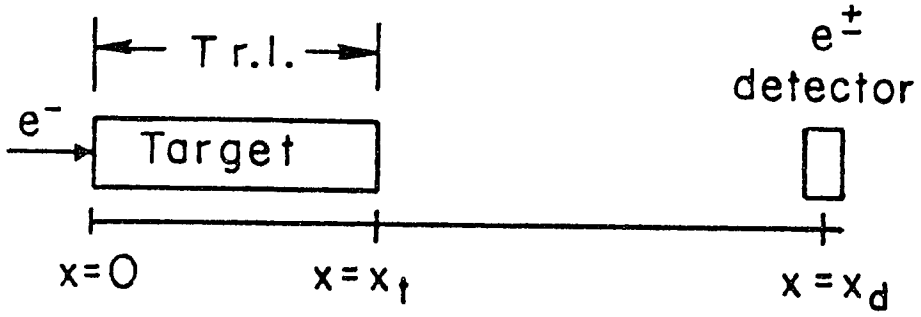

Figure 1.6: The set up of a typical electron beam-dump experiment.

pseudoscalar boson in a wide lifetime-mass range, including the entire region suggested by the GSI heavy-ion experiments. Figure 1.6 shows a typical configuration of an electron beam-dump experiment. The target thickness has to be carefully chosen. When the electrons enter the target, they will lose their energy very rapidly within a few radiation lengths of the target. Therefore, the majority of axions will be created in this region. The target should be thick enough so that the electromagnetic shower is absorbed, but thin enough to let the possible short-live axions escape from the target.

The first experiments to search for the axion were performed in the early 1980s [Bec79, Jac80], independent of the GSI observations. Bechis et al. were able to rule out two bands for the parameter x (x is the ratio of two Higgs fields, $x = \frac{\langle\phi_1\rangle}{\langle\phi_2\rangle}$) at 90% confidence level (CL), $0.074 \leq x \leq 0.042$ and $9.2 \leq x \leq 70$, for an axion decaying into e^+e^- or $\gamma\gamma$, using a 11.8 g/cm^2 tantalum target and a 45.3-MeV electron beam-dump. At mass $M_{X^0} = 1.8$ MeV, axions with lifetimes greater than 10^{-11} sec are excluded. Jacques et al. performed a proton-beam-dump experiment, in which they set the upper limit for the ratio of the axion production rate to the π^0 production rate, $R = \frac{\sigma(pN\to a^0+...)}{\sigma(pN\to\pi^0+...)} < 10^{-8}$ at 90% CL.

The observation of narrow sum-energy peaks in the positron and electron spectra in heavy-ion experiments attracted much attention to the axion. Since then, several more sensitive experiments [Kon86, Bro86, Dav86, Rio87] have been carried out to search for evidence of the existence of the axion, through electron or proton beam-dumps. Using a 2.5-GeV electron accelerator and a combination of iron of thickness of $\sim$ 2.5m, lead and plastic dump, Konaka et al. obtained impressive results. In their experiment, the decay products e^+e^- were measured by a set of detectors including multiwire proportional chambers and a scintillation hodoscope in front of a lead-glass counter for vertex reconstruction. After the required kinematic cuts for the axions, no candidate events remained. The sensitivity was mainly restricted by the dump length when the absorption of the X^0 in the dump was large. Lifetimes for the axion from $2 \times 10^{-13} < \tau < 10^{-10}$ sec were excluded at 90% confidence level (CL). Figure 1.7 shows the limits on the coupling constant from their experiment.

In the experiment by Brown et al. [Bro86], the axion was expected to be created via proton-beam-dump from a 800-GeV proton beam. A 5.5-m-long copper target was used as the beam-dump. The hadronic and electromagnetic showers were responsible for producing the new particle, and the subsequent decay of e^+e^- events was detected by a high efficiency spectrometer. This experiment established a sensitivity in lifetime up to $\tau >\sim 10^{-14}$ sec over a wide mass range. But both of these experiments made the common assumption that the absorption cross-section of the axion in the dump is small. Due to the thick beam-dump material, the axion suffers significant attenuation even if the absorption cross-section is only 0.5 mb per nucleon. Riordan et al. [Rio87] solved this problem by employing very thin beam dumps. Electrons with energies of about 9.0 to 22.4 GeV struck the 10 cm or 12 cm copper and tungsten dumps. This experiment set much better limits for the axion without causing a large attenuation

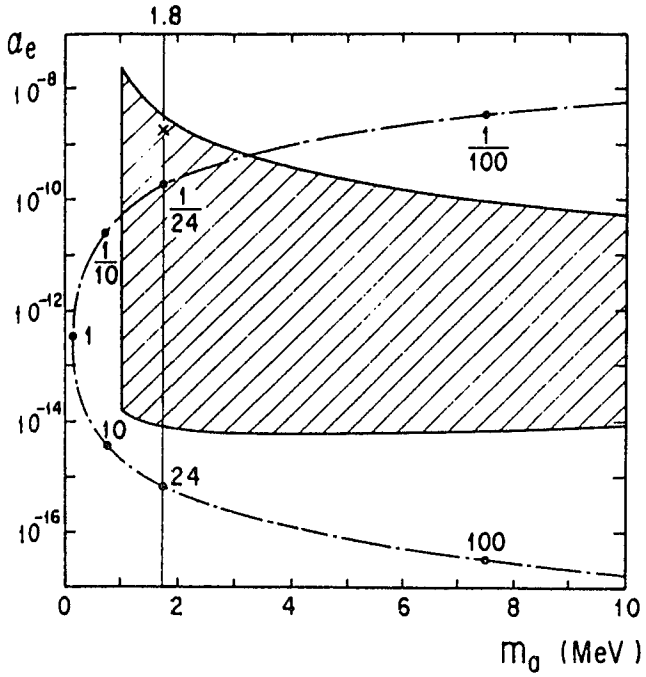

Figure 1.7: Constraints on α_e as a function of the axion mass. The hatched region is excluded by the experiment (90% CL) if axion bremsstrahlung is assumed. The dash-dotted line indicates the prediction of the standard axion model. The figure is reproduced from [Kon86].

of the particle even when the absorption cross-section per nucleon was assumed to be 50 mb.

So far, all beam-dump experiments searching for the standard axion in the lifetime and mass region suggested by GSI heavy-ion data have shown no evidence for its existence. In relating the axion to the GSI X^0 or other possible light pseudoscalars, there are still questions concerning the limits set by these experiments. One argument against the validity of the beam-dump experiments centers on how large the absorption really is. The other centers on what the production rate for X^0 is if there is a formfactor modifying the particle. The limits set on the X^0 strongly depend on the answers to these questions. Although the experiment of Riordan et al. can set the limits even at a fairly large absorption cross section for the X^0, the final bounds still depend on the exact absorption cross-section. Since so far there is no detailed

knowledge about the X^0 itself, it is impossible to know the exact cross-section for absorption. On the issue of an extended state, Schäfer [Sch88a] discussed the effect of a finite size of X^0 on the bremsstrahlung production rate.

1.5.2 Creation of X^0 Through Nuclear De-excitation

The search for the new particle in the beam-dump experiments ruled out the standard axion model. In an attempt to explain these negative beam-dump results, two groups, Peccei et al. [Pec86] and Krauss et al. [Kra86], in 1986 independently suggested a modified axion model, in which the coupling of the axion to the charm and bottom quarks is weakened, while maintaining its coupling to the light up and down quarks and leptons. This new theory indicates that the beam-dump experiments are not sensitive to the modified axion model, but allows this new axion to be produced in nuclear processes. In late 1986, experiments [Hal86, Sav86, Boe86, Bab86, Sav88] were carried out to search for the hypothetical particle, by investigating the possible coupling of the light neutral particle to nucleons. The e^+e^- events produced from the X^0 in the nuclear decay experiments can be separated from the e^+e^- events of the ordinary internal pair conversion in electromagnetic decay of the nuclear states by the different angular correlations corresponding to these two processes. If the observed positron-electron peaks in the GSI heavy-ion experiments can be attributed to this new particle, it would cause a strong signal of positron-electron pairs in competition with γ-rays or with the existing e^+e^- from virtual photon internal conversion.

In a set of such experiments, no obvious evidence of the X^0 was observed. The constraints of the coupling of the particle to the nucleons were improved step-wise. Savage et al. [Sav88] searched for the axion with a sensitivity of $10^{-19} < \tau < 10^{-11}$ s in the mass range of $1.022 < M_{X^0} < 5$ MeV. By measuring the angular correlation

Axion Model	$\Gamma_a/\Gamma_{\pi M1}$(Isovector)	$\Gamma_a/\Gamma_{\pi M1}$(Isoscalar)
Standard ($x = 0.044$)	5.3	310
Krauss and Wilczek ($x = 68$)	7.2	0
Peccei et al.		
I ($x = 68$)	7.2	0
II ($x = 68$)	1.1	680
III ($x = 34$)	0.66	170
Experiments	0.104	2.2

Table 1.2: The results from several theories and experiments on the branching ratio of the axion [Hal86].

of e^+e^- pairs emitted from excited states of ^{14}N, ^{16}O and ^{8}Be, upper limits were set on the branching ratio to electromagnetic decay, $\Gamma_a/\Gamma_\pi < 0.18$ (in ^{14}N) for isovector particles, and $\Gamma_a/\Gamma_\pi < 0.50$ (in ^{8}Be) for isoscalar particles, at the 90% confidence level. For a 1.8 MeV particle, the limits on the isoscalar and isovector coupling constants to nucleons are,

$$g^0 < 1.6 \times 10^{-2}$$

$$g^1 < 2.0 \times 10^{-2}.$$

As mentioned in the preceding section, the validity of strong limits from beam-dump experiments depends on the small X^0-nucleon cross section. These nuclear decay experiments provide an estimate of the absorption. Savage et al. gave an approximate value of the cross section as $\sigma_{XN} \sim 1\mu b$. This value is significantly below the limit at which the sensitivity of the beam-dump experiments starts to drop.

Hallin et al. [Hal86] also reported that the axion intensity was a factor of 50 weaker than theoretical predictions. Some of their results are listed in Table 1.2.

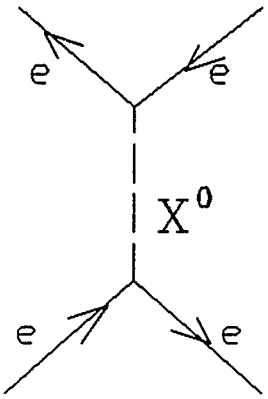

Figure 1.8: Feynman diagram of the resonant e^+e^- scattering.

1.5.3 Creation of X^0 From Low-energy Elastic Electron-Positron Scattering

Although the beam-dump and nuclear decay experiments seemed to exclude the existence of a point-like elementary particle, they all suffered a serious problem. The interpretation of the experimental data relied on the specific coupling model, and, in the case of beam-dump experiments, the absorption cross-section of the product X^0 in the target. A model-independent search for the light neutral particle must hinge upon a precision test of the elastic e^+e^- scattering cross-section, such as the experiment reported in this thesis.

The GSI heavy-ion data showed a clear exit channel of the low-mass neutral particle to the positron-electron pair, $X^0 \rightarrow e^+e^-$. Assuming that the creation of the X^0 does not need the strongly varying electromagnetic field which exists in the heavy-ion collisions, the process $(e^+e^- \rightarrow X^0)$, i.e., resonances in elastic positron-electron scattering at low energy, would provide the most conclusive and model-independent method to test the particle hypothesis. This reverse process is allowed by the *principle of detailed balance.* The Feynman diagram for the production and decay of the X^0 through the s-channel is shown in figure 1.8.

In such an experiment, the entrance channel is exactly the same as the exit channel observed in the GSI experiments. Although the cross-section of positron-electron (Bhabha) scattering can be calculated with great precision by QED, due to the lack of interest in this energy region (a few MeV) and the technical difficulties of obtaining a mono-energetic positron beam at such a low energy range, experiments on e^+e^- scattering performed prior to the GSI observations are limited and none of them put any valuable limits on the coupling of the new particle to e^+e^-. An experiment performed by Ashkin et al. [Ash54] in 1954 investigated the e^+e^- scattering cross section with 10% accuracy for 3 discrete positron energies at 0.61 MeV, 0.82 MeV, and 1.15 MeV.

Stimulated by the heavy-ion observation, there have been an abundance of experiments on the precision test of the e^+e^- scattering cross section, searching for evidence for the existence of the light neutral particle. On first consideration, the cleanest experiment would seem to be the collision of e^+e^- using a positron-electron collider. However, the technical problems aside, the luminosity at such low energies is too low to allow for the required statistics. A practical solution is to bombard a stationary electron target with positrons. The first work of this kind reported [Erb86, Pec87a, Wan87, Sak88, Bar87, Bar89] was not sensitive enough to reach the lifetime limits beyond the one set by the $g-2$ precision test, and the results are confusing, ranging from positive to negative. All of these experiments utilized a Th target with which the anomalous e^+e^- sum-energy lines were produced in heavy-ion collisions. As will be discussed in detail in chapter 2, the choice of this high Z target is poor for the resonance signal sensitivity, for two reasons: (1) the ratio of the core electrons to valance electrons is large, and (2) the momentum spread of the valance electrons is large. These factors cause the resonance peak to smear into a much

broader spectrum. Also, the positrons from the decay of a radioactive source (for example ^{68}Ga) are widely spread in energy. These experiments are briefly reviewed below:

Review of the e^+e^- Scattering Experiments

The first experiment to look for resonance in e^+e^- elastic scattering was carried out in 1986 by Erb et al. [Erb86] after the announcement of the GSI results. A thick Th target was bombarded with e^+ from a $\sim 40\mu$Ci ^{68}Ga source. A positive result was reported: at an invariant mass around 1.32 MeV, the existence of a peak structure was observed. Due to the Compton edge introduced by 511 keV annihilation photons, their result was based on a small excess of events above a large background, with insufficient statistics. Furthermore, the 1.32 MeV peak did not correspond to the GSI peaks kinematically. Later, in 1987, two groups [Pec87b, Wan87] repeated the same experiment on e^+ + Th scattering with improved detector performance and a much suppressed background. After the subtraction of the Compton edge from the raw spectrum, no peak was observed.

Nevertheless, as more experiments were performed, two other groups [Sak88, Bar87, Bar89] reported that a spectral structure in e^+e^- scattering was observed. Again, these conclusions were based on insufficient statistics. As several authors later pointed out (for example, in reference [Sch91]), in all of these experiments with high-Z targets, the large electron momentum spread in the target will give a broadened resonance peak of width at least 60 keV, and, in the electron energy spectrum alone, a width of a few hundred keV would be expected. There is no physical mechanism by which a resonance width as narrow as a few keV can be obtained, as reported in reference [Sak88].

In the experiment of Wimmersperg et al. [Wim87], a low Z target was used as the electron source for scattering, for the first time, abandoning the idea that the e^+e^- resonance would rely on a Th target. In their setup, positrons from a ^{27}Si source were scattered off electrons in a polyethylene target, and the coincidences of e^+e^- events were measured with two scintillators arranged at an angle of $\pi/2$ symmetrically with respect to the target. The data showed $5.8 \pm 2.7\%$ deviation from the Bhabha background at the sum-energy of 710 keV in the center of mass system. This deviation amounted to 14.5 ± 6.8 keV b for the energy-integrated cross section, and this was attributed to the e^+e^- resonance. If this were the real resonance signal, it would have shown up distinctly in the electron $g-2$ precision test, more than two orders of magnitude above the $g-2$ limit. Their conclusion, based on a twelve-point spectrum in the e^+e^- scattering, was not rigid; the excess counts basically came from some unknown systematic errors. The experimental results were not improved much by Mills et al. [Mil87]. No one had been able to reach the $g-2$ limit up to this point. The conclusions from such elastic e^+e^- scattering experiments were just bouncing back and forth between the negative and the positive. Obviously, improvements in the stability and intensity of the positron source had to be made.

The next set of experiments progressed in such a direction. A few mono-energetic positron beams at the MeV range were constructed, including the Dynamitron positron beam built at Brookhaven National Laboratory. Positrons with narrow energy width, better stability, and a large flux provided greater statistics and cleaner background in the data. With a positron beam, the energy was also much more controllable. At this point, the search for the X^0 through elastic e^+e^- scattering began to reach lifetime regions beyond the $g-2$ limit.

Starting with the Stuttgart pelletron accelerator, Maier at al [Mai87] obtained

Group	Energy	E_{peak}	Target
Erb[Erb86]	1100-2200 keV	1360 keV	Th
Bargholtz[Bar87]	1290-1450 keV	1350 keV	Th
Sakai[Sak88]	1200-2900 keV	1350 keV	Th
Bargholtz[Bar89]	1270-1470 keV	1340 keV	Th

Table 1.3: Summary of e^+e^- scattering experiments which obtained a resonance.

mono-energetic positrons from a 33 mCi ^{22}Na source moderated by a 3μm thick W moderator (the moderation process to obtain mono-energetic positrons will be discussed in detail in chapter 2). With a low-Z mylar ($C_2H_4O_2$) target and a detector array consisting of five PM-tubes, they were able to reconstruct the kinematics of the scattering events with angular resolutions of 2.4° and 8° in the θ and ϕ directions, respectively. The background was effectively suppressed. No peak-like structures were observed in the e^+e^- cross-section. A limit was placed on the X^0 lifetime of $\tau > 1.8 \times 10^{-14}$ sec, which was close to the $g-2$ limits. However, one year later, the same group [Mai88a] announced that a resonance was observed in the e^+e^- scattering cross-section at 810.4 ± 1.1 keV, coincident with the GSI 810 keV line with an energy-integrated cross-section $\sigma_{res} \cdot \Gamma_{res}^{e^+e^-} = 30$ barn eV (C.M.). Unfortunately, this encouraging result was later withdrawn by the authors [Mai88b]. It was due to an overnight drift of the detector efficiency. In an attempt to confirm the Stuttgart results, Lorenz et al. [Lor88] investigated the invariant mass region $1.62 < M_{X^0} < 1.89$ MeV. No resonance was observed. They reached the lifetime limit of $\sim 3.5 \times 10^{-14}$ sec. The results of e^+e^- scattering experiments are summarized in Tables 1.3 and 1.4.

About the same time, a group at Grenoble began an experimental search in this area, publishing their first paper [Tse88b, Tse88a] in 1988. The experiment investigated the invariant mass near the GSI 810 keV line with $1782 < M_{X^0} < 1860$ keV. No

Group	Energy (keV)	Target	$(\int \sigma dE)_{max}$
Peckhaus[Pec87a]	1200-2800	Th	
Wang[Wan87]	1200-2800	Th	
Mills[Mil87]	1500-2000	Be	1000 beV
Maier[Mai87]	1620-1670	Mylar	65 beV
Maier[Mai88a]	1800-1870	Be	
Lorenz[Lor88]	1620-1890	Be	62 beV
Tsertos[Tse88a]	1780-1860	Be	12.6 beV
Tsertos[Tse88b]	1790-1860	Be	6.3 beV
Tsertos[Tse89]	1500-1650	Mylar	30 beV
Judge[Jud90]	1770-1860	Be	$\tau > 7.5 \times 10^{-12}$ s
Widmann[Wid91]	1800-1920	Active target	excluded
			$\sim 1.2 \times 10^{-13} < \tau < 3.0 \times 10^{-12}$ s

Table 1.4: Summary of e^+e^- scattering experiments which did not obtain any resonance.

resonance structures were seen. In this experiment, a metallic beryllium target was chosen to enhance the resonance signal in the e^+e^- scattering, since electrons exhibit a narrow momentum distribution in this target. Positrons were obtained from an ILL High-Flux reactor with the BILL β-spectrometer and a total beam flux of $8 \times 10^5 e^+/s$. The detector system consisted of two arrays of four Si(Li) detectors for kinematic reconstruction. Both Bhabha events and Mott events ($e^+Z \rightarrow e^+Z$) were recorded. Because no resonance would be expected in the Mott scattering spectrum due to the X^0 and because this process takes place at the same time as the Bhabha scattering process, it provided a very good basis for normalizing the Bhabha scattering events, independent of variations in beam flux. For each step in energy, $\sim 4 \times 10^{+4}$ coincidence events were collected in the Bhabha spectrum, and $\sim 2 \times 10^{+5}$ singles events for the Mott scattering. For the first time, the statistics reached 0.5% in the Bhabha/Mott spectrum. This experiment excluded a lifetime region with $\tau < 4.3 \times 10^{-14}$ sec for a pseudoscalar particle around mass 1.832 MeV. The same group reported another experiment [Tse89] with improved sensitivity and better statistics (0.25%) and a total

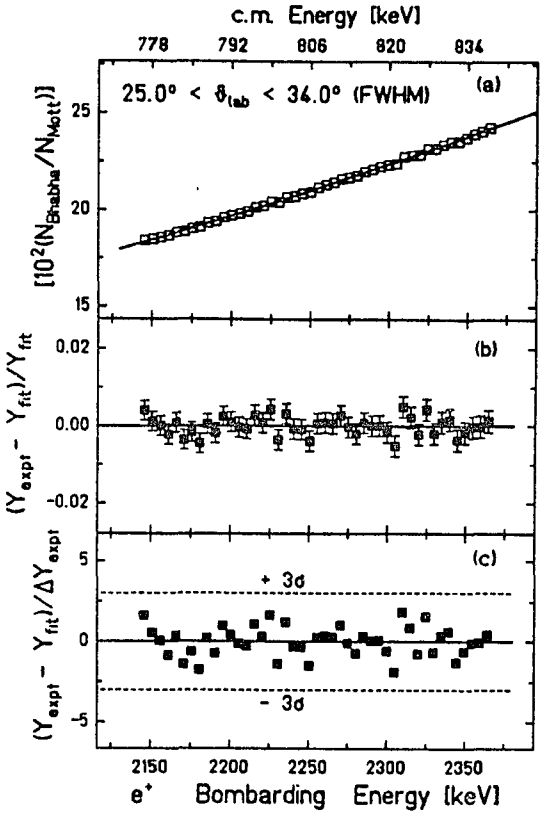

Figure 1.9: Deviation in the elastic e^+e^- scattering cross section, obtained with a thin beryllium target [Tse89].

deviation of 0.35% including systematic errors. The result again was negative. But this time, a stringent limit was set for the light neutral pseudoscalar particle with $\tau > 3.5 \times 10^{-13}$ s, which was beyond the $g-2$ limit, at the same invariant mass range as in their first experiment. Figure 1.9 shows the deviation from the Bhabha background obtained in the experiment. A few different targets were also tested in this experiment, but they gave less stringent bounds for the new particle.

To reach lifetimes beyond 10^{-12} sec, obviously, better statistics are required. However, this is extremely difficult to achieve, because, at this sensitivity, the systematic uncertainty starts to dominate. One way to avoid the need for high statistics is to

eliminate the momentum broadening in the target. Some groups were trying to confine low-temperature positrons in an area and to bombard the free positron target with mono-energetic electrons; no result has been reported thus far. On the other hand, a few experiments, including the one performed by the Yale-BNL group, suppressed the non-resonant Bhabha background to look for the events from the decay of X^0 only, but the absorption of candidate events in the target had to be assumed small.

Despite all of these experiments in elastic e^+e^- scattering, only a fraction of the open mass-lifetime area had been covered (see figure 1.10). Now, with the experiment reported in this thesis covering the whole mass range in the short lifetime area ($\tau < a few \times 10^{-13}$ sec), and the one performed by the same group (S.D. Henderson, Ph.D thesis, Yale University 1991), utilizing an active target to suppress the non-resonant Bhabha background to reach the longer lifetime limits ($10^{-10} < \tau < 10^{-12}$ sec), nearly the entire open region suggested for the existence of the X^0 has been systematically studied. Our results, together with those from a few other important experiments, are discussed in chapter 3.

1.6 The Present Experimental Work

In a collaboration with the Physics Department of Yale University, we searched for X^0 in the mass region from ~1.5 MeV to ~1.9 MeV, through elastic electron-positron (Bhabha) scattering. Resonant enhancement in Bhabha scattering was expected to appear through the s-channel contribution. With an apparatus having much better resolution and sensitivity, and also with the successful construction of a 0.5 to 2.8 MeV tunable mono-energetic positron beam at Brookhaven National Laboratory, the e^+e^- scattering cross section was carefully investigated. The Yale group, headed by J.S.

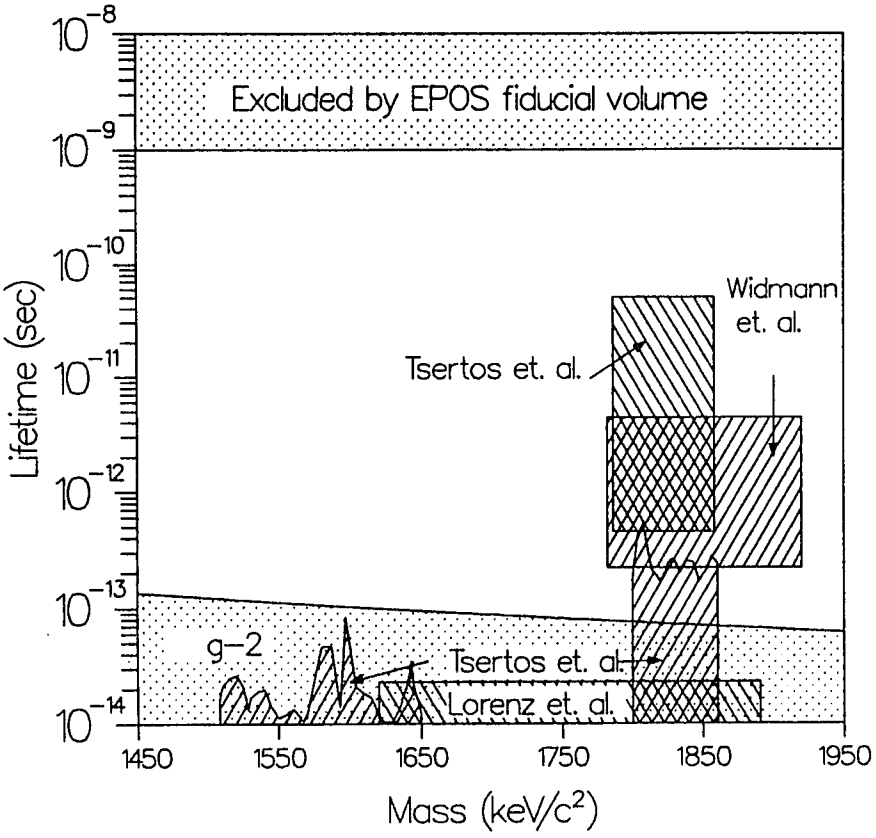

Figure 1.10: The GSI experiments suggested area, together with the results of the e^+e^- experiments which have been performed. There is a large region still uninvestigated.

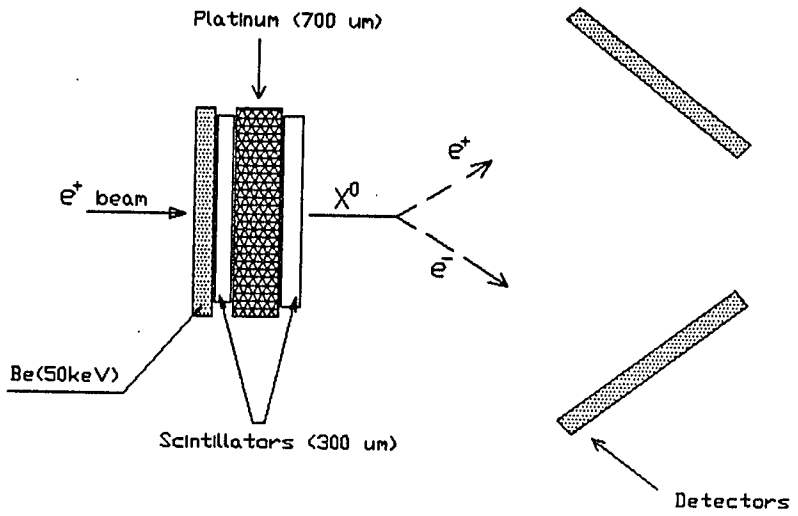

Figure 1.11: The active target utilized in the experiment [Hen88] to select the vertex of a non-interacting neutral decay for longer lifetime sensitivity.

Greenberg, was involved in searching for the light neutral particle in a long lifetime region $\tau > 10^{-12}$ sec, employing an active target (Be-Scintillator-Pt-Scintillator) to veto the non-resonant Bhabha events which are stopped by the thick platinum (see figure 1.11). In this setup, only non-interacting neutral particles can penetrate the platinum and decay outside the target. The detected candidate e^+e^- event rate after kinematic cuts is approximately one event for a period of 24 hours data collection (for a detailed discussion, see reference [Hen88]).

For the short lifetime $\tau <$ a few $\times 10^{-13}$ s, the Brookhaven group, headed by K.G. Lynn, searched for the resonance through direct elastic Bhabha scattering. This will be the main topic of part 1 of this thesis. Compared with the experiments of Tsertos et al.[Tse88b, Tse88a, Tse89], our experiment has much less background, better detector resolution, and most of all, a much wider invariant mass range covering the three GSI sum-energy lines of 616 keV, 750 keV, and 807 keV. In the next two chapters, a detailed description of the experiment, the data collection and data analysis are

discussed. Stringent limits obtained for the lifetime of the X^0 by the BNL-Yale collaboration through a direct elastic e^+e^- scattering experiment are presented.

Chapter 2

Resonant Positron-Electron scattering

Elastic positron-electron scattering has long been a well-understood process. The cross section of the process was first calculated by H.J. Bhabha in 1935, in his article **"The scattering of positrons by electrons with exchange on Dirac's theory of the positron"**. The process was later named after the author. Although the theory was carefully tested in the high-energy range as a test of QED, for nearly half a century no interest was paid to the low-energy range around a few MeV. Recently, however, due to the observation of the anomalous sum-energy peaks of the positron-electron pair in the GSI heavy-ion collision experiments, the Bhabha scattering cross section was intensively studied, with the hope of obtaining resonance-like structures in the MeV range. Since 1986, several groups have investigated this previously untouched area, including the group to which the author belongs.

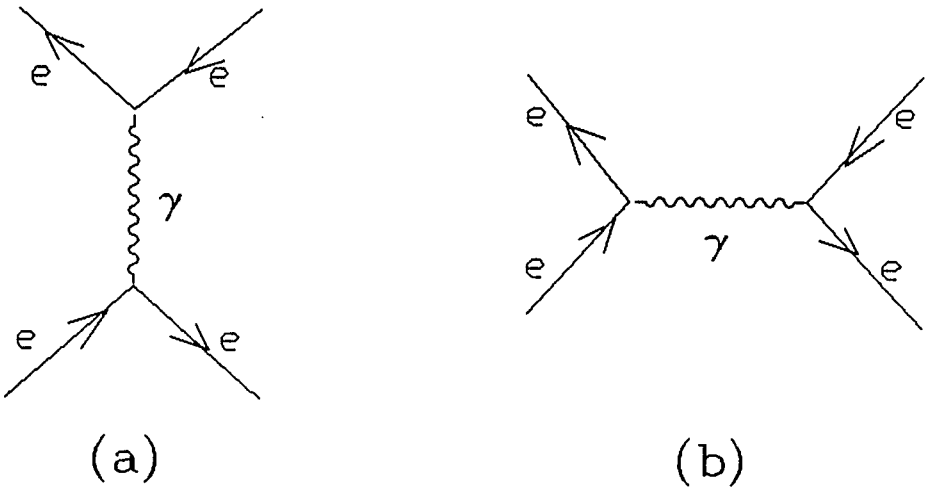

Figure 2.1: Feynman diagram of e^+e^-scattering: (a) s-channel (b) t-channel

2.1 QED e^+e^- Scattering

Figure 2.1 shows the low-order Feynman diagram for ordinary Bhabha scattering (thereafter, called QED Bhabha scattering as distinct from resonant e^+e^- scattering), due only to the coupling of positrons and electrons to photons. This process can be described completely by QED. Both the s-channel and t-channel contribute to the lowest order diagrams. The cross section contributed by both diagrams in figure 2.1 in the center of mass system is

$$\left(\frac{d\sigma}{d\Omega}\right)_{CM} = \frac{r_e^2 m^2}{16E^2}\left(\frac{(E^2+P^2)^2}{P^4\sin^4\frac{\theta}{2}} - \frac{8E^4-m^4}{P^2E^2\sin^2\frac{\theta}{2}} + \frac{12E^4+m^4}{E^4} - \frac{(4P^4+4E^2P^2)\sin^2\frac{\theta}{2}}{E^4} + \frac{4P^4\sin^4\frac{\theta}{2}}{E^4}\right) \quad (2.1)$$

where E, P, and θ are the energy, momentum, and scattering angle of the particle (e^+ or e^-) in the center of mass system, respectively, and m is the electron rest mass.

In such two-body scattering kinematics, the invariant mass is defined as

$$s = (E_{e+} + E_{e-})^2 - (P_{e+} + P_{e-})^2. \tag{2.2}$$

In the center of mass system, with $E_{e+} = E_{e-} = E$ and $P_{e+} + P_{e-} = 0$, equation 2.2 becomes

$$s = 4 \cdot E^2. \tag{2.3}$$

For a typical detector acceptance angle of $60° \leq \theta \leq 120°$ in the CM system, the total cross section is roughly 200 mb at an energy of $\sim$1 MeV.

2.2 Resonant e^+e^- Scattering Due to The X^0

With the existence of a light neutral particle coupling to e^+ and e^-, the elastic e^+e^- scattering cross section has to be modified to incorporate the new coupling. The following Feynman diagram in figure 2.2 is added to the original diagram in figure 2.1 for the cross section calculation. The two Feynman diagrams, figures 2.1 and 2.2, are similar except the exchanging photon in figure 2.1 is replaced by the X^0 in figure 2.2. One difference worth mentioning is that in figure 2.2, from the s-channel Feynman diagram, the X^0 can be created as a resonance on the mass-shell because of its non-zero rest mass. The contribution from the t-channel is relatively small near the resonance, and it provides a continuous background.

Total Resonance Cross Section

It is well known that in the partial wave analysis of cross sections, for a partial wave with angular momentum J, the peak cross section is bounded by unitarity,

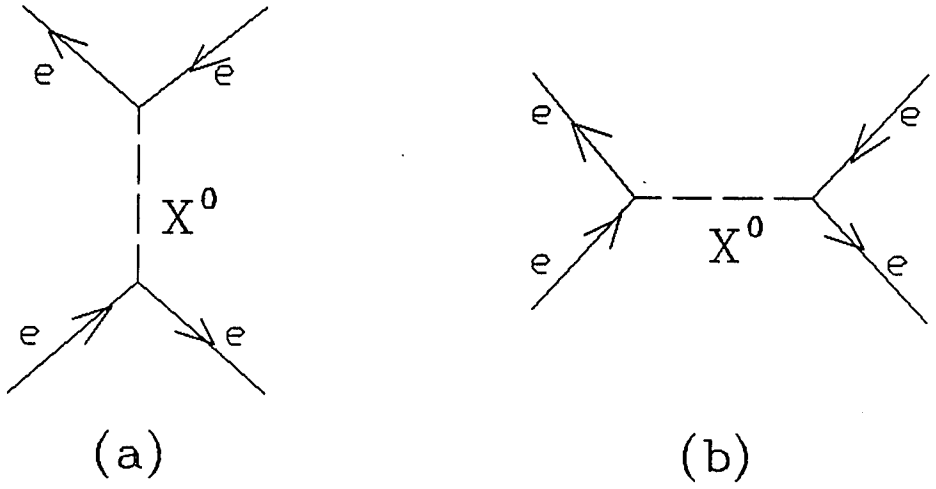

Figure 2.2: Feynman diagram showing contribution from the coupling of the X^0 (a) s-channel (b) t-channel.

independent of the specific model [Bla52]

$$\sigma_{CM}^{Max} = 4\pi\lambda^2 \frac{2J+1}{(2s_1+1)(2s_2+1)} \tag{2.4}$$

where s_1 and s_2 are the spins of the electron and positron, and λ denotes the resonance wavelength

$$\lambda = \frac{2\hbar}{(M_{X^0}{}^2 - 4m^2)^{1/2}}. \tag{2.5}$$

At invariant mass 1.8 MeV, the peak cross section is $\sim$ 2000 barns, overwhelming the QED Bhabha scattering cross section by orders of magnitude. But this cross section cannot be realized in practice, due to the narrow intrinsic resonance width and widely spread invariant mass contributed by the electron momentum distribution in the target. In principle, the amplitudes for resonant and QED Bhabha scattering have to be added together coherently. However, it has been noted that the interference terms are small and can be neglected [Sch91]. The dependence of the total resonance cross section on the invariant mass can be expressed by the standard Breit-Wigner

distribution,

$$\sigma_{CM}(s) = \sigma_{CM}^{Max} \frac{\frac{1}{4}\Gamma_{e^+e^-}^2}{(\sqrt{s} - M_{X^0})^2 + (\Gamma_{e^+e^-}/2)^2}, \tag{2.6}$$

where $\Gamma_{e^+e^-}$ is the intrinsic resonance width of the X^0. From the $g-2$ limit, $\Gamma_{e^+e^-}$ is of the order of 10^{-2} eV. Therefore, the total energy-integrated resonance cross section is

$$\int_{-\infty}^{+\infty} \sigma_{CM}(s) d\sqrt{s} = \frac{\pi}{2} \sigma_{CM}^{Max} \Gamma_{e^+e^-}. \tag{2.7}$$

As mentioned above, the resonance width is broadened in the real experiment. For a low Z electron target, at resonance the invariant mass has a typical width ΔE of ~ 10 keV, while the intrinsic width $\Gamma_{e^+e^-}$ is 10^{-2} eV at the $g-2$ limit ($\tau \sim 10^{-13}$ sec). In the experiment, the observed peak cross section is reduced to $\sim \sigma_{CM}^{Max} \cdot \Gamma_{e^+e^-}/\Delta E = 2$ mb. On the other hand, the QED Bhabha cross section continuum is 200 mb; hence, to reach lifetimes longer than the $g-2$ limit, an experimental sensitivity better than 1% is required.

Differential Resonance Cross Section

In 1987, Reinhardt et al. [Rei87] first calculated the resonant differential cross section. After some general remarks on the coupling of the resonant states, the angular distribution of the resonant Bhabha scattering cross section was evaluated, assuming the electrons are at rest in the target. The Lagrangian of the field describing the X^0 boson can be expressed as

$$L = g_i \int d^3x \bar{\psi} \Gamma_i \psi \phi_{X^0}, \tag{2.8}$$

where $\bar{\psi}\Gamma_i\psi$ represents the covariants of the Dirac field ψ, and ϕ_{X^0} describes the X^0 boson field, satisfying the Klein-Gordon or Proca equation. The vertices for the coupling are listed in table 2.1. The result is only valid for an elementary point-like boson. A *form factor* has to be applied to the calculation for a composite object, and

i	J^π	$\Gamma_i^{(a)}$	$\Gamma_i^{(b)}$	$\Gamma_i^{(c)}$
Scalar (S)	0^+	1		
Pseudoscalar (P)	0^-	$i\gamma_5$		
Vector (V)	1^-	γ_μ	$(p_1+p_2)_\mu$	$(p_1-p_2)_\mu$
Axial-Vector (A)	1^+	$\gamma_\mu\gamma_5$	$i(p_1+p_2)_\mu\gamma_5$	$i(p_1-p_2)_\mu\gamma_5$

Table 2.1: Coupling vertices for an elementary point-like boson. These three vertices are the possible vertices for $J = 1$.

this is model-dependent. The unpolarized differential cross section in the laboratory system is given by,

$$\overline{\left(\frac{d\sigma}{\Omega}\right)}_{lab} = \frac{\alpha_{X0}^2}{m^2}\frac{\cos\theta}{(1-b^2\cos^2\theta)^2}\frac{m^2}{(E+m)^2}\frac{m^2}{(E-E_R)^2+(\rho\Gamma/2)^2}S_i(s,t,u). \qquad (2.9)$$

For couplings S_i,

$$\begin{aligned} S_S(s,t,u) &= \tfrac{1}{4}(s-4m^2)^2/m^4 \\ S_P(s,t,u) &= \tfrac{1}{4}s^2/m^4 \\ S_V(s,t,u) &= \tfrac{4}{m^4}\left(m^2s - m^4 + (u^2+t^2)/8\right) \\ S_A(s,t,u) &= \tfrac{4}{m^4}\left(m^4(1-s/m_X^2)^2 + (u^2+t^2)/8\right). \end{aligned} \qquad (2.10)$$

The definitions of the parameters in Equation 2.9 are as follows: θ is the scattering angle of the positron in the laboratory system, E is the total energy $(T_+ + m)$ of the positron. E_R is the resonance energy given by $E_R = \frac{m_X^2}{2m} - m$, $\rho = m_X/m$, $b^2 = (E-m)/(E+m)$. The Mandelstam variables s, t, u in Equation 2.10 can be expressed as $s = 2m(E+m)$, $t = -2m(E-m)\sin^2\theta/(1-b^2\cos^2\theta)$, and $u = 4m^4 - s - t$. In the CM system, the relationship among the Mandelstam variables is summarized by

$$\begin{aligned} u^2 + t^2 &= \tfrac{1}{2}(s-4m^2)^2(1+\cos^2\theta_{cm}) \\ u - t &= (s-4m^2)\cos\theta_{cm}. \end{aligned} \qquad (2.11)$$

Figure 2.3 shows the differential cross section at E = 2.773 MeV, corresponding to the GSI 810 keV e^+e^- sum-energy line.

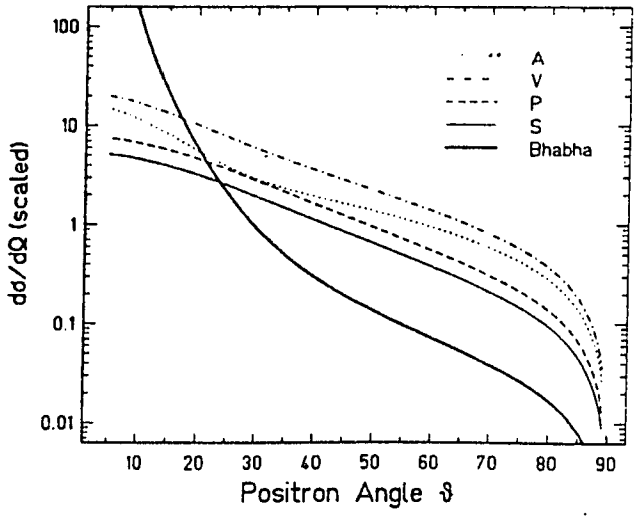

Figure 2.3: Differential cross-section in units of α^2/m^2 for e^+e^- scattering at E = 2.773 MeV. The thick line shows ordinary Bhabha scattering. The other lines refer to the resonant production of an intermediate state X^0 coupling with the vertex Γ_i^a. The assumed mass is M_{X^0}= 1.832 keV. This figure is reproduced from Fig 2 of [Rei87]

2.2.1 Normalization of e^+e^- Scattering Events

As discussed, the ratio of the expected peak resonance cross section to the QED Bhabha e^+e^- scattering cross section is less than 1% at the $g-2$ limit. To go beyond this limit, better sensitivity is essential. Thus, the normalization of the e^+e^- events has to have sensitivity much better than 1%. In the experiment, it is very difficult to control the flux of the bombarding positrons with such great stability. Fortunately, the Mott scattering (e^+ scattered by the nucleus) events make it possible to normalize the Bhabha events for flux variations. This has been reported previously, for example [Tse88a]. Equation 2.12 gives the differential cross section for the Mott scattering in the laboratory system

$$\left(\frac{d\sigma}{d\Omega}\right)_{lab}^{Mott} = \frac{(\alpha Z)^2 E^2}{4p^4 \sin^4(\theta/2)} \left(1 - \frac{p^2}{E^2}\sin^2(\theta/2)\right), \qquad (2.12)$$

where p is the momentum of the incident positron, E is the total energy of the positron, and θ is the scattering angle.

Normalizing the e^+e^- scattering events to this smooth curve enhances the appearance of the resonance, since it eliminates systematic effects arising from fluctuations in the e^+ intensity. The Mott events are registered by detecting a positively charged particle, and the Bhabha scattering events appear as a coincidence of two charged particles. A large number of γ-rays will be produced simultaneously by positron Bremsstrahlung in the target, and by 511 keV annihilation of positrons with electrons. To avoid false events due to γ-rays, the detector system must be able to suppress the γ background. This γ suppression is essential in achieving the sensitivity required by the experiment.

2.2.2 High-Z Targets vs Low-Z Targets

The choice of the electron target used as a scatterer to search for the resonance in the elastic e^+e^- scattering cross section has evolved from the high-Z elements to the low-Z elements in the past few years. In the first experiments of the most recent series of investigations, thorium and some other high-Z materials were utilized as targets. It was initially believed that Th target played a role in the production of the neutral particle. However, this choice of target makes observing the resonance signal difficult, due to the large fraction of bound electrons and their high momentum distribution. The maximum observable resonance peak in the Bhabha cross section is extremely sensitive to the momentum spread (not the energy spread, which is usually of the order of eV) of the electron scatterer , simply because of the e^+e^- scattering kinematics. In any elastic e^+e^- scattering experiments using a stationary target, it is impossible to obtain a resonance having a width as narrow as 0.5 keV, as reported by

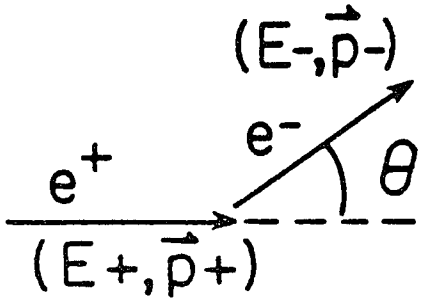

Figure 2.4: The kinematics of a positron scattered by an electron in motion

the group of Sakai et al. [Sak88], especially in a high-Z target. A kinematic analysis of the scattering will clearly explain this point, see figure 2.4.

Considering a positron and an electron with energies and momenta E_+, p_+, E_-, and p_- respectively, the invariant mass is given by

$$\begin{aligned} s &= (E_+ + E_-)^2 - (p_+ + p_- \cos\theta)^2 - (p_- \sin\theta)^2 \\ &= 2E_+E_- + 2m^2 - 2p_+p_- \cos\theta \\ &\simeq s_0 - 2p_+p_- \cos\theta. \end{aligned} \tag{2.13}$$

$s_0 = 2m(E_+ + m)$ is the invariant mass for a stationary electron. It is obvious that the electron momentum p_- is carried in the equation. For an electron in the target, $E_- \sim m$, $p_-/E_- \ll 1$. Therefore,

$$\begin{aligned} \sqrt{s} &= \sqrt{s_0 - 2p_+p_- \cos\theta} \\ &= \sqrt{s_0}\sqrt{1 - \frac{2p_+p_- \cos\theta}{s_0}} \\ &\simeq \sqrt{s_0} - \frac{p_+p_- \cos\theta}{\sqrt{s_0}}. \end{aligned} \tag{2.14}$$

For electrons with $\cos\theta = 1$ and $\cos\theta = -1$, a resonance width of $\Delta\sqrt{s}$ is expected

$$\Delta\sqrt{s} = \frac{2p_+p_-}{\sqrt{s_0}}. \tag{2.15}$$

Even in a low-Z metallic lithium target where the Fermi energy $E_F = 4$ eV, the electron momentum $p_- \simeq \sqrt{2mE_F} = 2.02$ keV. At the resonance mass $M_{X^0} = 1832$ keV, the broadened resonance width $\Delta\sqrt{s}$ is roughly 6.1 keV, which becomes 21.8 keV in the laboratory system when multiplied by the boosting factor M_{X^0}/m. This broadening is significant compared to a few keV energy width of the incident positrons and a few keV energy loss in the target. For details of the resonance shape, Henderson [Hen88] and other authors [Sch91] made a calculation using the Compton profile $J(q)$ of valence electrons in the target. Their result is given by

$$\sigma(E_+) = \frac{2\pi\rho\Gamma(\hbar c)^2(2J_i+1)J(q)}{mZ(\rho^2-4)p_+}, \tag{2.16}$$

in which

$$\begin{aligned} q &= \tfrac{1}{2}\left((2-\rho^2)p_+ + E_+\left((2-\rho^2)^2-4\right)^{1/2}\right) \\ \rho &= M_{X^0}/m. \end{aligned} \tag{2.17}$$

where J_i and Γ are the spin and the intrinsic width of the X^0, respectively.

Figure 2.5 shows the resonance width in the laboratory system for two low-Z targets, beryllium and lithium. The choice of a proper target should be guided by the specific experimental conditions. Basically, the lower the Z, the narrower the electron momentum spread. The lowest are hydrogen and helium, but at normal temperature, they are not solids. In the gas states, their target density is too small for experimental purposes. Therefore, they cannot be used as the scatterer unless an extra cooling system is added to the apparatus. The next low-Z targets are metallic lithium and beryllium. Beryllium is a commonly used target material because it does not react with air. Although lithium has a narrower electron momentum spread, it is difficult to

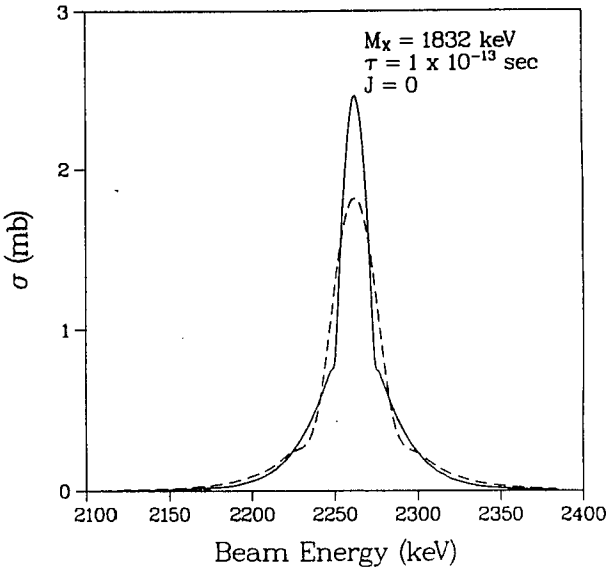

Figure 2.5: Broadened resonance width due to the target electron momentum only. The solid line and dashed line are for lithium and beryllium, respectively.

handle because it reacts with air and is quickly oxidized. For an experiment in which the positron beam has large energy spread, 30 keV FWHM, for example, reducing the electron momentum broadening from ~30 keV for beryllium to ~20 keV for lithium, produces little change in the final resonance width. In our experiment, however, the bandwidth of the positron beam was extremely narrow (less than 1 keV FWHM) and the energy loss in the target was about 3 keV. Hence, electron momentum broadening is an extremely important factor in determining the final resonance width. Choosing a lithium target obviously has the advantage of reducing the resonance width, and in turn, enhancing the possible resonance signal.

2.3 The Positron Beam

Producing a tunable mono-energetic positron beam with well-defined properties at energies of a few MeV was a principal part of the experiment. With the use of

a 3 MeV Dynamitron accelerator originally devoted to electrons, such a beam was designed and built At Brookhaven National Laboratory during the period from late 1986 to mid 1988. In the next few sections, the properties of the beam and related issues will be discussed.

2.3.1 Positron Production

The isotopes commonly used for positron production are ^{64}Cu, ^{58}Co, and ^{22}Na. ^{22}Na was chosen in this experiment because of its rather long half-life of 2.6 years compared to 12.8 hours for ^{64}Cu and 71 days for ^{58}Co, and its large positron emission branching ratio (90%). At Brookhaven a facility was built to produce such a positron source with high intensity, high positron yield. The source was deposited directly on a 6 μm thick, light-tight titanium foil window and encapsulated in a titanium case. The source had an activity of 250 mCi immediately after deposition and an active area 6 mm in diameter.

Positron Moderation

The positrons from a ^{22}Na source have a continuous energy spectrum. The end-point energy is roughly 550 keV. Clearly, these "raw" positrons can not be utilized in the experiment directly because of their wide energy spread. In the past decade, a large number of low-energy mono-energetic positron beams have been developed to study solid state phenomena, using a technique called *positron moderation.* Positrons from a radioactive source are implanted into a thin metallic foil called a *moderator.* In the process, the majority of the positrons ($\sim$ 77% for a 2000 $\AA$ W foil) are transmitted through the foil. A fraction of the implanted positrons will be slowed down to thermal energies. These thermalized positrons either annihilate with electrons in the foil in

a few hundred picoseconds, or diffuse to the surface. Because the work function for positrons in W is negative, positrons that reach the surface will be re-emitted with a kinetic energy equal to the absolute value of the work function.

The electron work function ϕ_- for a solid is defined as the minimum energy required to remove a bulk electron from the inside to the outside. This energy includes two parts: a contribution from the electron's chemical potential μ_- in the bulk, and a contribution from the surface dipole barrier. This dipole barrier prevents electrons in the solid from coming out of the surface. For the positron, the work function is defined the same way. The contributions to μ_+ include repulsion from the cores and attraction by the electrons. The work functions for positrons and electrons are given by

$$\begin{aligned} \phi_- &= +D - \mu_- \\ \phi_+ &= -D - \mu_+. \end{aligned} \tag{2.18}$$

where D is contribution of the surface dipole.

The moderation efficiency, which is defined as the ratio of the number of positrons implanted in the moderator to the number of moderated low-energy positrons emitted from the surface, varies widely according to the material of the moderator and its bulk purity, as well as its surface condition. A typical efficiency for a good metallic moderator is 10^{-4} [Wu90]. Because of the contamination of the moderator's surface usually the moderator has to be annealed after a few months of use to restore its surface condition. Figure 2.6 compares positron yield with and without the moderation process.

The moderated positrons have well-defined characteristics: they are mono-energetic (a few eV) and directional. The longitudinal kinetic energy is 3 eV for W(100) foil. The transverse energy spread is mainly contributed by the thermal motion of the positrons. The maximum transverse energy is roughly 75 meV at room temperature,

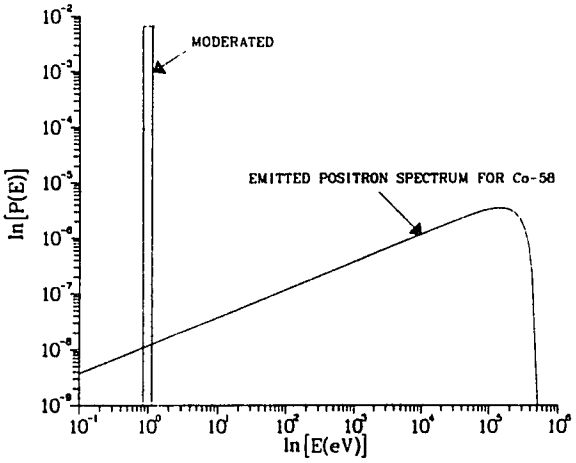

Figure 2.6: Comparison between positron yield from a moderator and the original β^+- particle energy spectrum for ^{58}Co (normalized). This figure is reproduced from reference [Sch88b].

which causes an angular spread of $\sim 10°$ with respect to the surface normal. In the experiment, the high-energy positrons which are transmitted through the moderator are removed by an optical filter and the beam transport system , as will be discussed in the next section.

Therefore, the initial beam conditions are: (1) starting energy of $\sim 3 \pm 0.2$ eV, (2) a maximum half-angle divergence of 10°, and (3) a radius of 3 mm.

2.3.2 The High Energy Filter

The positron flux from the moderator includes both low-energy moderated positrons and high-energy positrons transmitted through the foil. The moderator used in the experiment is a very thin W foil (about 3000 $\AA$), so that the majority of the positrons

will be transmitted through the foil, losing very little energy. Therefore, the low-energy positrons have to be separated from the high-energy ones. Between the moderator and the accelerator entrance an optical filter [Kum89] is placed to remove the unwanted high-energy positrons. This filter selects the moderated positrons and discards the remainder of the spectrum [Kum89]. The filter consists of a modified Soa immersion lens and a pair of symmetrical the einzel lens, as shown in figure 2.7. The Soa lens extracts the positrons from the moderator and the einzel lens transports the low-energy positrons through this 65-cm long filter to a small aperture of 6 mm diameter at the end of the lens. Because the lens operates at low voltages, it focuses only the low energy positrons and has very little effect on the trajectory of the high energy positrons. In this way, the number of the high-energy positrons is reduced by the acceptance angle before they enter the acceleration section of the Dynamitron. The long filter and the small aperture eliminate about 99.99% of the unmoderated positrons, and transport all of the moderated positrons to the entrance of the accelerator. Before entering the accelerator, the positrons have an energy of $\sim$ 400 eV. The remaining high-energy positrons are further reduced by a 90° double-focusing bending magnet in the beam transport section.

2.3.3 The Dynamitron Accelerator

The Dynamitron accelerator was initially built to accelerate electrons to energies in the range 0.5 MeV - 2.8 MeV with high intensity. To perform the elastic e^+e^- scattering experiment, major changes were made, including a reversal of the polarity to accelerate positrons and modifications in the terminal part of the machine to facilitate positron injection. Also, many vacuum tubes were replaced with solid state devices for increased stability and reliability. The 12 meter-long beam-transport pipe

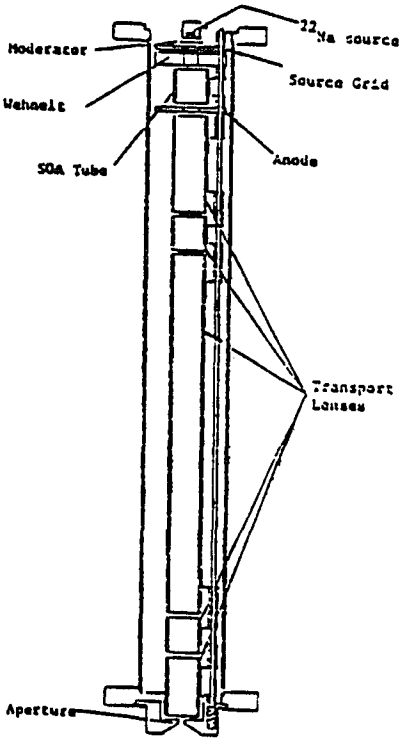

Figure 2.7: The high energy filter lens. This system reduces the high energy contamination to a factor of 10^{-4}.

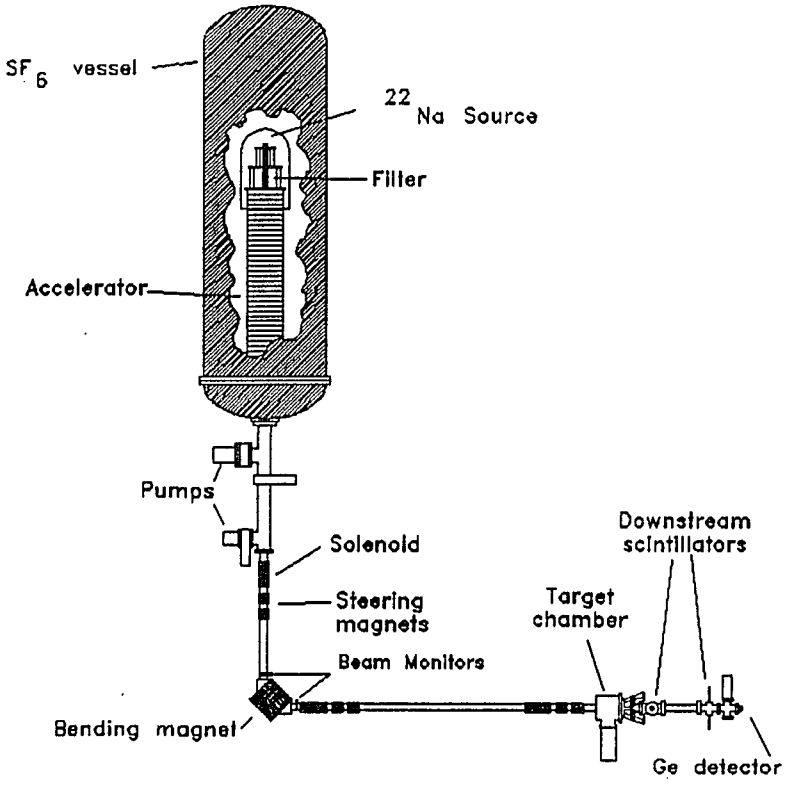

Figure 2.8: Schematic drawing of the Dynamitron accelerator and the beam transport system.

to guide positrons to the experimental target room was designed specifically for this experiment.

When the positrons enter the accelerator column, they are focused by two lens elements. The voltages to operate the lenses are tuned to produce the smallest possible beam size at the exit of the accelerator. The accelerator itself is powered by an RF-coupled Cockroft-Walton type, 3 MeV electro-static adjustable high-voltage power supply. The whole accelerator is surrounded by SF_6 at a pressure of 75 psi to protect against electrical breakdowns. All the electronics on the high-voltage terminal are powered by a DC generator driven by a motor near the base of the accelerator. These electronics on the top are used to extract positrons from the moderator and to operate

the high-energy filter. They are "floated" at the accelerator voltage.

Figure 2.8 shows a schematic diagram of the accelerator. A chain of cascaded rectifiers is capacitively coupled to the RF electrodes through the corona rings. Across the RF electrodes, an AC potential of roughly 100 keV is developed, driven by the power from the oscillator at a frequency of 125 kHz. The oscillator is a tuned-plate, untuned-grid, self-excited circuit. It takes a high voltage DC input and converts it to RF. The rectifier system is surrounded on each side by a column of corona shields. The RF power is coupled to the rectifiers through the large area capacitance of the corona shields. These rectifiers are arranged in such a way that, at any specific moment, only half of them conduct; therefore, charge is always being moved toward the terminal at the top of the accelerator. Thus, high-voltage is established at the terminal with respect to ground and its value is proportional to the input RF voltage. Positrons injected into the entrance of the accelerator are accelerated toward the bottom of the accelerator through 96 dynodes coupled to a voltage divider consisting of a chain of resistors. This chain of resistors draws a large portion of the current from the terminal compared to a very small beam current of $0.1pA$. Another current path is also formed to monitor the accelerator voltage and to provide feedback to the oscillator. By adjusting the input RF voltage, the positrons can be energized to any energy in the range 0.5 MeV - 2.8 MeV. Minimum ripple of the high voltage is 300V. With the existing feedback system, long-term drifts resulted in a few keV change in voltage. This slow effect was later corrected with a PC-based system to stabilize the output high-voltage through minor adjustments of the RF voltage.

The final characteristics of the beam are summarized in table 2.2. The beam size was measured both by observing a channel electron multiplier array (CEMA) plate at the target position visually and by moving a thin target across the beam.

e^+ Intensity	$5 \times 10^5 e^+/s$
Stray e^+	$< 1e^+/s$
Beam Energy FWHM	< 1 keV
Beam Size	1.1 mm
Beam Angular Divergence	0.5°

Table 2.2: Characteristics of the 3 MeV positron beam at the target position.

The results were consistent and the beam was determined to be $\sim$ 1mm in radius. From this beam size and the collimators in the beam line, the angular divergence of the beam was deduced to be $\sim$ 0.5°. It was difficult to extract an exact value for the beam energy width. Even with a HP-Ge detector at the end of the beam line, the measured positron profile could not be used to determine the FWHM for the real beam, because the Ge detector was located a few meters away from the target position where the positrons were focused, and also the positron intensity was reduced significantly by the beam-dump scintillators. S.D.Henderson [Hen88] employed two methods. The first measurement, which relied on steering of the beam across the Ge detector, showed a beam energy width of approximately 3 keV, while the second measurement, which relied on characterization of the unregulated RF on the high-voltage terminal, showed a width of $\sim$ 5 keV. A more precise measurement of the beam energy width at the target position was achieved as a by-product of another experiment described in chapter 4 during an observation of the single-photon e^+e^- annihilation process. As a result of the contribution of the beam energy width to the single photon annihilation spectrum, the width was determined to be less than 1 keV.

2.3.4 Beam Transport and Beam Monitoring

The initial positron beam is vertical at the exit of the accelerator. The beam is bent through 90° and transported to the experimental target room, using a set of

steerers and solenoids as well as one double-focusing bending magnet (figure 2.8). The transport system is designed so that the beam's symmetry is maintained when it reaches the target position. The beam is monitored at each stage for easy tuning and controlling. A detailed description and calculation are presented in reference [Kum89].

A set of "dog-legged" steerers placed 1.5 m below the exit of the accelerator assures that the initial beam enters the aperture centered on the beam pipe axis before the first focusing solenoid, a condition that is achieved when 511-keV γ rays arising from the annihilation of the positrons in the aperture are minimized in intensity. The first solenoid focuses the beam on the object focal point of the bending magnet, which is monitored by a plastic scintillator coupled to light guides. Both the solenoid and the double-focusing bending magnet are able to conserve the transverse symmetry of the initial beam. At the image focal point of the bending magnet is another thick scintillator with an aperture of a size that allows a ± 6 keV deviation of the tuned beam energy to pass and stops the remainder of the unmoderated high-energy positrons. The normal count rates on the object and image scintillators are 2 kHz and 4 kHz, respectively, when the beam is properly tuned. The beam is again transported by a solenoid 0.5 m away from the image slit and further focused by another solenoid on the target position. Between the target and the last solenoid, a set of steerers are arranged to adjust the final beam onto the central axis of the detector arrays.

2.4 The Detector System

The detector system employed in the experimental target room consists of an array of four multi-wire proportional chambers (MWPC's) and eight plastic scintillators for measuring the scattered particles from the Li target, a movable CEMA plate with a

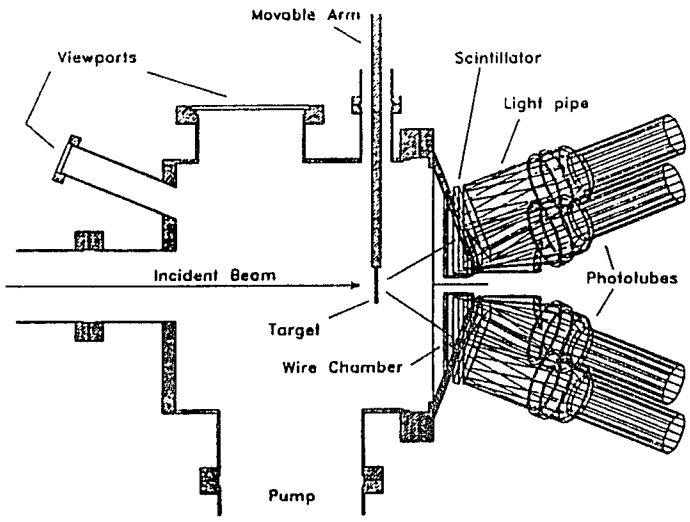

Figure 2.9: Schematic drawing of the detector system and target chamber employed in the experiment.

phosphorescent screen for visually tuning the beam, and a windowless ORTEC HP-Ge detector for measuring and monitoring the beam energy. The array of MWPC's provides two-dimensional position measurements of the scattered charged particles, and the array of scintillators generate the event triggers, as well as the energy read-out. With such a detector system, we are able to reconstruct the kinematics of the scattering events and suppress the unwanted γ-ray background. The large volume of the detector system covers an angular region from 16° to 50° in polar angle, and 75% of 2π in azimuthal angle with respect to the target position.

2.4.1 The Target Chamber

The positrons are finally transported to the target chamber (figure 2.9), where two long-arm linear feed-throughs provide the capability of moving the target and calibration source in and out of the chamber without breaking the existing vacuum. The

target employed in the experiment was a 55 μm lithium foil mounted on the movable arm on top of the chamber and connected to a small second stage chamber which can be separated from the main chamber to protect the sensitive lithium target from air when the main chamber is opened. The target position is monitored by a telescope through a viewport window in the chamber. During calibration, the target is raised up from its experimental position and a ^{207}Bi source is moved into its original position. The CEMA, mounted on a rotary motion feedthrough, can be inserted to provide correct beam tuning at the target position. A 8-in window located at the top of the main chamber provides a good view of the beam size and position as displayed on the phosphorescent screen during beam tuning. An 10-in cryopump mounted on the bottom of the main chamber maintains the vacuum in the chamber and the nearby beamline at about 7×10^{-6} Torr. The rather poor vacuum in the target chamber is caused by water vapor transmitted through a thin kapton window supporting the MWPC's as explained below.

The detector arrays are attached to a flange having the shape of a 4-folded pyramid, about 15 cm downstream from the target. The four MWPC's are symmetrically arranged around the target, with one in each quadrant. The tilting angle is selected so that the plane of the detectors is perpendicular to the path of equal-angle-scattered e^+e^- at the energy of interest. This arrangement maximizes the possibility of detecting both e^+e^- particles at a given detector volume. Behind the MWPC's, eight plastic scintillators are placed, with two of them covering the entire area of one MWPC. The MWPC's must operate at nearly atmospheric pressure in order to detect charged particles efficiently. A kapton window of 50 μm thickness is used to hold the gas pressure inside the MWPC's. The kapton window is supported by a set of 1/16 inch diameter stainless-steel wires with 1 inch separation. The choice of this window thickness is

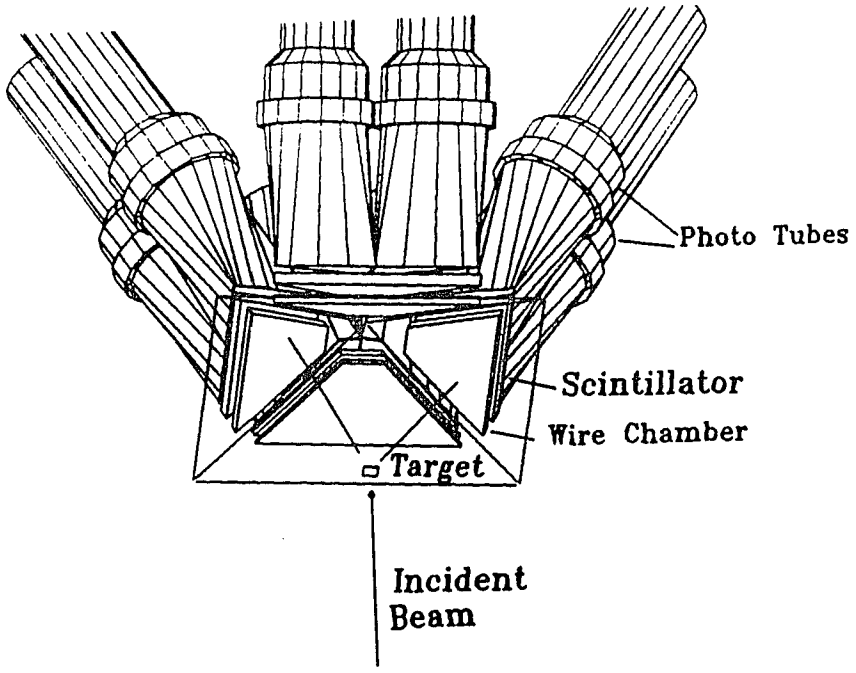

Figure 2.10: Schematic drawing of the multiwire proportional chamber.

a compromise in minimizing the energy loss, multiple scattering, and the diffusion of water vapor through the window to the target chamber. In the experiment, this rather thin window was chosen to support the $\sim$ 15 in^2 area of each MWPC; we gained the advantage of better position measurement of the scattering event at the price of a relatively poor vacuum.

2.4.2 The Design and Performance of the Wire Chambers

The multi-wire proportional chambers (MWPC's) were designed and constructed by the Instrumentation division of Brookhaven National Laboratory specifically for this experiment. The trapezoidal shape of the MWPC's (shown in figure 2.10) is the optimum for the acceptance angle matching the geometry of the target chamber.

The MWPC's are capable of reading out both the polar (θ) and azimuthal (ϕ) angles with a resolution better than 1° in both directions. The four MWPC's are identical; each of them has an active thickness of 1.1 cm filled with a gas mixture of 80% Ar and 20% CO_2 at a pressure slightly above atmospheric. Roughly 100 ion pairs are produced in this thickness of gas chamber for the minimum ionizing β particle passing through, thereby giving a detectable signal. The gas enters from the input end of the MWPC, regulated by an MKS 250B flow controller with a feedback system. The output of the gas path is left open to the air. The gas inside the wire chamber is ionized in the path of incident β particles. For particles with a given energy, the total charge produced obeys the Landau distribution (shown in figure 2.11). The peak position of the Landau distribution is associated with the detector efficiency. Therefore, efficiency drift of the MWPC's can be monitored by the shift of Landau peak. This feature was utilized in the data analysis to correct for any slight changes in the efficiency of the detector during long-term data collection.

The MWPC's are designed to read both polar and azimuthal angles on a single chamber. There are 39 anode wires evenly arranged over the active area of each MWPC along its longer dimension, with a spacing of 1.95 mm between any two adjacent wires. Identification of the signal from a single wire spacing gives a resolution better than 0.9° in the θ direction of the scattering angle. The ϕ angle readout is realized by another set of wires along the shorter dimension of the MWPC, independent of the anode wires. These 118 cathode wires are also evenly spaced, 0.5 mm apart. The resolution of the scattering angle in this direction is $\sim$ 0.5°. The fine spacing of cathode wires defines a plane about 2.5 mm behind the anode wires. In front of the anode wires, about 2.5 mm upstream, an additional 12.5 μm thick Al-Mylar cathode window is placed for added strength in supporting the wire chamber as well as for the

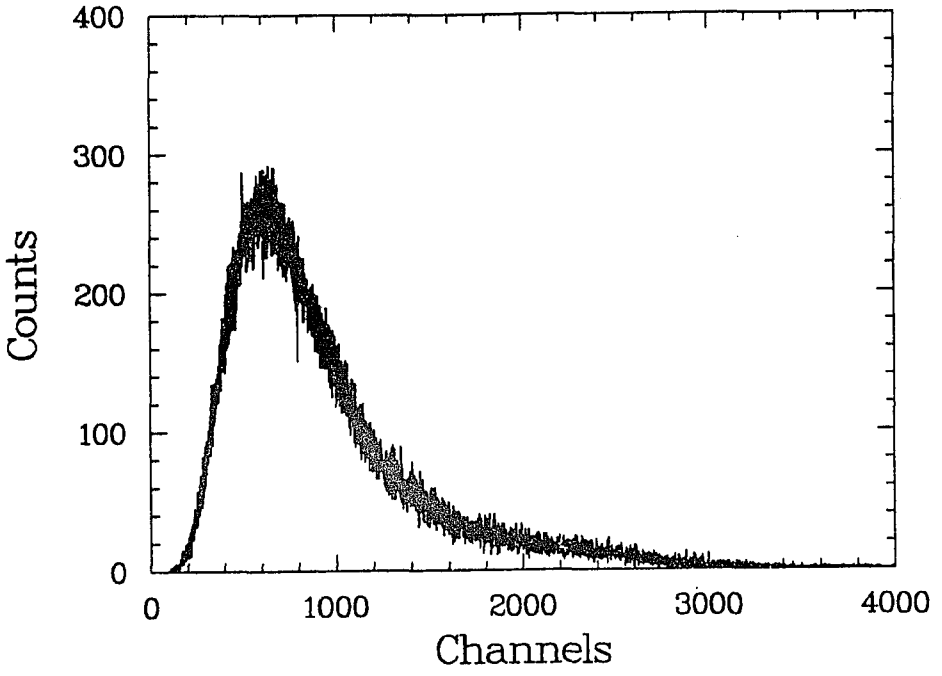

Figure 2.11: Landau distribution of energy deposited on the wire chamber at a beam energy of 2217.3 keV with a lithium target.

measurement of total ionization charge. There are two different ways to measure the total ionization charge in the wire chamber. One is via the sum of the readout of the signal height on both ends of the anode. The other is via the mirror image method on the front cathode window, since the total charge in the plane defined by the anode wires induces an image charge in the front cathode window. Both methods provide a measure of the total energy deposited on the wire chamber; that is, the Laudau distribution. As figure 2.11 shows, the Laudau distribution has a long tail on the high-energy side. These large energy deposition events, as well as the small energy deposition events, have to be taken into account carefully in the signal processing, since a very large portion of the signals are in these regions. Therefore, the electronics employed in the experiment must have a large dynamic range.

To increase the sensitivity of the wire chamber, a -1000 V potential is applied to the back window, forcing the electrons back to the active region of the chamber. A ~90% overall efficiency for the MWPC's is achieved. Two different methods of

reading out the signal for identifying the position of the scattered charged particles in the wire chambers are described in detail below.

θ Angle Measurement from Anode Readout

It is obviously inefficient and costly to connect each wire of the anode or the cathode to separate electronics. Instead, in practice, the anode signal readout is accomplished through resistive connection of the wires. Each of the 39 anode wires is attached to its adjacent wires through 800 Ω resistors, forming a chain of resistors, shown in figure 2.12. The two ends of the wires are connected to the appropriate charge-sensitive preamplifiers and amplifiers. Total ionized charges are partitioned to travel to the ends of the resistor chain according to the number of resistors from the incident position to the ends of the resistor chain. Thus, the charge pulse at the readout ends is proportional to the reciprocal of the number of resistors through which the current propagates.

Assume that the particle hits a position somewhere in the middle of the anode wire at position x, the total length of the anode wires being l. Then if the detected signals of the charge pulse at the starting point and the ending point of the anode are h_s and h_e, respectively, the relationship among these parameters is given simply by

$$\frac{x}{l} = \frac{h_e}{h_s + h_e}. \tag{2.19}$$

Unfortunately, the analysis is more difficult than that suggested by equation 2.19. The complication arises when a particle hits a position near either end of the anode wire. A very small pulse is produced on one end, while, on the other end, a very large signal pulse is produced. For the readout of the small pulse, the signal-to-noise ratio is small. Events have to be discarded if the signal is so small that it

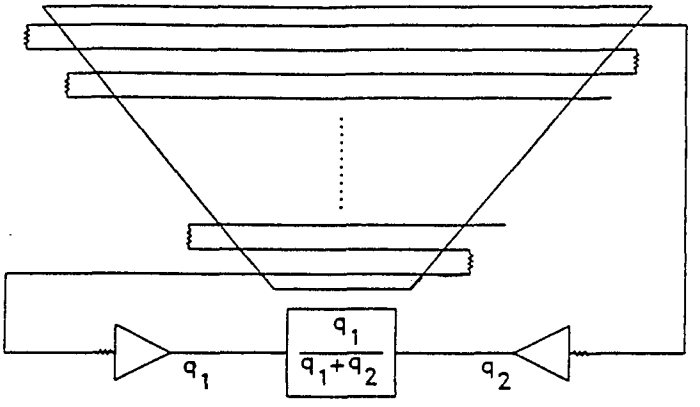

Figure 2.12: Resistive readout of the anode signal.

can not be distinguished from the noise. On the other hand, the very large signal readout can result in an overflow in the associated analog to digital converter (ADC). These problems will eventually affect the MWPC's efficiency. The Laudau energy distribution only makes matter worse.

To increase the sensitivity of the small signal readout, a narrow dynamic range ADC is preferred. However, to overcome the problem of the ADC overflow, a wide dynamic range ADC is desirable. In the experiment, on each end of the resistor chain, the signal is digitized with both a 2 V and a 8 V ADC. Therefore, there are four readouts for the anode in each wire chamber. By correctly selecting the appropriate ADC for signal processing in the software, good sensitivity on both sides is made possible. Accurate calibration of the two ADCs is very important. However, additionally, the pedestals of the ADCs have to be incorporated in the analysis to improve the resolution of position measurements. These issues will be presented in detail in chapter 3, when the calibration of the detectors is discussed.

ϕ Angle Measurement from Cathode Readout

The ϕ angle measurement is made possible by the 118 cathode wires 2.5 mm behind the anode wires. A different method is used to determine the incident particle's position in the ϕ direction. Instead of resistor chains, a group of two cathode wires are joined together and capacitively coupled to their adjacent groups through a series of delay lines of 1 μs total delay time. The reason for grouping two cathode wires together is that the cathode wires are very finely spaced and the typical dimensions of the the induced charge are larger than the spacing. When a mirror image is formed on the well-defined cathode plane, the time difference between the pulses reaching both ends of the cathode wires determines the position of the scattered particle. Since we

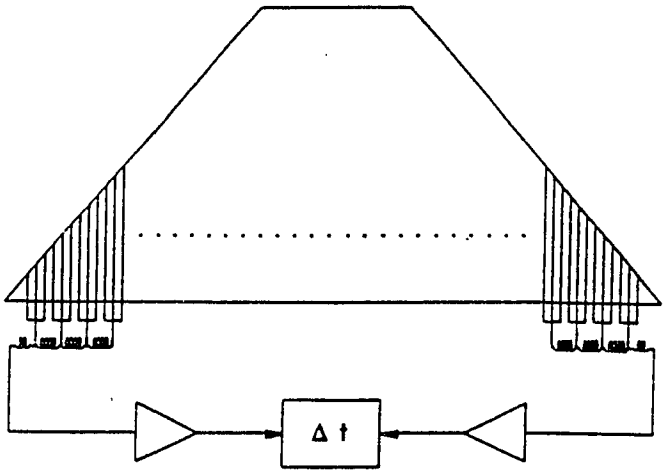

Figure 2.13: The layout of the cathode wires and the delay line readout scheme.

were only interested in the logic signal trigger of the pulses at the ends, the signal amplitudes were divided equally by terminating the cathode wires evenly at both ends. As in the case of the anode readout, let us assume that the incident particle's position on the cathode is x, and the total wire length is l. Then if t_s is the time the pulse takes to propagate through the delay line to the starting position of the cathode wires, and t_e is the corresponding time to the ending position of the cathode wires, parameters are related by

$$\frac{x}{l} = \frac{t_s}{t_s + t_e}. \tag{2.20}$$

Experimentally, it is the time difference, $\Delta t = t_s - t_e$, that is measured. Since the total time delay is a constant ($t_s + t_e = 1\mu s$), equation 2.20 is more appropriately written as

$$\frac{x}{l} = \frac{\Delta t + 1\mu s}{2\mu s}. \tag{2.21}$$

If the geometry of the detector system is known, the parameter x can be converted into the ϕ angle with respect to the target, but care has to be taken to extract the correct timing of the pulses. The pulses at both ends of the cathode line are first preamplified and then amplified. The amplified signals are sent to a zero-crossing discriminator from which two logic pulses are produced. These two logic pulses serve as the stop signal in the time-to-digital converter (TDC) for recording the delay time. Since we were only interested in the time difference between the two pulses, the time when the start signal was generated is not important as long as it falls in the TDC time limit window. In the experiment, the signal in the scintillator array behind the wire chamber produces the start trigger for the TDC. If the possible delay of the start trigger is considered, one would expect that the sum of the two delay pulses would

be exactly $1\mu s$. However, the noise in the system often causes premature firing of the discriminator. The reason for this is that noise added to the front region of the real pulse can result in a signal larger than the discriminator threshold (set to be 1.5 times higher that the average noise level). The correct stop trigger then comes after the premature trigger but is ignored in the common TDC module. This pattern will definitely lead to an incorrect kinematic reconstruction of scattering events and must be avoided in the experiment. To solve this problem, a LeCroy 4028 TDC is used. This TDC is able to record two different pieces of time information with two successive stop triggers within a short time slice of less than 2 μs. Thus, for each cathode firing, four times are obtained: two on each end of the cathode delay line. With this recorded information, it is easy to reconstruct in software the correct delay time from the four possible combinations by requiring the sum of the two delay times to be the closest to $1\mu s$. Figure 2.14 (a)-(d) shows the sum of delay times from four possible TDC stop combinations with $1\mu s$ represented by channel 500. Figure 2.15 is the sum time distribution with correct TDC stop pulses selected in software.

The readouts from both the anode and cathode of the MWPC's enable us to reconstruct information on the position of the scattering events in both θ and ϕ directions. The signal identification on each individual cathode wire results in 0.5° resolution the ϕ direction. Energy information of the events is provided by the scintillator array detectors.

2.4.3 The Design and Performance of the Scintillators

The MWPC's provide good angular resolutions (0.9° and 0.5° in the θ and ϕ directions respectively), but they do not give any information on the energy of the scattered

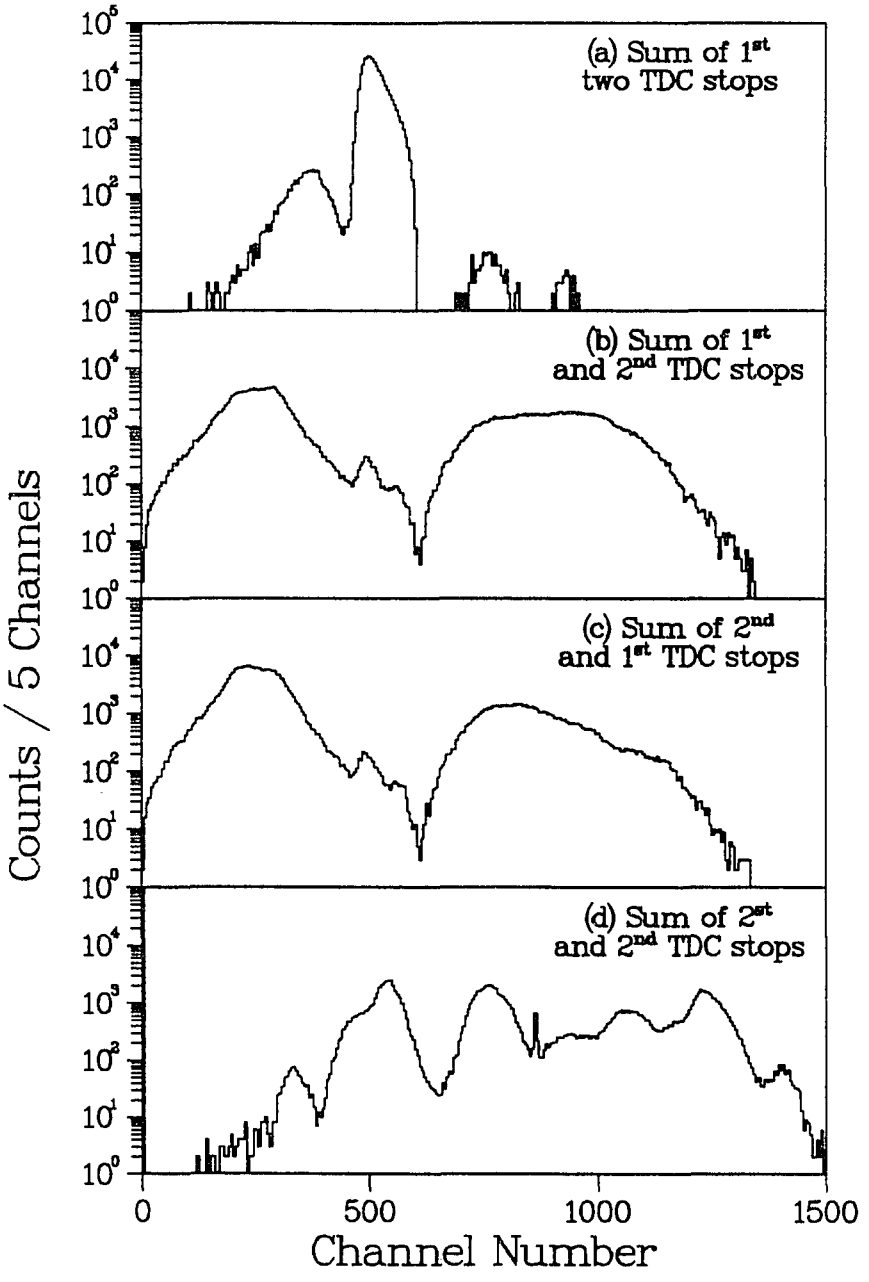

Figure 2.14: Sum-time distributions of the four possible TDC stop combinations. (The one selected with the correct 1 μs sum time delay in shown in figure 2.15.)

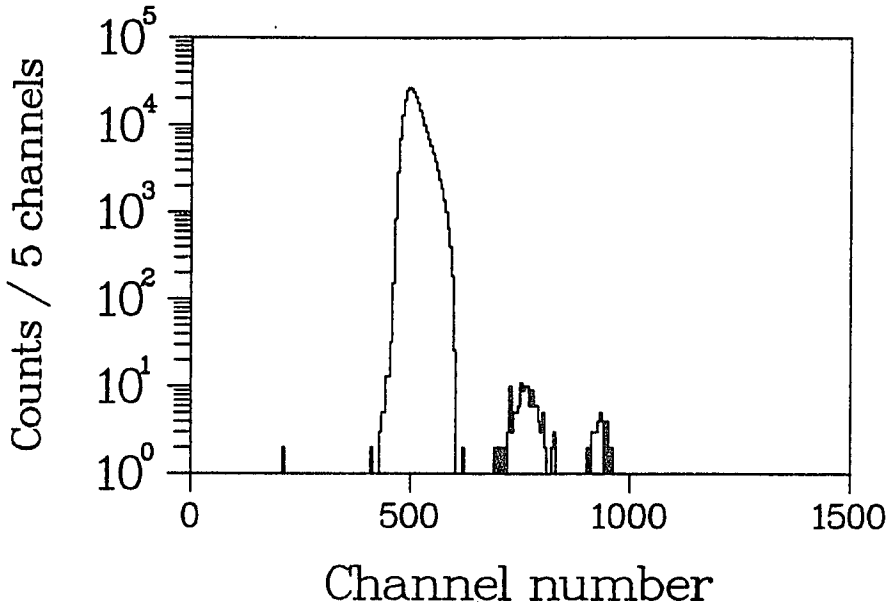

Figure 2.15: Correct TDC stops selected by software to satisfy the 1 μ s sum delay time condition.

particles. Electrons and positrons with a few MeV kinetic energy penetrate the chamber. Therefore, the scintillator array behind the MWPC's is designed to measure the energy of the particles. Each MWPC is backed up by two plastic scintillators with the shape shown in figure 2.16. Both "left-handed" and "right-handed" scintillators are glued to separate lucite light guides, which, in turn, are coupled to phototubes. The phototubes operate at 1200 V.

The unusual shape of the scintillator is due to the geometry of the MWPC's. The measurement of energy by the scintillator itself is rather poor because particles that strike near the edge of the scintillator generate a smaller signal than those hitting the middle of the scintillator due to different light collection efficiencies. This difference may amount to $\sim 10\%$ error in the energy determination, and would result in incorrect kinematics. The effect can be corrected if the dependence of the pulse height on the striking position of the particle is known. Fortunately, the MWPC's in front of

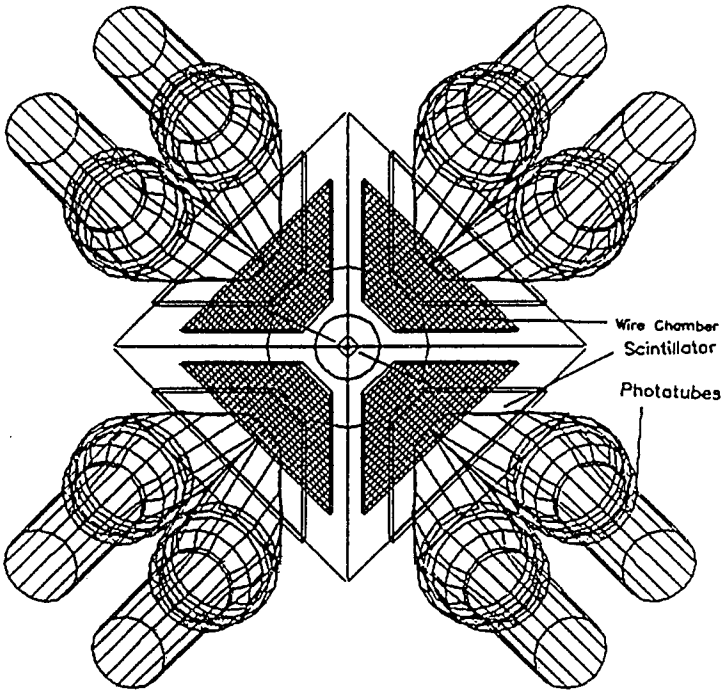

Figure 2.16: Schematic drawing of plastic scintillators.

the scintillators provide the position information necessary for the correction. S.D. Henderson [Hen88] calibrated the position dependence in his experiment to search for long lifetime e^+e^- states. The same correction of pulse height was adopted in this experiment.

The 1-cm thick plastic scintillators can completely stop positrons or electrons with energies up to 2 MeV. There may be a problem when the beam energy is higher than 2 MeV, since the plastic scintillators are not thick enough to stop the positrons at that energy. The invariant mass that we were interested in corresponds to beam energies in the range from ~1.340 MeV to ~2.360 MeV. Hence, at the high energy end, only part of the energy of the particle is measured, and a false energy identification results. This condition can happen only in the Mott scattering, however, since the scattered positrons retain all their incident kinetic energy if the target is not too thick. In Bhabha scattering, the positrons and the electrons share the incident energy, and thus neither of them normally has energy higher than 2 MeV. To correct for the "punch-through" energy, a set of Mott scattering spectra are taken in the energy region of interest, in steps of 200 keV. If there were no such energy straggling, the Mott scattering peak would coincide with the incident beam energy. Figure 2.17 shows measurements of the residual of Mott scattering energy (corrected for position dependence) and the incident beam energy.

If we express the real energy T_r as a function of the measured energy in the scintillator T_m up to the third order; that is, if T_r is written as

$$T_r = a_0 + a_1 T_m + a_2 T_m^2 + a_3 T_m^3, \tag{2.22}$$

the coefficients can be obtained from figure 2.17. They are listed in table 2.3 for all eight scintillators. (The numbering of the detectors is shown in the next section.) For greater accuracy, the pulse can further be corrected to subtract the ADC pedestal.

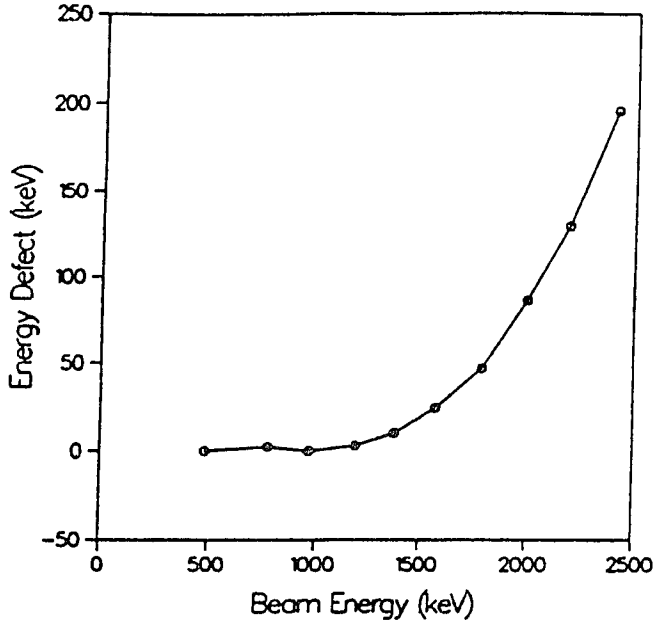

Figure 2.17: Positron straggling through scintillator 0.

A detailed discussion of the corrections of the position and energy measurements is presented in chapter 3, in which the calibration of the detector system is discussed.

2.4.4 Reconstruction of Vertex of Scattering Events

In the experiment, electrons and positrons cannot be distinguished in the case of e^+e^- scattering, since the MWPC's cannot identify whether the particle carries a

Scintillator	a_0	a_1	a_2	a_3
S0	12.29	0.9563	3.340×10^{-5}	0.0
S1	-38.25	1.155	-1.665×10^{-4}	5.032×10^{-8}
S2	-46.71	1.199	-2.374×10^{-4}	8.063×10^{-8}
S3	-2.09	1.026	-5.263×10^{-5}	2.591×10^{-8}
S4	-18.98	1.072	-8.032×10^{-5}	2.810×10^{-8}
S5	-38.75	1.168	-2.098×10^{-4}	8.180×10^{-8}
S6	-0.95	1.013	-2.928×10^{-5}	1.860×10^{-8}
S7	15.98	0.9469	2.780×10^{-5}	1.307×10^{-8}

Table 2.3: The calibrated coefficients for the pulse-height straggling correction.

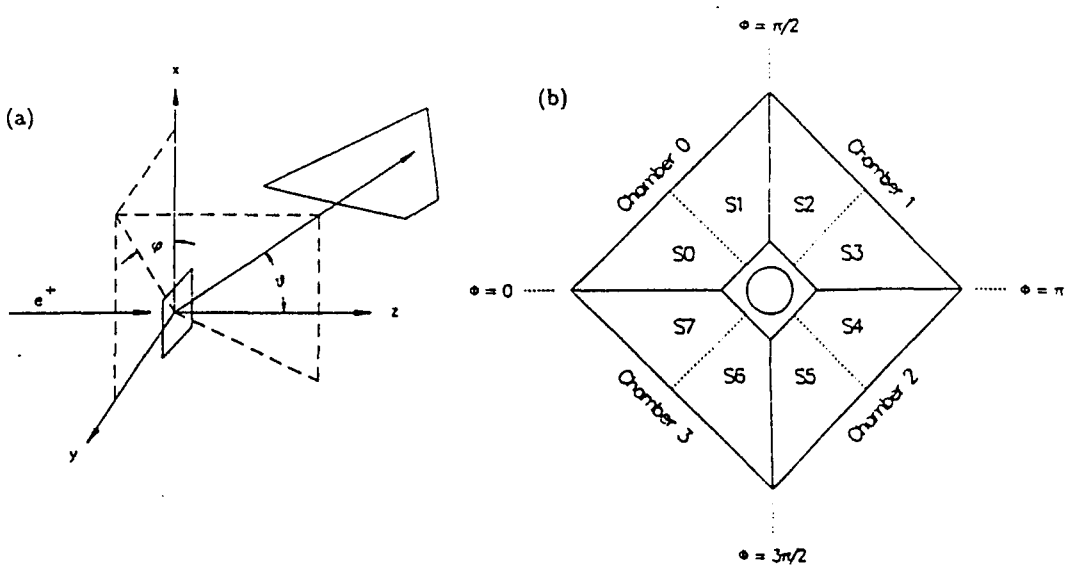

Figure 2.18: Angle definitions and detector numbering.

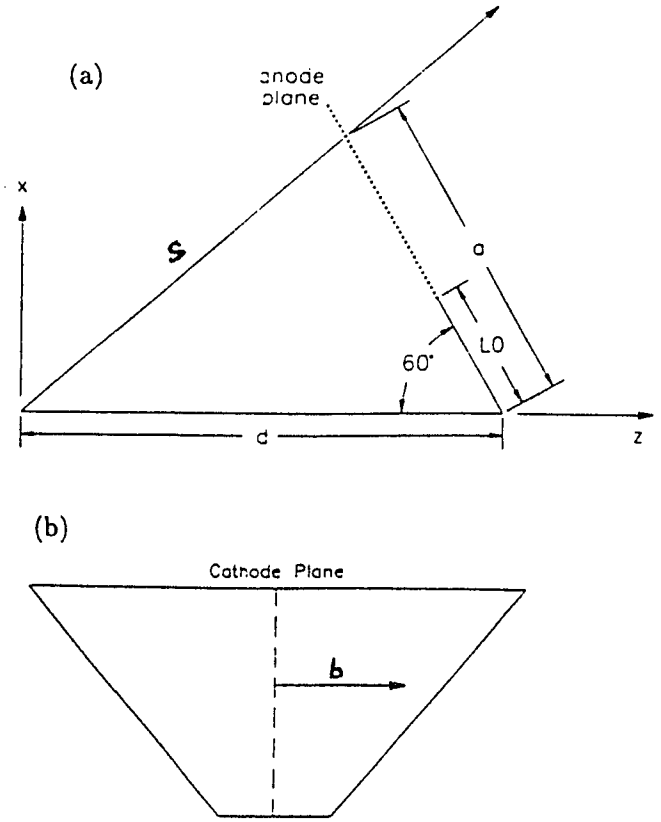

Figure 2.19: Variables defined for the vertex reconstruction.

positive or a negative charge. The measured cross section of Bhabha scattering is the sum of the e^+e^- events folded at 90° of the θ angle. However, the lack of charge identification does not affect the sensitivity in searching for the resonance in the cross section. From the information given by the wire chambers, the exact scattering angles of the particles in the laboratory system can be calculated. With the energy measurement, these laboratory angles can be easily converted to the center-of-mass system in which all the kinematic cuts for the e^+e^- scattering are taken.

The scattering angles θ and ϕ are defined in figure 2.18. The MWPC planes form an angle α of 60° with respect to the beam direction. If the distance from the hit to the intersection of the beam direction and the anode plane is a, the distance from the hit on the cathode wire to the bisector of the chamber is b (see figure 2.19),

the distance from the target to the intersection of the beam direction and the anode plane is d, the perpendicular distance from the target to the wire chamber is s, and the separation between the anode plane and the cathode plane is d_0, the coordinates (x, y, z) of the hit on the plane defined by the anode wires are given by

$$x = a \sin \alpha \tag{2.23}$$

$$z = d - a \cos \alpha \tag{2.24}$$

$$y = b \frac{s}{s + d_0}. \tag{2.25}$$

Parameters a and b can be determined from the MWPC's; d, s, and d_0 are fixed and predefined by the hardware setup. After the coordinates (x, y, z) are calculated, the scattering angles θ and ϕ can be obtained from the relations

$$\cos \theta = \frac{z}{\sqrt{x^2 + y^2 + z^2}} \tag{2.26}$$

$$\tan \phi\prime = y/x \tag{2.27}$$

$$\phi = \frac{\pi}{2} \cdot N + \frac{\pi}{4} + \phi\prime, \tag{2.28}$$

where N is the MWPC numbering as defined in figure 2.18. Then if it is known which of the MWPC's fired, the scattering angles θ and ϕ can be determined.

2.5 Data Acquisition

The data are acquired by a Micro-Vax II based system with a stand-alone Starburst processor. The Starburst is housed in a single width CAMAC module, and has a DEC J-11 CPU. A program in the Starburst's main memory controls the CAMAC crate. After the required data from other CAMAC modules are transported to the Starburst, the data are buffered in its main memory, and then transferred to the

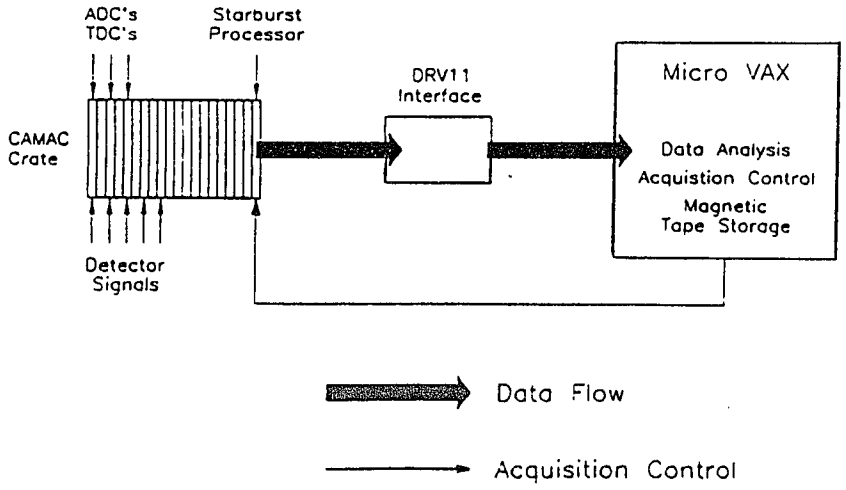

Figure 2.20: Flow chart of the data acquisition system.

host computer via a Q-bus interface whenever the buffering memory is full. There are two external interrupt lines in the Starburst. One is used to process the singles triggers (Mott scattering) and the other, to process the coincidence triggers (Bhabha scattering). With these interrupts and a scaledown scheme for the singles triggers, the system is fast enough to handle the data event by event and it is able to record events at a few hundred triggers per second. At the normal rate of ~100 triggers per second (corresponding to a beam intensity of $\sim$ 500,000 e^+/s), the data are transferred once per second. Finally, the raw data are stored on magnetic tapes by the host computer. Figure 2.20 illustrates the flow of the data acquisition system.

2.5.1 Overview

The Micro-Vax pre-processes the collected data on-line and records the data to magnetic tape storage devices. At the normal trigger rate, there is enough free time

for the host computer to complete some basic analysis on-line, and to plot the histogrammed data. The system can handle about $\sim$ 600 triggers per second. The data acquisition system is designed in such a way that the transfer of data from the Starburst to the host computer and from the host computer to the magnetic tape has top priority. Thus no data can be lost in between. The on-line analysis of the data is mainly for monitoring the experiment and notifying the operators of any possible malfunction of the devices involved, for instance, a trip of the voltage supply for the MWPC's generated by the effects of increased humidity in the target room on the MWPC's themselves. The final, more sophisticated analysis of data was done off-line using the DEC-Vax mainframe in the Computer Department of Brookhaven National Laboratory, after the entire experiment was finished.

2.5.2 Events of Interest

The system generates two different types of triggers: the singles trigger and the coincidence trigger that correspond to a Mott scattering event and a Bhabha scattering event, respectively. These two triggers generate the interrupts and start the related interrupt routines in the Starburst processor.

Singles Events

For positrons scattered by a nucleus in the target, only one of the eight-fold scintillators is fired. This is called *a singles event* in the experiment. This type of event has a higher triggering rate than the coincidence events in our detector volume. It is worth mentioning that the detection of a singles event does not necessarily mean that a Mott scattering event occurred. In the case of Bhabha scattering, because of the finite detector volume, it is possible that only one of the scattered particles (either e^-

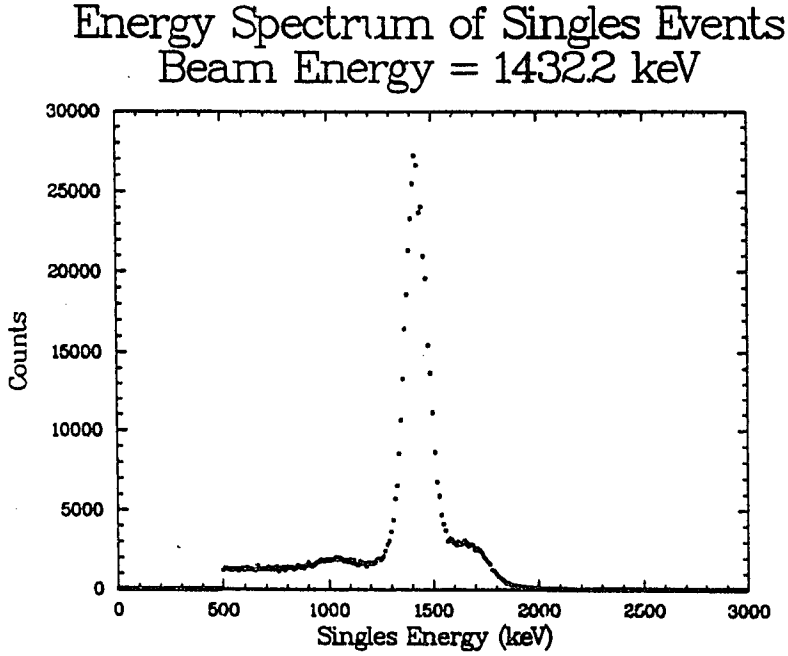

Figure 2.21: Energy spectrum of singles events. The events from Bhabha scattering produce a small bump in the low-energy part of the spectrum. The bump in the high-energy part of the spectrum is due to the pile-up of 511 keV γ-rays due to the annihilation of positrons with electrons in the scintillators.

or e^+) will fall in the detector volume, and thus a singles trigger may be produced. This phenomenon can be recognized in the energy spectrum of the singles events since it appears as a bump in the low energy part (See figure 2.21). The gamma-rays can also generate valid singles triggers, which can be eliminated by requiring valid signals from the corresponding MWPC.

Coincidence Events

Two or more firings in the scintillators in a time window of 45 ns are recorded as *a coincidence event.* This type of event is of the most interest. Two particles (e^+ and e^-) due to Bhabha scattering would generate such a coincidence trigger. Since both the QED and the resonant Bhabha scattering events have the same kinematics and produce such coincidence triggers (as was discussed at the beginning of this chapter

for the short-lived states), they can not be separated kinematically. The main purpose of the experiment was to search for an excess of such events at the resonance energy due to the s-channel Feynman diagram of the X^0 (see figure 2.1) as a signature of the existence of the X^0.

In practice, two scintillators in the same quadrant are grouped together for trigger generation. Therefore, two hits of particles in the same quadrant would only produce a singles trigger (see figure 2.24), if it ever happened. Theoretically, this would never happen, since correct kinematics for such events will require coplanarity in the ϕ angle, and thus, such events can only trigger firings of scintillators in two opposite quadrants. In order to study any possible unusual phenomenon, two hits in adjacent quadrants are also recorded as a coincidence event. In the final analysis, kinematic cuts required for a two-body decay/scattering are applied in the software. The normalized rate of coincidence events can be obtained as a function of the invariant mass. Possible resonances implied by this excitation function will be investigated.

2.5.3 Electronics

The main part of the data acquisition is handled by the Starburst and standard CAMAC modules, including analog to digital converters (ADCs), time to digital converters (TDCs), memories, and the input register. Also, NIM modules are used to provide logic for producing necessary triggers. All the discriminators, amplifiers, logic units, and fan-in/fan-out units are NIM bin modules.

Electronics for the Scintillator Array

Figure 2.22 shows the electronics used to process pulses from the scintillators. The scintillators supply information on pulse height, meanwhile, generate triggers and

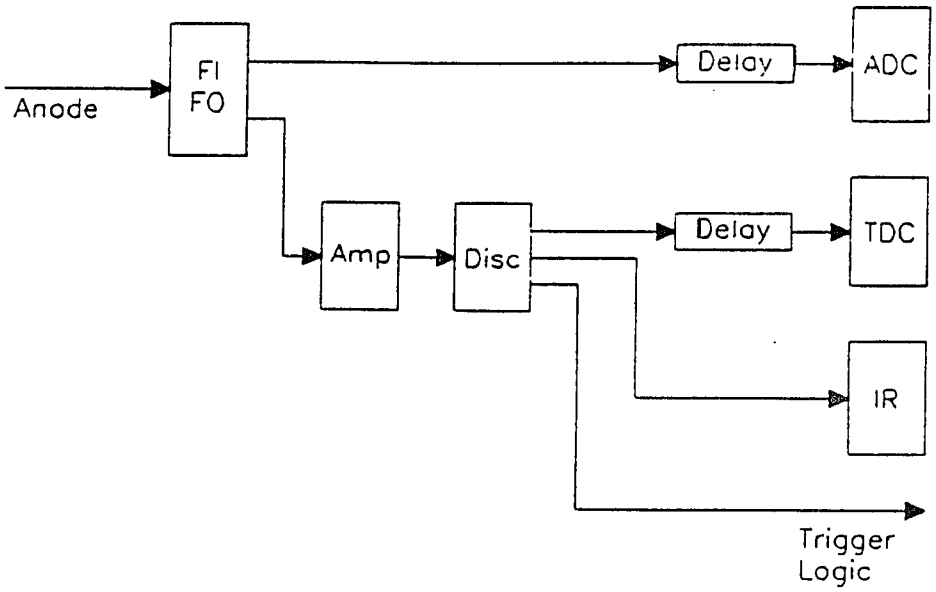

Figure 2.22: Scheme to process pulses for the scintillator array.

TDC starts. Four outputs are obtained from each scintillator.

The signal from the plastic scintillators is first amplified by the photomultiplier (PM) tubes and then fed into a LeCroy 428 linear fan-in/fan-out to increase its driving capability. After a fixed delay time to allow generation of the trigger and the ADC gate, the pulse is digitized by a 12-channel LeCroy 2249A ADC, in which only 8 channels are used, one for each scintillator. The signal is also routed to an amplifier in order to obtain better discrimination. This amplified signal passes a LeCroy 621 leading edge discriminator and the logic pulses generated by the discriminator have three outputs. One of them is again delayed, and serves as the TDC start for the wire chamber delay line measurement. Another provides the trigger logic and the third goes to the input register. This Bi Ra 2351 CAMAC input register has 12 channels. It records which of the 8 scintillators and 4 wire chamber front cathodes have fired. This information is used in the analysis to keep track of the activity of the detector system.

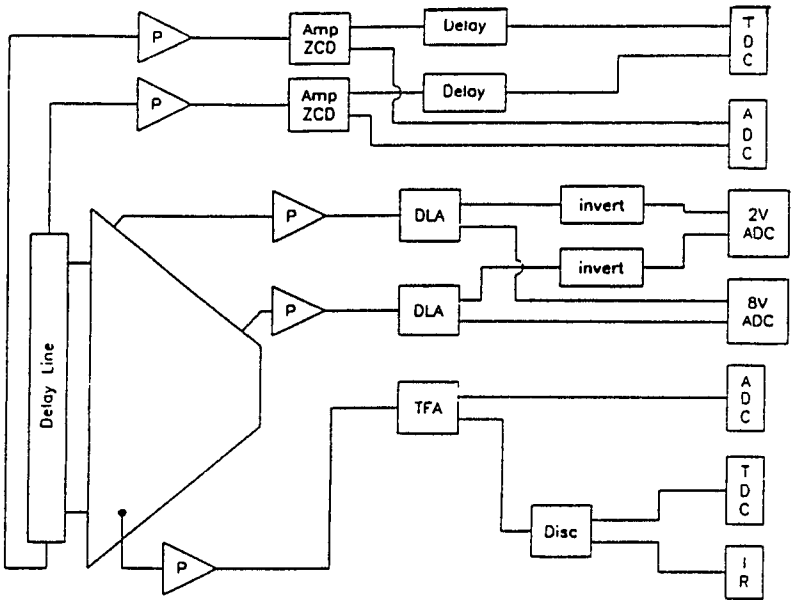

Figure 2.23: The electronics for processing signals from the MWPC's.

Electronics for the MWPC's

There are five outputs from each MWPC: one pulse from the front cathode window, two from the wire chamber resistive anode readout and two from the wire chamber cathode delay line readout. Figure 2.23 is the schematic drawing of the configuration.

Anode Resistive Readout: The signals from the two outputs of the anode wires are first amplified by charge sensitive preamplifers and then by delay line amplifiers. As described earlier, each amplified output is digitized by both 2-V range and 8-V range ADC's.

Cathode Delay-line Readout: The signals from the two outputs of the cathode wires are preamplified. The signals are then again amplified by the amplifier/zero-crossing discriminator units. The logic pulses from the discriminators provide the stop pulses for the TDCs, while the start pulses are generated by the scintillators. The pulse height is also recorded by the ADC's to monitor the stability of the discriminator threshold.

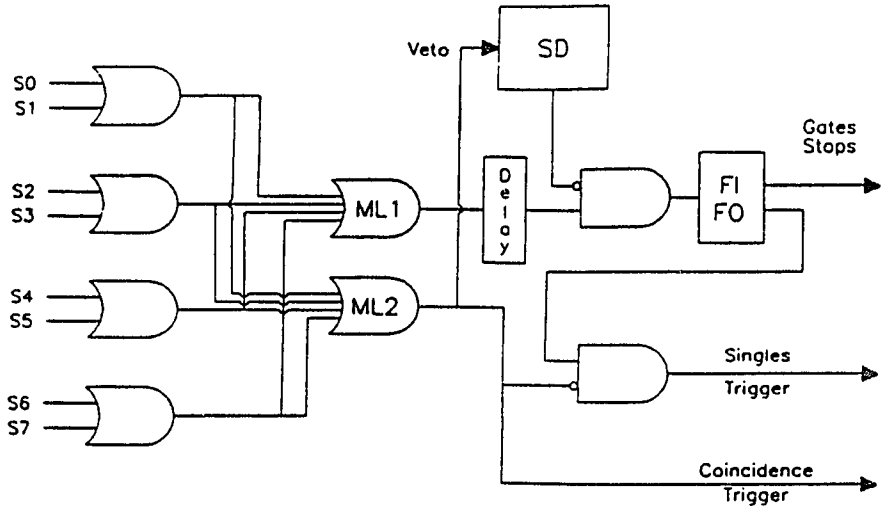

Figure 2.24: The scheme for generating logic triggers.

Front Cathode Window Readout: The front cathode window provides information on the total charge collected in the wire chambers. After the signal is amplified, the pulse height is recorded in the ADC, as shown in figure 2.11. There is another route, after the timing filter amplifier, shown in figure 2.23. The signal is fed to a discriminator, which in turn, creates two logic outputs. One is connected to the CAMAC input register for keeping track of hits and the other goes to a TDC to supply additional timing information on the wire chambers.

Generation and Scaledown of Triggers

The triggers from the two scintillators in the same quadrant are OR-ed together. Figure 2.24 shows the logic for the trigger generation. Outputs from the grouped triggers are decoded by two EG&G C315 majority coincidence modules, one of which is set to level 1 for singles triggers, and the other is set to level 2 for coincidence triggers. The coincidence trigger is generated directly from the output of the second

majority module. However, the singles trigger is a little more complicated. One problem is that the singles trigger has to be inhibited in the presence of the coincidence trigger. The other problem is that the singles trigger comes in at a rate of ~200 times faster than the coincidence trigger. This high trigger rate (~ 2 kHz) introduces a large dead-time into the data acquisition system, and the coincidence events, which are of primary interest, could be blocked. Therefore, hardware to scale down the singles triggers was built. This is achieved by using a 1 MHz clock which is first prescaled by a factor of 100, using an ORTEC 706 prescaler. A gate of adjustable width is generated by this signal every 0.1 ms. By selecting the correct gate width, the active time of the singles circuit can be adjusted. This gate to open the singles circuit is AND-ed with the coincidence to veto the singles trigger when the coincidence trigger is available. With this method, only ~ 5% of the singles triggers are accepted in the experiment. Both active time and the total time of the gate are recorded and used to correct for the scaledown effect.

Deadtime

The deadtime of the system is introduced when the data in the CAMAC modules are read. As the experiment begins, a CAMAC scaler counts the pulses from a 1 MHz clock which records the total running time of the experiment. Another scaler is used to record the active time, in the following way. At the start of reading data by the Starburst, a busy signal is generated to inhibit the modules from their normal activities. The first scaler is not affected by this busy signal; however, the second scaler is disabled. When the data transfer is finished, the busy signal is cleared. Hence, from the counts in these two scalers, the deadtime of the system can be calculated. During the entire data collection, the deadtime is less than 2%.

2.5.4 Data Collection

Overview

The experiment to search for short-lived states coupling to e^+e^- began immediately after the search for long-lived states [Hen88] had finished. The whole set of experimental runs lasted for eight months from March to October, 1990. The Bhabha scattering cross section was systematically investigated in the invariant mass region from ~1560 keV to ~1860 keV, which covered the entire mass region suggested by the GSI heavy-ion data. Compared with other experiments performed thus far using direct plastic e^+e^- scattering methods, ours covered the largest mass region, and at the same time, retained high sensitivity throughout the region.

A large amount of Bhabha scattering data was taken for 260 different beam energies, from ~1360 keV to ~2363 keV, in steps of ~ 3 keV. The expected resonance width (FWHM) was ~20 keV for a thin lithium target in the laboratory system. Thus, there would be about 10 points in the resonance peak which could be identified with ease. The data were taken very carefully following the preset procedures described below.

Beam Energy Increment and Balancing

For each step in energy, the positron beam was tuned to achieve the best beam quality. Since the double-focussing bending magnet must be tuned for each energy, the magnet current was adjusted first when a small change in beam energy was required. A scaling factor for the magnet current could be obtained from the on-line software. After the current in the bending magnet was set for the required beam energy, the energy was then adjusted until the beam spot was slightly off the center hole of the image slit, giving a count rate of 30 kHz on both sides of the required energy. The average value

of these two energies was basically the required energy set by the bending magnet. Fine tuning around this value was sometimes necessary.

After the beam energy was determined, the focussing solenoids had to be fine-tuned. At this stage, the target was removed from the experimental position, and the channel plate was moved into this position. The beam spot could be viewed on the phosphorescent screen at the back of the channel plate. The current in the first solenoid was adjusted to minimize the count rate on the object slit of the bending magnet to ensure the precise entrance of the beam to the bending magnet. The current in the second solenoid was also tuned, until a small, round beam spot was seen on the phosphorescent screen.

Next the beam was aligned with respect to the detector system; that is, the beam was adjusted to be on the central axis of the MWPC and the scintillator arrays. This was not accomplished visually. The detector system in the experiment was designed symmetrically around this central axis, which was very helpful for centering the beam. The channel plate was removed from the target position and the target was moved to its experimental position. By adjusting the x and y steerers upstream of the target chamber to balance the Mott scattering count rates on the four MWPC's, the correct beam position could be determined.

The procedure mentioned above was only appropriate for a small adjustment in the energy of the positron beam, because the first set of steering elements after the exit of the beam from the accelerator might be out of adjustment, due to errors accumulated from many small energy increments. This part of the tuning was not simple and had to be done very carefully. The tuning involved adjusting the beam through all the existing beam monitoring detectors. Fortunately, this adjustment was only required once the accumulated beam energy increments totalled about 150 keV

away from the previously set value.

Calibration Run

The detectors were calibrated daily to account for any possible gain drift of the system. The target was raised from its normal experimental position, the calibration source ^{207}Bi was moved into the target position by an external arm, and γ-ray sources ^{60}Co and ^{228}Th were placed near the HP-Ge detector. Another calibration source ^{137}Cs was permanently situated in the beam tube near the HP-Ge detector, and off the axis. Before the run started, the valve upstream from the last focussing solenoid was shut to block the beam. The MWPC's, scintillators, and the HP-Ge detector were then calibrated. A detailed discussion of such calibration is presented in chapter 3. The calibration information on the detectors was used for the day's data.

Halo Run

After each energy tuning and before the actual run, the target was raised. The effect of the beam on the detectors was measured. This 15-minute run was called the "halo run". The purpose was to measure the exact beam energy and to study the beam quality after the tuning, as well as the existing background. Because there was no target in front of the HP-Ge detector, with the acquired calibration information, the beam energy could be precisely determined. Ideally, there should be no triggers on the MWPC's and scintillators. In practice, cosmic ray background was seen in the spectra, and also, if the beam was not properly tuned, stray beam positrons appeared in the spectrum at the beam energy. Figures 2.25 and 2.26 show the singles spectra for a well-tuned beam and an improperly tuned beam, respectively.

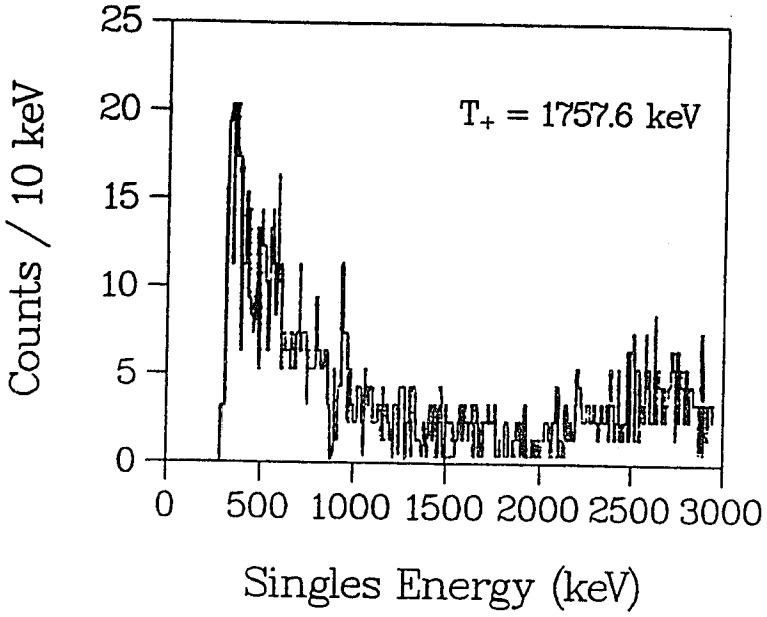

Figure 2.25: The energy spectrum of singles events. There are no stray beam positrons at the beam energy of 1757.6 keV. The background is mainly from cosmic rays.

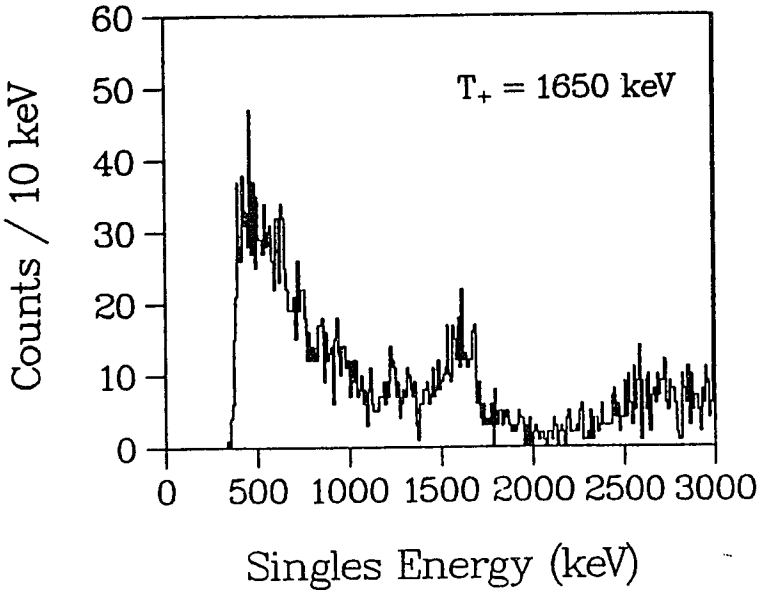

Figure 2.26: The energy spectrum of singles events. Stray beam positrons are observed at the beam energy of 1650.0 keV. This suggests that the beam is not properly tuned.

Mott and Bhabha Events Runs

The runs for Bhabha and Mott scattering events were taken after the halo run was finished. The thin lithium target was lowered into the proper position and checked with a telescope to maintain reproducibility of the exact position. For each new energy, more than 200,000 coincidence events were collected. At the normal beam rate, it took $\sim$ 4 hours to collect data with sufficient statistics.

2.5.5 The On-Line Analysis Software

During the three different runs described above, the progress of the experiment was monitored interactively by the on-line analysis software. The program ran in the DEC Micro-Vax II host computer. The main purpose of the real-time analysis of the collected data was to ensure that the experiment was proceeding satisfactorily and to provide the user with an overall knowledge of the data being taken. Simple kinematic cuts on the data could be applied in the on-line software. Thus, any possible strong resonances at certain energies, or unexpected exotic phenomena, could be observed immediately during the course of the experiment.

Chapter 3

Data Analysis and Results

3.1 Overview

The entire data collection for the experiment was finished in October, 1990. Elastic Bhabha and Mott scattering events were investigated in the invariant mass region from $\sim$ 1560 keV to $\sim$ 1860 keV. The accumulated data were stored on $\sim$ 400 magnetic tapes, including calibration runs. The data were analyzed using the off-line software for about half a year. Possible resonances in the Bhabha scattering in this energy region were studied carefully. With the off-line software, the necessary kinematic cuts for a two-body decay from a neutral particle were taken into account in the data analysis. No evidence of resonances was observed in the entire mass region searched in the experiment with the sensitivity of 0.27%. Compared with the statistical uncertainty ($\sim$ 0.26%), the systematic error was small. Constraints on lifetimes of the hypothetical light neutral object implied by the GSI heavy-ion data were set for both scalar and vector couplings. To date, this experiment has provided the tightest bounds for the X^0 on the short lifetime end ($\tau \sim 3.0 \times 10^{-13} s$), by means of direct

elastic e^+e^- scattering. Detailed information on how the lifetimes were extracted are presented in this chapter.

A paper reporting the results obtained in this experiment has been published in **Physical Review Letters**, together with another paper describing the search for long-lived states coupling to e^+e^-[Wu92, Hen92].

3.2 Calibrations

Calibration runs were performed daily, producing 1/4 of the total collected data. The experimental apparatus to search for the light neutral object was designed to have a high sensitivity to the e^+e^- scattering cross section, and a deviation of $\sim 1\%$ can be easily detected. Therefore, the calibration of the detector system played an important role in the overall resolution obtained in the experiment.

3.2.1 Calibration of Energy Measurement

Calibration of Beam Energy

For the precise reconstruction of the kinematics of the scattering events in the CM system, an exact knowledge of the positron beam energy is needed. The beam energy measurement was done using a liquid N_2 cooled windowless HP-Ge detector. Several γ rays of known energy obtained from ^{228}Th and ^{60}Co sources provided good linear calibration of the detector, covering the energy range from $\sim$ 1 MeV to $\sim$ 2.6 MeV. However, because of the gradual deposition of vapor on the detector, the electrons and positrons suffer an energy loss in accumulated ice on the detector surface. This deposition rate corresponded to $\sim$2 keV energy loss per week. The ice could be eliminated by warming the detector up to room temperature, but this was time

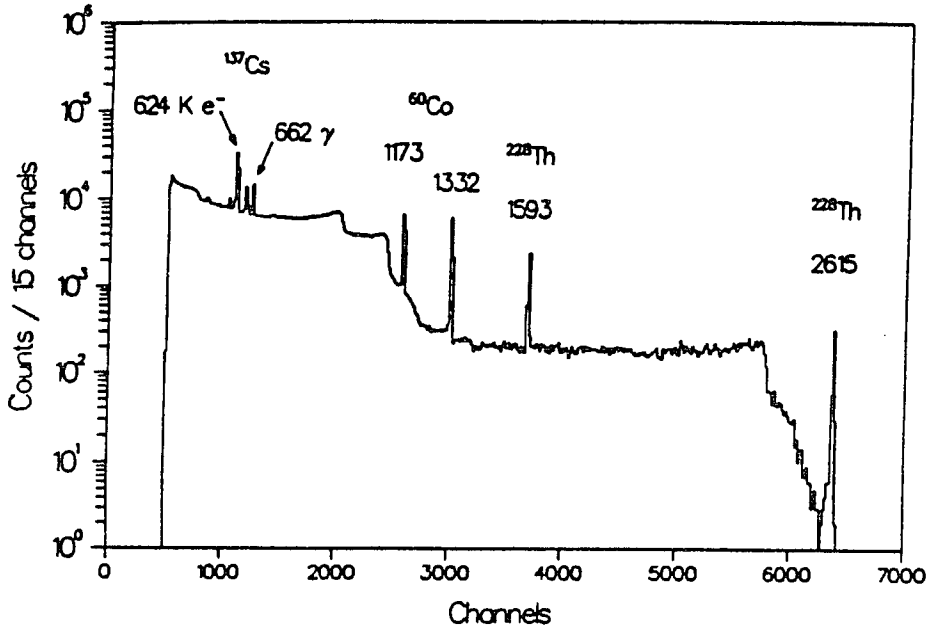

Figure 3.1: The energy spectrum obtained for HP-Ge detector calibration. Energy lines from several calibration sources are labeled, including the 0.624 MeV conversion electron line.

consuming. In practice, the energy loss was compensated by measuring the deviation of the 0.624 MeV conversion electron line obtained from a ^{137}Cs source, which was permanently in the vacuum, 15 cm from the HP-Ge detector and 5 cm off the beam axis. The difference between the energy measured by the HP-Ge detector (calibrated by the γ-rays) and the known value of 0.624 MeV determined the energy loss in the ice. This amount of energy was added to obtain the correct positron beam energy. Figure 3.1 shows the energy spectrum for calibrating the HP-Ge detector.

Calibration of the Energy Measurement of the Scintillators

As mentioned previously, the calibration of the scintillators was complicated. First, it required information on the hit track from the MWPC's. Second, unlike the HP-Ge detector, the plastic scintillators have rather poor energy resolution. Thus, sophisticated fitting was required to determine the peak positions of various energy lines.

The final value for the energy obtained by the scintillators has to go through the following correction procedures, in this order.

(a) pulse-height vs hit track correction.

(b) converting the corrected pulse-height obtained from procedure (a) to energy by the previously obtained linear calibration parameters.

(c) correction for the straggling effect of particles in the scintillators.

The energy of positrons after Mott scattering at 1525 keV was measured by the scintillators. Figure 3.2 shows the relative pulse height as a function of position. A deviation of $\sim$ 10% was found, due to different light collection efficiencies at different positions on the scintillators. To correct for this effect, first, each of the scintillators was divided into $\sim$ 100 small elements. By subtracting the ADC pedestals, the pulse height at each element was determined. Then a scaling factor for each element in the scintillator was obtained by normalizing the pulse height in the element to the average pulse height for the Mott-scattered events measured by the entire scintillator. In the analysis, the raw pulse-height was first corrected by this array of scaling factors, before the energy calibration was made.

The scintillators were calibrated with the conversion electron lines obtained from ^{207}Bi placed in the normal target position. Two γ ray lines at energies of 0.570 MeV and 1.064 MeV from the transition of ^{207}Bi to ^{207}Pb produce four e^- lines from K and L shell conversions, two for each γ-ray line. Figure 3.3 shows the high resolution measurement of the energy spectrum from the ^{207}Bi source by the HP-Ge detector. Six mono-energetic lines were clearly observed, including the unconverted γ rays. The four conversion electron lines are at 0.482 MeV, 0.554 MeV, 0.976 MeV, and 1.048 MeV.

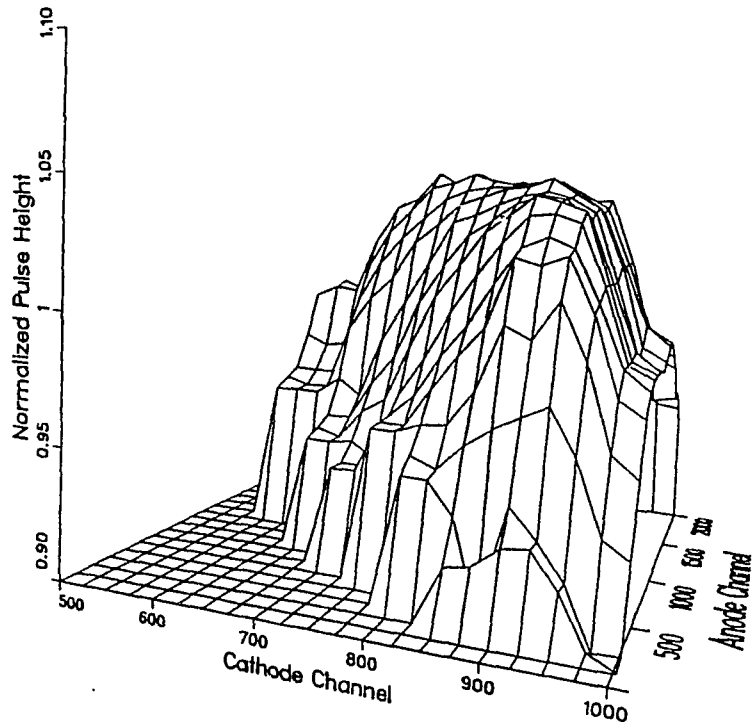

Figure 3.2: Pulse height distribution of Mott scattered positrons at 1525 keV in scintillator 0.

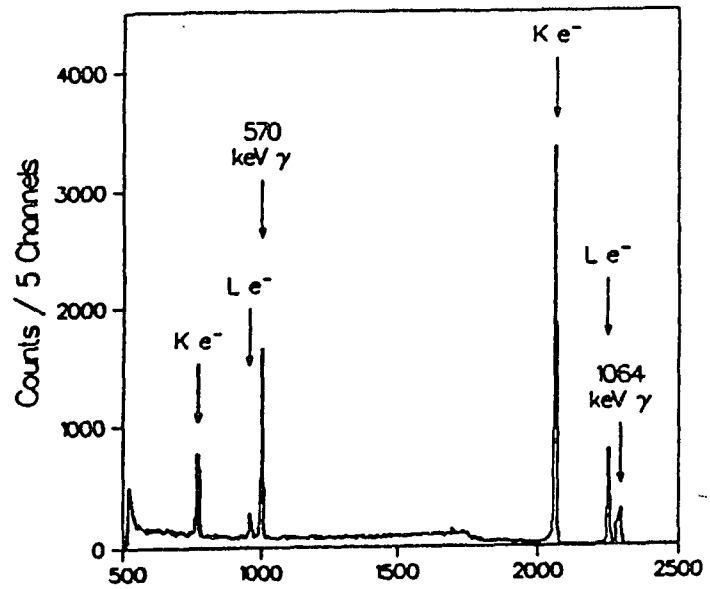

Figure 3.3: Energy spectrum of ^{207}Bi from the HP-Ge detector.

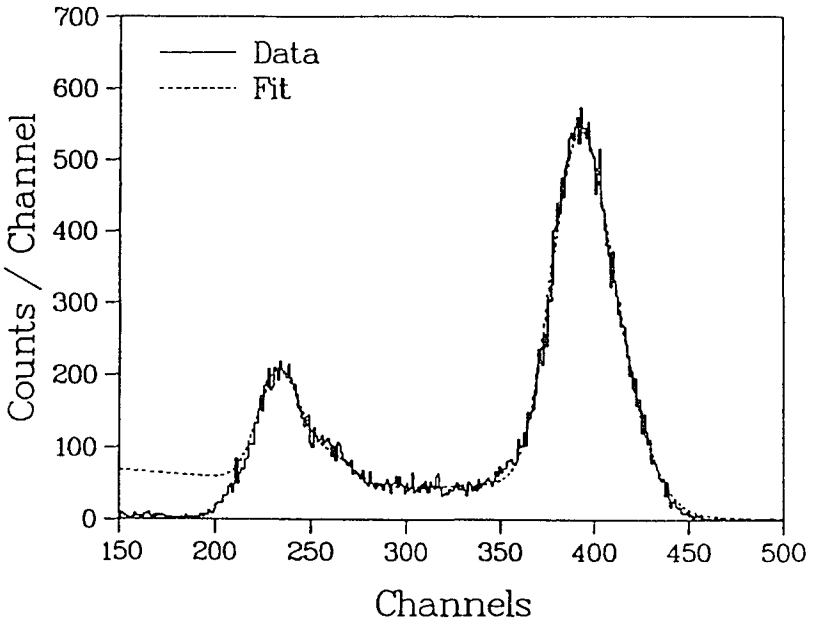

Figure 3.4: Energy spectrum of ^{207}Bi from the scintillator. The solid line and the dotted lines represent the data and the fit, respectively.

With the measurement made by the scintillators, however, K and L conversion lines with a small energy separation are indistinguishable. The energy spectrum obtained from the plastic scintillator is presented in Figure 3.4, after the pulse-height correction and the pedestal subtraction were applied. In the data analysis for the scintillator calibration, the γ-ray background was eliminated by requiring valid firings of the MWPC's. This γ background contributed $\sim$ 50% of the triggers in the scintillators.

The pulse positions of the four conversion e^- lines were extracted by fitting with an assumed functional form, including all the line spectra and the Compton background. The functional form is given by,

$$f(x) = \sum_{n=1}^{n=4} f_n(x) + c(x) + b(x). \tag{3.1}$$

In equation 3.1, $f(x)$ is the collected count distribution, x is the channel number,

and $f_n(x)$ are the four electron conversion lines with known peak energies E_n for $n = 1,2,3,4$. The functions $c(x)$ and $b(x)$ are the contributions from Compton scattering and the linear background, respectively.

Standard Gaussian distributions of the e^- lines are

$$f_n = \frac{I_n a_0}{\sigma_n} e^{-0.5(x-a_n)^2/\sigma_n}, \tag{3.2}$$

where a_n for $n = 0$ to 8 are the fitting parameters. I_n are the known relative intensities of the conversion e^-, a_0 is the scaling factor, σ_n are the detector-resolved line widths at 1 MeV, with $\sigma_n = a_5\sqrt{\frac{E_n}{1MeV}}$. The effective term $c(x)$ can be expressed as,

$$c(x) = \frac{a_6 C(x)}{e^{2(x-E_c)/\sigma_3} + 2}. \tag{3.3}$$

The Compton distribution $C(x)$ is obtained from reference [Sie65] and the Compton edge $E_c = 0.9 \cdot a_3$. The exponential term in the denominator confines Compton effect to energies below E_c.

Like the Compton term, the linear background is cut off by the denominator when the energy exceeds E_3. Then $b(x)$ can be expressed as

$$b(x) = \frac{a_7 + a_8 x}{e^{2(x-a_3)/\sigma_3+1}}. \tag{3.4}$$

The energy distributions of the eight scintillators were fitted with the same functional as given by equation 3.1. Knowing the exact energies for the four e^- lines and their measured pulse positions (a_1, a_2, a_3, and a_4) obtained from the fitting, the relationship between the energy and the channel number could be determined. However, this energy was again corrected for the straggling effect (see equation 2.22).

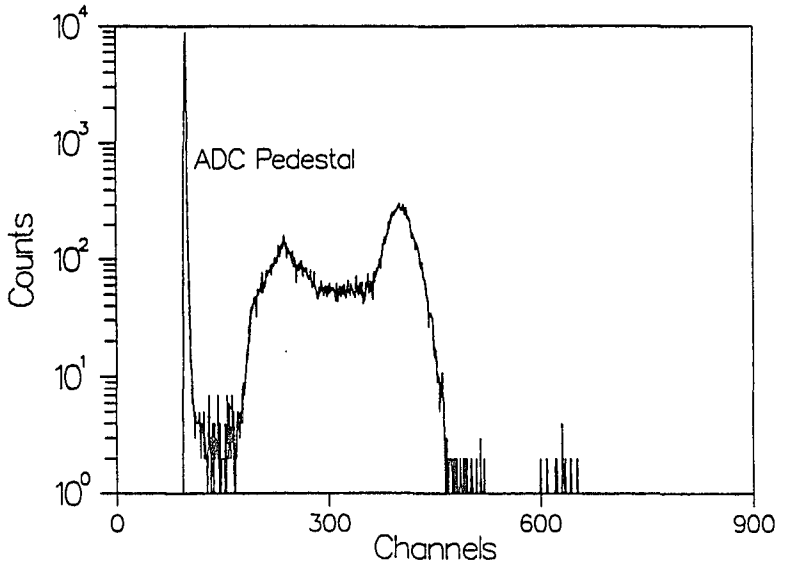

Figure 3.5: ADC pedestals in the ADC readout.

3.2.2 Calibration of Position Measurement

The Anode Calibration

Calibration of the wire chamber anode readout included the alignment of the dual measurements of the resistive pulses with the 2-V and 8-V range ADC's, and the pedestal correction for the pulse height. There were sharp peaks in the low channels of all the ADCs, due to the pedestals existed in the measurements (Figure 3.5). The pedestal centroid p was measured for every calibration run and subtracted from each ADC channel, resulting in a net pulse height H

$$H = h - p, \tag{3.5}$$

where h is the raw ADC readout of the pulse height.

This correction was done before setting the relationship between the two ADC's. The relationship between the 2-V and the 8-V ADC's was obtained from the collected data. Since the experiment recorded the data event-by-event, each event triggering the wire chambers resulted in a 2-V ADC readout and an 8-V ADC readout. Thus,

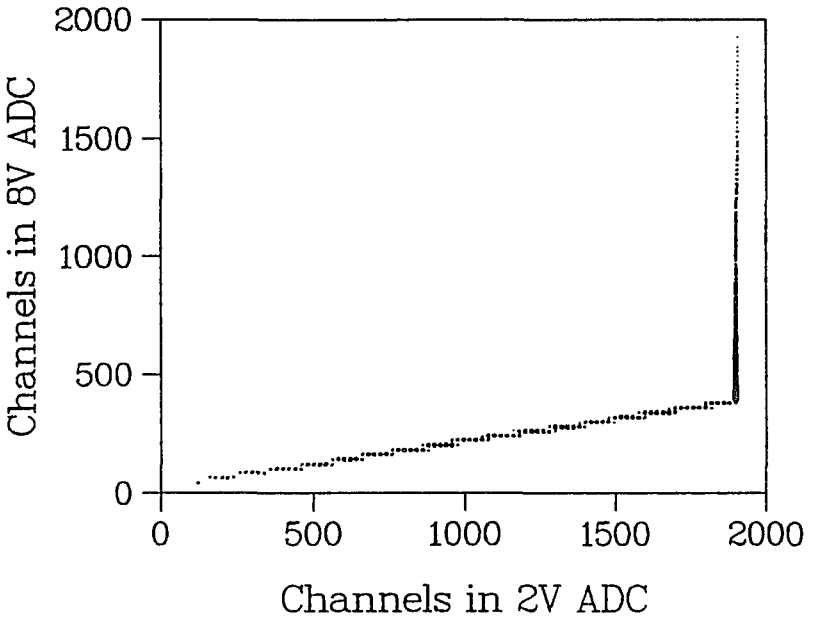

Figure 3.6: Relationship between the 2-V and the 8-V ADC's, with the necessary pedestal subtraction.

each single event provided the required information. With enough such events, a well-established relationship between the two ADC's could be obtained. This is shown in Figure 3.6 after the pedestal had been subtracted.

The 2-V ADC had good resolution for pulse heights from 0 to 2 volts but an overflow was generated when the pulse height was above the 2 volt limit. The 8-V ADC provided a relatively poorer resolution; however, it covered the entire dynamic range. The scheme here was to take the optimal choice: for large pulses, the 8-V ADC was the only choice, and for small pulses, the 2-V ADC was chosen. Thus, the 2-V ADC value had to be scaled to the 8-V ADC range. This was done precisely by linearly fitting the data, shown in Figure 3.6, from channel 0 to channel 1800. The final pulse height used for anode position measurement was

$$H_c = \begin{cases} a \cdot (h_{2V} - p_{2V}) + b, & h_{2V} < 2 \text{ V}; \\ h_{8V} - p_{8V}, & h_{2V} \geq 2\text{V}. \end{cases} \tag{3.6}$$

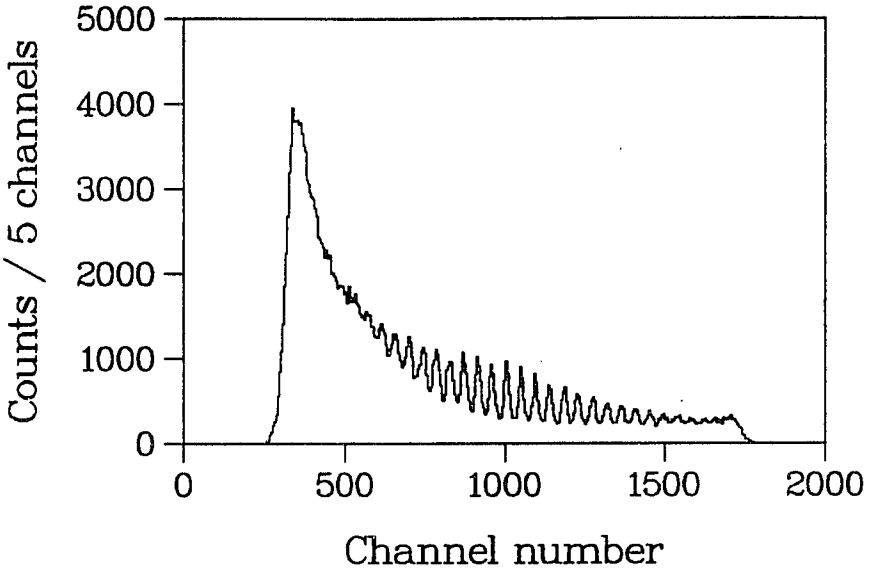

Figure 3.7: θ distribution of Mott scattering events without pedestal correction.

where H_C is the final version of pulse height used in the experiment, and h and p are the raw pulse height of the signal and the pedestal from the ADC, respectively. Parameters a and b are the slope and the intercept of the linear fit. This calibration was carried out for both ends of the anode wire. Substituting H_c for h in Equation 2.19, the anode position measurement had an improved resolution. Figures 3.7 and 3.8 show the θ distributions of Mott events with an Al target at the energy of 1525 keV with and without pedestal subtraction; 37 anode wires are clearly visible in Figure 3.8 after the correction. The first and the last anode wires were not the designed for position measurement; instead, they were thick wires for terminating the field at the ends, and thus, were not expected to produce avalanches.

The final calibration of the wire number and its measured channel number was achieved by using ^{55}Fe (see Figure 3.9). The 6-keV x-ray from ^{55}Fe has the advantage of producing rather localized ionization in the wire chambers. With the identification of wire number and the dimensions of the MWPC's, the parameter a in Equation 2.23 is determined as: a =A+$(N-1)\Delta a$, where A is the distance from the first anode wire to the beam axis, N is the anode wire number for a specific event, and Δa is the

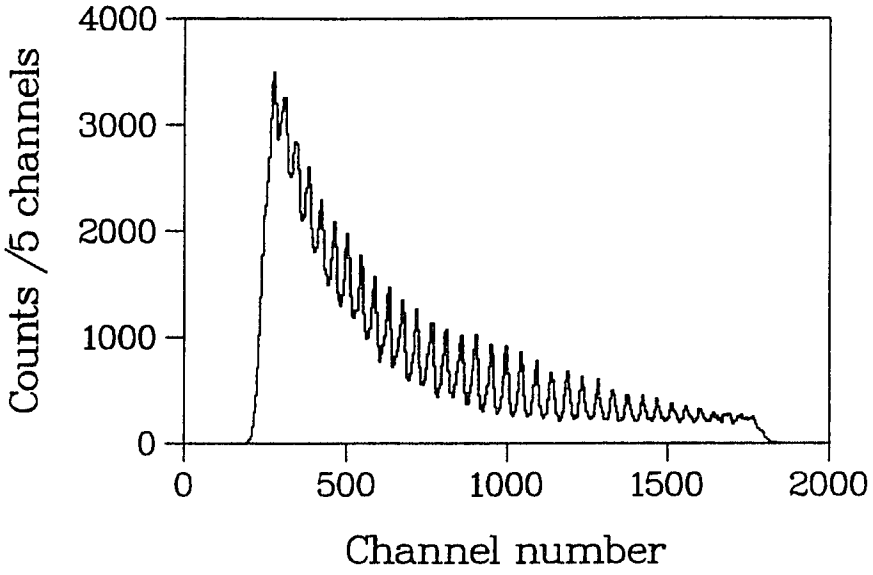

Figure 3.8: The same data as Figure 3.7, but with pedestal correction.

known anode wire separation.

The pedestal subtraction improved the wire chamber resolution significantly; however, the long-term ADC gain drift was difficult to correct. Fortunately, it was small enough to be ignored. The maximum deviation was found to be less than 0.3° in the θ angle during eight months of data collection. A resolution of $\sim 0.9°$ in θ angle with the anode resistive readout was achieved.

The Cathode Calibration

The calibration of the cathode wire was again performed with a radioactive ^{55}Fe source for a smaller ionization spot. As mentioned in chapter 2, the cathode wires had a finer spacing than the anode wires. Even with the ^{55}Fe source, we were still unable to resolve all the cathode wires. The wires near the edges could not be seen clearly. Figure 3.10 shows the ϕ angle distribution of events from the calibration source.

The trigger was modified in the calibration to obtain the data in figure 3.10. Since the 6 keV x-rays are of too low an energy to fire the related scintillators, the TDC start

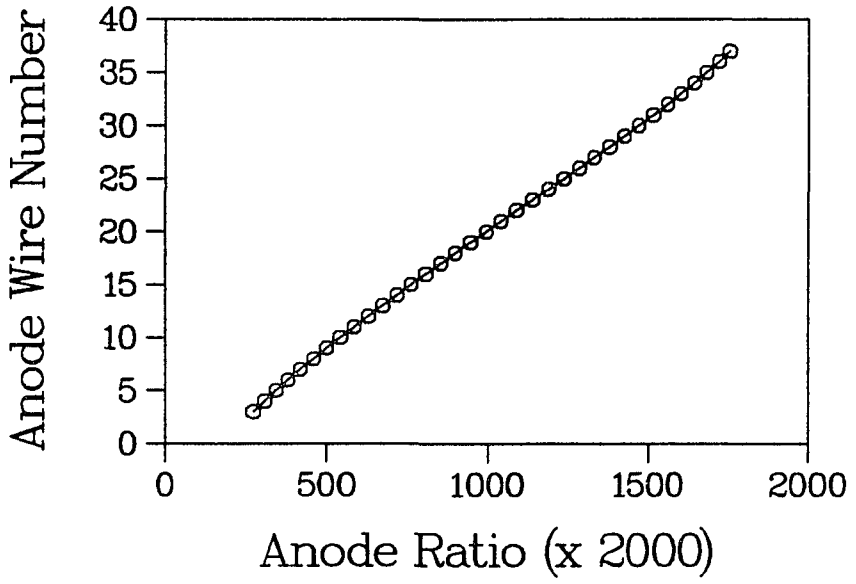

Figure 3.9: Relationship between the measured channel for the anode wire and the anode wire number. The line was fitted with a third-order polynomial.

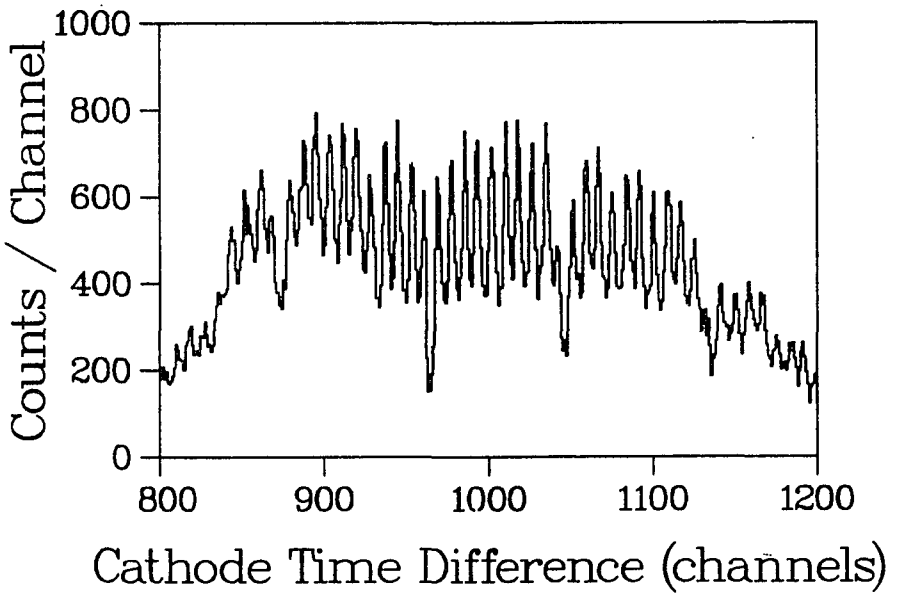

Figure 3.10: ϕ angle distribution of wire chamber 0 obtained using a ^{55}Fe source.

pulses were generated by the front cathode windows. The poor rise time of the front cathode window signal did not affect the difference of delay times. Because of the invisibility of the wires near the edges, only the clearly observed wires in the middle of the cathode were involved in the calibration. A linear fitting scheme was used to avoid introducing a large deviation to the edge wires. The absolute positions of the wires were extracted by relating their measured positions to the vacuum support wire, which appeared as a large dip in figure 3.10. The exact positions of these stainless-steel wires were known in the design. The ϕ angle resolution via the cathode delay-line readout was 0.5°.

3.3 Event Selection and Data Reduction

3.3.1 General Requirements for a Valid Event

Each time the scintillator fires, it generates an event trigger, and the data acquisition system records it as either a *singles event* or a *coincidence event*, depending on the trigger type. The scintillators fire on both γ rays and charged particles. Even with charged particle triggering, only in about 90% of the cases is it accompanied by the firing of the appropriate wire chamber, due to the Landau distribution of the MWPC's. A valid event requires all the information necessary for the kinematic reconstruction. The general requirements are: (a) the input register records the firing of the front cathode window of the related wire chamber, (b) the anode resistive readout results in a valid ADC value; i.e., both pulses from either end of the anode pass the ADC thresholds and produce no overflow in the 8-V ADC, (c) there are valid TDC stops for the cathode, but no TDC overflow is detected.

The ADC hardware thresholds may drift during a long-term run, which may

introduce inconsistency in the event selection and finally result in a false change in the event rate. To avoid this problem, in the software, a slightly higher ADC threshold is set. Each event has to pass this software threshold in order to be selected. Hence, a small drift in the hardware threshold does not affect the data.

The energy T, polar angle θ, and azimuthal angle ϕ of the scattered charged particle can be calculated if requirements (a), (b) and (c) are met. With T, θ and ϕ, further kinematic cuts for the Mott scattering and for the Bhabha scattering events can then be applied.

3.3.2 Good Singles Events

The data acquisition system records a singles event when only one of the eight-fold scintillators has fired. Besides that, a good singles event has to meet the general requirements described above. Only about 60% of the singles triggers are selected after the general requirements. The events that are too close to the edges of the MWPC's are also discarded, because the MWPC's tend to lose the accuracy at the edges in the angular reconstruction. At a particular beam energy, an energy window corresponding to the energy loss in the target and the energy resolution of the scintillators could be required. But this introduces the problem of moving the cuts with the beam energy. These cuts become very sensitive to the energy measurement and are not used in the final data selection. Instead, a fixed energy window for all the runs is chosen. Thus consistent cuts are applied to all the data. In addition to the general requirements, a good singles event has to pass the kinematic cuts for both energy and angular requirements listed below:

- The singles energy fits in the window 500 keV $\leq T_{e+} \leq$ 2990 keV

- The scattering angle θ in the laboratory system falls within $22° \leq \theta \leq 40°$
- The angle ϕ: (a) $20° + 90° \cdot N \leq \phi \leq 42.5° + 90° \cdot N$, or (b) $47.5° + 90° \cdot N \leq \phi \leq 70° + 90° \cdot N$, where $N = 0, 1, 2, 3$.

Three histograms of good singles events are of the most interest, as shown in Figure 3.11. The data in the figure were taken at a beam energy of 1432.2 keV. The energy peak of Mott scattering events (Figure 3.11(a)) is located at a position equal to the beam energy minus the $\sim$ 3 keV energy loss in the target. The shape of the spectrum is well understood. The long tail at low energy is produced mainly by those events from the positrons out-scattered by the target chamber wall. Two shoulders on either side of the energy peak are visible. As was mentioned in chapter 2, the shoulder on the low energy side is due to Bhabha events, in which only one of the scattered particles is detected by the detector system. The shoulder on the high energy side is the typical detector response to the positrons. The detected positrons quickly lose their kinetic energy and stop in the detector. These slow-moving positrons annihilate with electrons in the scintillator and produce two 511 keV γ-rays from each annihilation. These γ-rays contribute extra energy which is added to the measured kinetic energy of the positrons. The θ angle distribution has the typical normal Mott scattering polar angle dependence and the spectrum in ϕ angle is isotropic if the beam is well aligned. The gaps in the ϕ angle are due to the software cuts, where the joints of the scintillators are glued.

3.3.3 Good Coincidence Events

In addition to the coincidence trigger and the general requirements, a good coincidence event is selected after it passes the software cuts for the two-body decay kinematics. In

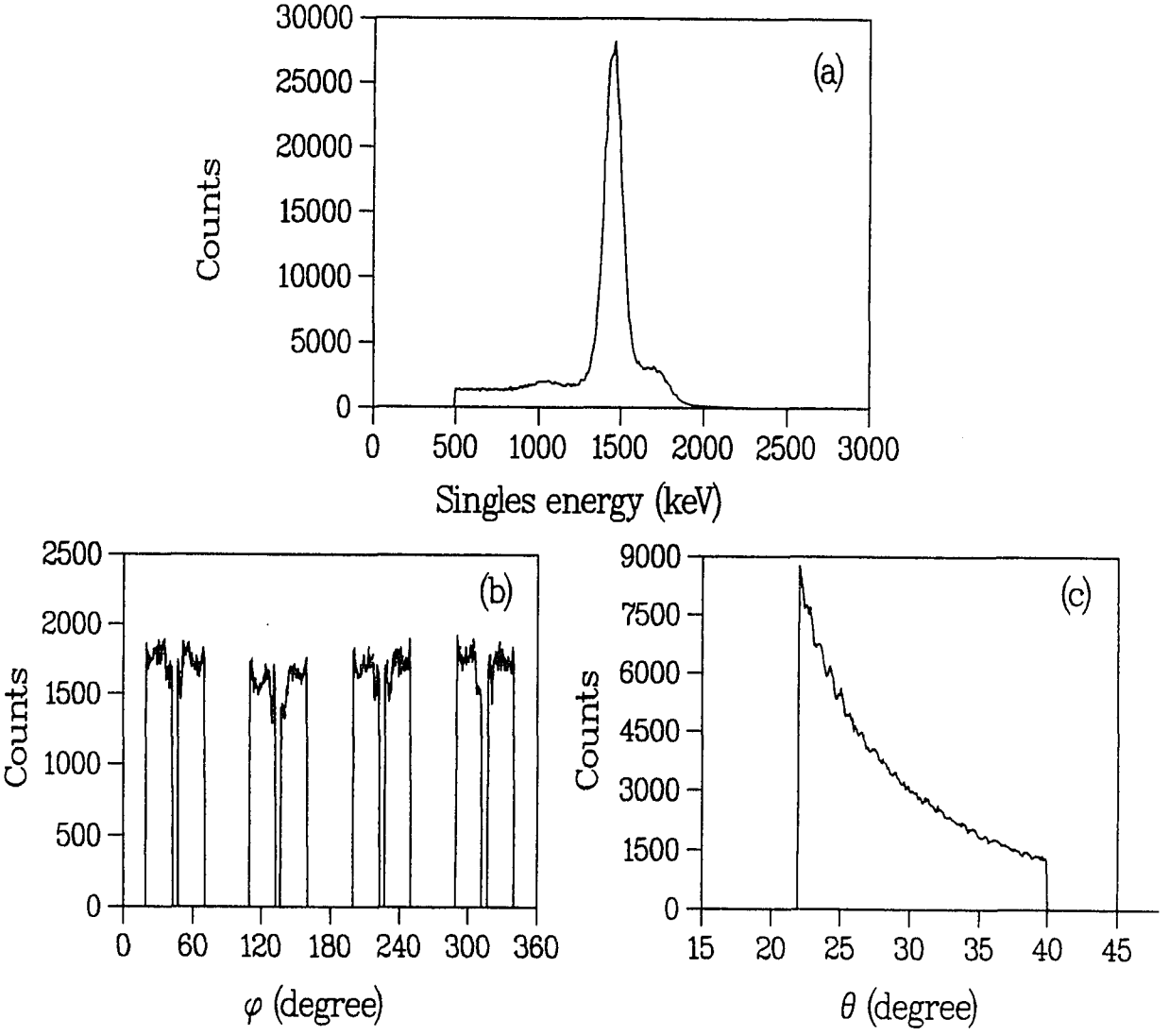

Figure 3.11: The histogrammed events after the cuts for a good singles event. The data were taken at a beam energy of 1432.2 KeV. (a) Energy distribution (b) Angular distribution in ϕ (c) Angular distribution in θ.

the hardware, two firings of scintillators in the 45 ns time window from both adjacent quadrants and opposite quadrants were taken as a coincidence trigger. Two-body decay or scattering requires coplanarity in the ϕ angle; i.e., the difference $(|\phi_{e+} - \phi_{e-}|)$ in ϕ angle must be about 180°. By simply requiring the firings to be in opposite quadrants, the coplanarity is obeyed. No exotic events having very large $(|\phi_{e+} - \phi_{e-}|)$ deviation from 180° are observed. The actual cuts are listed here:

- The sum energy is wide open, $0 < T_{e+} + T_{e-} < 2990$
- The coplanarity of ϕ, requires firings in opposite quadrants. The wire chamber edges are cut, by applying, $22.5° \leq \phi - 90° \cdot N \leq 67.5°$ for both particles, where $N = 0, 1, 2, 3$
- In the CM system, the scattering angle is selected within the range $60° \leq \theta_{e+} \leq 120°$ and $60° \leq \theta_{e-} \leq 120°$.

The active detector volume used in selecting a good coincidence event is different from that for a good singles event. The θ angle cuts are placed in the CM system and thus they move in the physical detector region as the beam energy changes. However, the θ cuts for the singles events are fixed. In order to obtain the correct position measurements from the MWPC's, the exact target position and precise beam energy are necessary for calculating the θ angle in the CM system. Deviations in these parameters will contribute systematic errors. The shift in target position can be monitored from the histogram of $|\theta_{e+} - \theta_{e-}|$, which should be 0° in the CM system. It should be mentioned that due to the inability of the detector system to distinguish positrons from electrons, the definition of the θ angle is different from the common definition, and it will be discussed later. The target position and energy dependence will also be discussed later in this chapter.

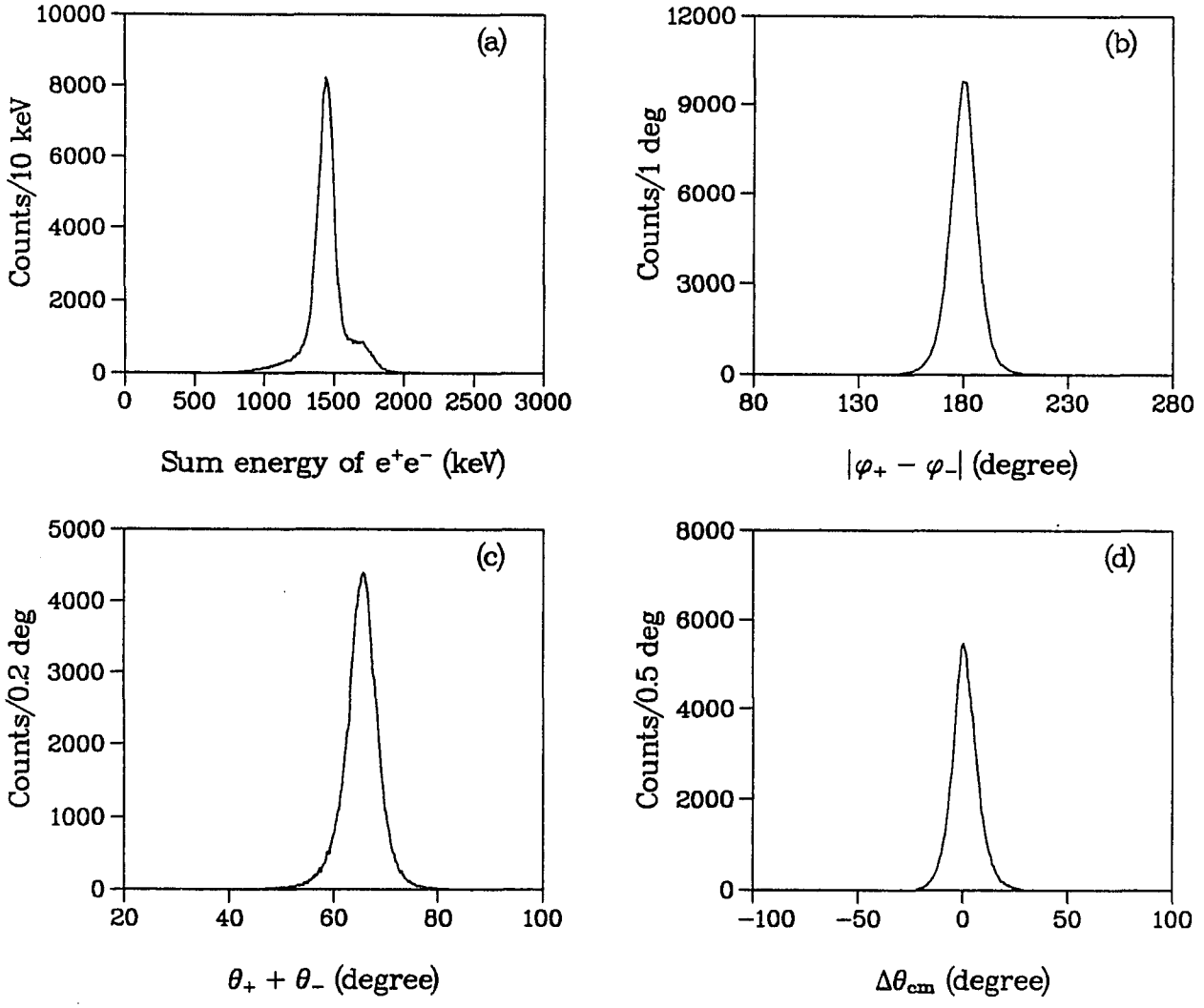

Figure 3.12: Histograms for e^+e^- scattering events at a beam energy of 1432.2 keV. (a) the sum energy of both particles (b) the ϕ angle difference (c) the opening angle (d) the folded θ angle difference in the CM system.

The detector system covers a very large volume in the CM system; even after the cuts, nearly 1/4 of the entire solid angle is still active. Four different histograms of good coincidence events for a run at a beam energy of 1432.2 keV are shown in figure 3.12. The sum energy of the coincidence events $T_{e+} + T_{e-}$ is centered at the beam energy. A shoulder on the high energy side due to 511 keV annihilation pile-up is seen in the spectrum (Figure 3.12(a)). The ϕ angle difference has its peak at 180°. The width of the coplanarity spectrum (Figure 3.12(b)) is $\sim 7°$ (FWHM) and indicates no strong multi-scattering effects in the target. This is consistent with the case for an extremely thin target (of thickness 55 μm). The opening angle is defined as the sum of the polar angles for the two detected particles in the laboratory system (Figure 3.12(c)). The peak is centered at $\sim 67°$, dependent on the incident energy of the positrons. The opening angle is wide simply due to the e^+e^-scattering kinematics and varies with incident beam energy.

The fourth histogram (Figure 3.12(d)) requires some explanation. The MWPC's identify the track of the charged particle, but no information is given by them for the specific charge of the detected particle, negative or positive. In the experiment, the measured θ angle in the lab system was transferred to the the CM system via the formula,

$$\cos\theta_{CM} = \pm\left(1 - \frac{4m}{\frac{T_+ + 2m}{\cos\theta_\mp} - T_+}\right), \tag{3.7}$$

where T_+ is the beam energy. $\theta_\mp$ are the polar angles in the lab system for e^- and e^+ respectively. Since we cannot distinguish electrons and positrons, only $|\cos\theta_{CM}|$ is calculated. For a two-body decay or scattering, the two particles are moving back-to-back in the CM system. The parameter $\Delta\theta_{CM}$, which is defined as

$$\Delta\theta_{CM} = \theta^{l}_{CM} - \theta^{s}_{CM}, \tag{3.8}$$

should be zero, where θ^{l}_{CM} and θ^{s}_{CM} are the θ angles in the CM system, corresponding respectively to the larger and smaller θ angle of the two scattered particles in the lab system. As shown in the figure, the histogram is centered at 0°. Deviation of the target from its designated position will be carried in the transformation and will result in a shift from 0° in the histogram. This feature is used to monitor the target position. Corrections can be performed according to the amount of shift from 0°. In the next section, this correction will be discussed in detail.

During the data collection, several large scintillation counters were placed above the target chamber to veto possible background from cosmic rays. The data for the coincidence events exhibit an environment free of background.

3.4 Obtaining the Excitation Function

3.4.1 Normalization

At $g-2$ limits (lifetime $\tau \sim 10^{-13}s$), the expected resonance contributed by X^0 is $\sim$ 1% of the non-resonant QED Bhabha scattering cross section. Normalizing the Bhabha events to the incident positrons is difficult, since in the experiment, it is not possible to monitor the number of incident positrons without losing the established good beam quality. The intensity of the positron beam drifts with time. Fluctuation of a few percent in the beam intensity is expected. Therefore, using the beam time as the normalization also introduces unacceptable errors to the data. Reliable normalization is obtained from the number of Mott events (good singles events), which is directly proportional to the number of incident positrons. Assuming

100% efficiency for the scintillators, the Mott scattering events can be expressed as

$$N_M(M_{X^0}) = N_P \left(\sum_{n=0}^{n=3} \epsilon_n \right) /4 \cdot \int_{V_M} \frac{d\sigma_M}{d\Omega} d\Omega, \tag{3.9}$$

where N_M is the number of good Mott events, N_P is the total number of incident positrons, V_M is the active detector volume for Mott scattering events in the lab system, $\frac{d\sigma_M}{d\Omega}$ is the differential cross section of Mott scattering, and ϵ_n for $0 \leq n \leq 3$, are the efficiencies of the MWPC's. Symmetrical cuts were taken for the four MWPC's, thus the dependence on the wire chamber efficiency can be simply expressed by the term $(\sum_{n=0}^{n=3} \epsilon_n)/4$.

The normalization factor is proportional to the beam intensity, and so the normalized Bhabha scattering cross section is independent of beam intensity fluctuations. The data were collected with high statistics, $\sim 1.8 \times 10^5$ and $\sim 5.0 \times 10^5$ events (before scaledown correction) acquired for the Bhabha and Mott scattering after the necessary kinematic cuts, respectively. Considering statistical errors only, the accuracy for the normalization is $\sim 0.1\%$, which is reasonable for the sensitivity required by the experiment.

3.4.2 The Excitation Function

The Bhabha scattering events can be expressed in a similar way to equation 3.9,

$$N_B(M_{X^0}) = N_P \left(\epsilon_0\epsilon_2 + \epsilon_1\epsilon_3 \right) /2 \cdot \int_{V_B} \frac{d\sigma_B}{d\Omega} d\Omega, \tag{3.10}$$

where N_B is the number of Bhabha scattering events, V_B is the active detector volume in the CM system for Bhabha scattering, and $\frac{d\sigma_B}{d\Omega}$ is the CM differential Bhabha scattering cross section. The coincidence events are chosen for the opposite wire chambers, so the resultant efficiency is $(\epsilon_0\epsilon_2 + \epsilon_1\epsilon_3)/2$.

By normalizing Bhabha events to Mott events, the excitation function $f(M_{X^0})$ is then defined as,

$$\begin{aligned} f(M_{X^0}) &= \frac{N_B(M_{X^0})}{N_M(M_{X^0})} \\ &= \frac{N_P(\epsilon_0\epsilon_2+\epsilon_1\epsilon_3)/2\cdot\int_{V_B}\frac{d\sigma_B}{d\Omega}d\Omega}{N_P\left(\sum_{n=0}^{n=3}\epsilon_n\right)/4\cdot\int_{V_M}\frac{d\sigma_M}{d\Omega}d\Omega} \\ &= \frac{(\epsilon_0\epsilon_2+\epsilon_1\epsilon_3)/2\int_{V_B}\frac{d\sigma_B}{d\Omega}d\Omega}{\left(\sum_{n=0}^{n=3}\epsilon_n\right)/4\int_{V_M}\frac{d\sigma_M}{d\Omega}d\Omega}. \end{aligned} \tag{3.11}$$

Equation 3.11 shows the wire chamber efficiency dependence of the excitation function. These efficiencies were constantly monitored through the Landau distribution of the MWPC's. In the real data, no significant drifts of the efficiency were observed during the entire data collection period. Generally speaking, the sensitivity of the experiment is affected only by sudden wire chamber drift, because the expected resonances appear as peak-like structures in the excitation function. Continuous and slow changes in the wire chamber efficiency basically contribute to the base line of the excitation function. A detailed discussion of the MWPC's efficiency is presented in section 3.6.3.

The excitation function was obtained for the entire X^0 mass region (1560 keV $< M_{X^0} <$ 1860 keV) suggested by the GSI heavy-ion data. Figure 3.13 shows the excitation function $f(M_{X^0})$ after kinematic cuts required for the two-body decay of a light neutral object were applied. The data in figure 3.13 are divided into four plots (figure 3.14) for a detailed view of the excitation function.

Within the sensitivity of the experiment, the excitation function shows no deviation from the smooth Bhabha scattering background. No peak structures contributed by the on-mass-shell creation of the X^0 are observed. The uncertainty in the excitation function is dominated by statistical errors ($\sim$ 0.26%). Both Bhabha and Mott scattering cross sections in the detector volume of the experiment define the slow

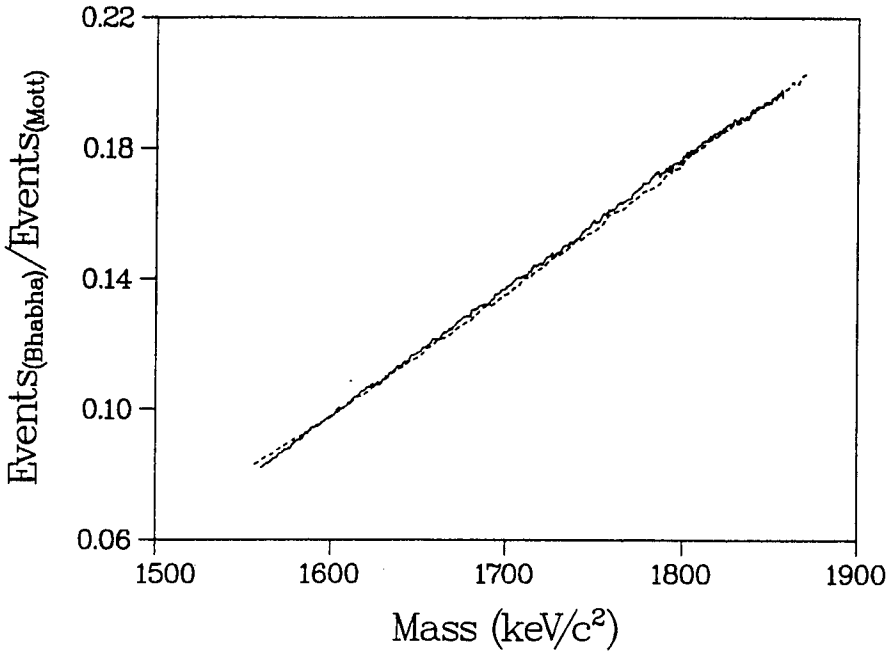

Figure 3.13: The excitation function, defined as the ratio of the number of Bhabha scattering events to the number of Mott scattering events, obtained in the invariant mass region 1560 keV $< M_{X^0} <$ 1860 keV. (a) solid dots represent the experimental data (b) the dashed line presents the Monte Carlo simulation.

rising slope of the excitation function as the energy increases. Monte Carlo simulations [Phl93], including positrons scattered by the target chamber, also show good agreement with the shape of the excitation function (see figure 3.13). The excitation function is investigated in detail and the constraints on the lifetimes of the hypothetical object are extracted from the excitation function data. The detailed method of calculating the lifetime limits is discussed next.

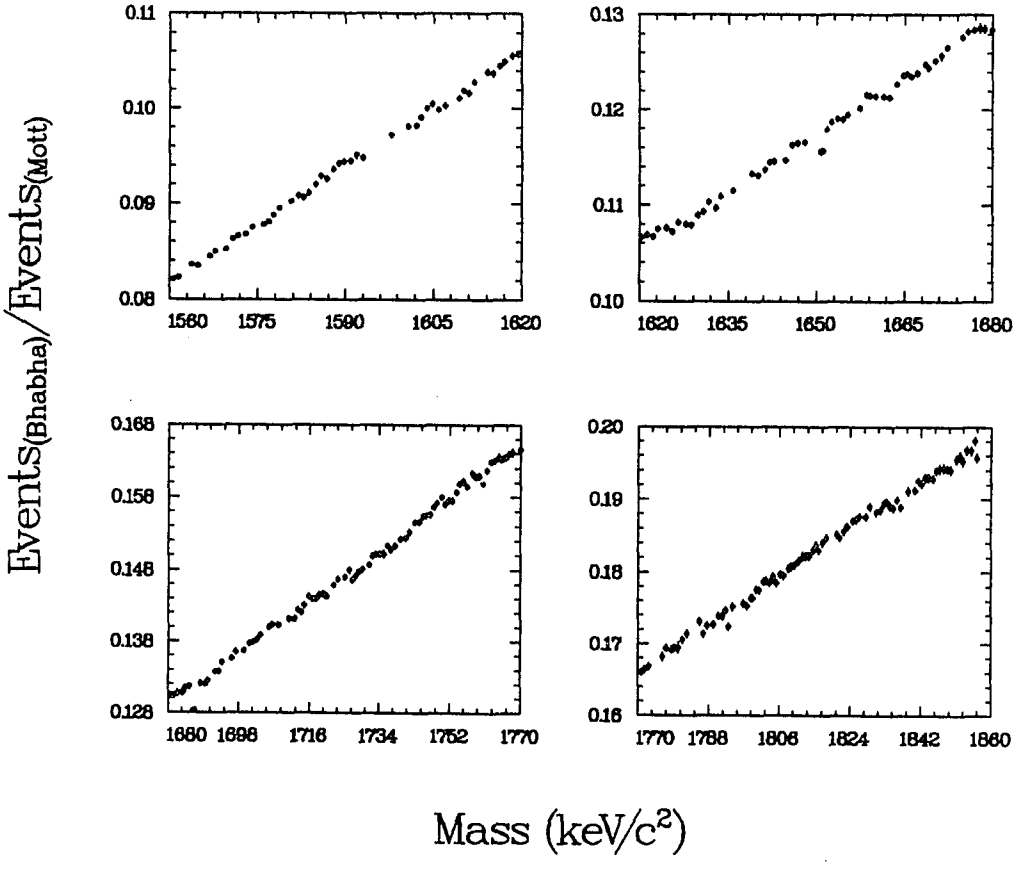

Figure 3.14: Detailed view of the excitation function. The data are the same as those plotted in figure 3.13.

3.5 Searching for Resonances in the Elastic Bhabha Scattering

3.5.1 Overview

The existence of the new light neutral particle X^0 introduces new vertices (figure 2.2) into the QED e^+e^- scattering Feynman diagram (figure 2.1). Resonances due to the s-channel diagram are expected to occur at the on-mass energy of the X^0. Although the sharp resonance spectrum near that specific energy is significantly broadened by the momentum distribution of the electrons in the metallic target, for such an object with a lifetime of $\sim 10^{-13}$ sec, the resonance peak cross section is expected to be $\sim 1\%$ of the ordinary QED e^+e^- scattering cross section. For longer lifetimes, the resonance peak is even smaller. Deviations with magnitudes larger than a few error bars above the Bhabha background are potential clues to resonances. Mathematical methods are developed to search for deviations in the normalized Bhabha cross section. At each energy, the deviations are fitted with the resonance shape including momentum broadening from the target electrons. Upper limits are thus established for the energy-integrated resonant cross sections, and these are related to the lifetime of the neutral object. In this section, a study of data for the e^+e^- scattering cross section is presented, and final limits on the lifetimes for the object are extracted from the experimental data.

3.5.2 Non-resonant Bhabha Scattering Background

The non-resonant Bhabha scattering cross section is ~ 200 mb in the energy range covered by this experiment. This non-resonant cross section varies smoothly with

energy. The absolute value of the QED Bhabha cross section is not the main concern of the experiment; instead, localized structures are the real signals of the resonance. These structures are resolved by subtracting the background from the excitation function and are identified through the residuals obtained.

Assuming b_{X^0} denotes the background, the residual $R(M_{X^0})$, which is by definition the ratio of the resonant cross section to the non-resonant cross section, can be expressed as

$$\begin{aligned} R(M_{X^0}) &= \frac{f(M_{X^0})-b(M_{X^0})}{f(M_{X^0})} \\ &\simeq \frac{\int_{V_B}(\frac{d\sigma_R}{d\Omega})d\Omega}{\int_{V_B}(\frac{d\sigma_B}{d\Omega})d\Omega}, \end{aligned} \tag{3.12}$$

where $\int_{V_B}(\frac{d\sigma_R}{d\Omega})d\Omega$ is the resonant cross section folded by the detector volume, and $\int_{V_B}(\frac{d\sigma_B}{d\Omega})d\Omega$ is the non-resonant QED Bhabha scattering cross section .

The background $b(M_{X^0})$ is obtained by fitting the excitation function $f(M_{X^0})$ with a third order polynomial. For better accuracy, the excitation function is not fitted in the entire invariant mass region, but instead the invariant mass region is divided into 4 regions, each of which covers $\sim$ 80 keV. This mass window for the fitting is about 10 times wider than the expected resonance width, resulting in good fittings with chi squares close to 1.0.

3.5.3 Resonant Bhabha Scattering

Assigning the deviations from Bhabha background to the contribution of the X^0, upper limits on the resonant cross section can then be calculated from the data obtained in equation 3.12. Figures 3.15 and 3.16 show the residuals as a function of the invariant mass. The resultant statistical error is about 0.26%. The points are distributed around zero base line. Clearly, there is no evidence of resonance-like peaks

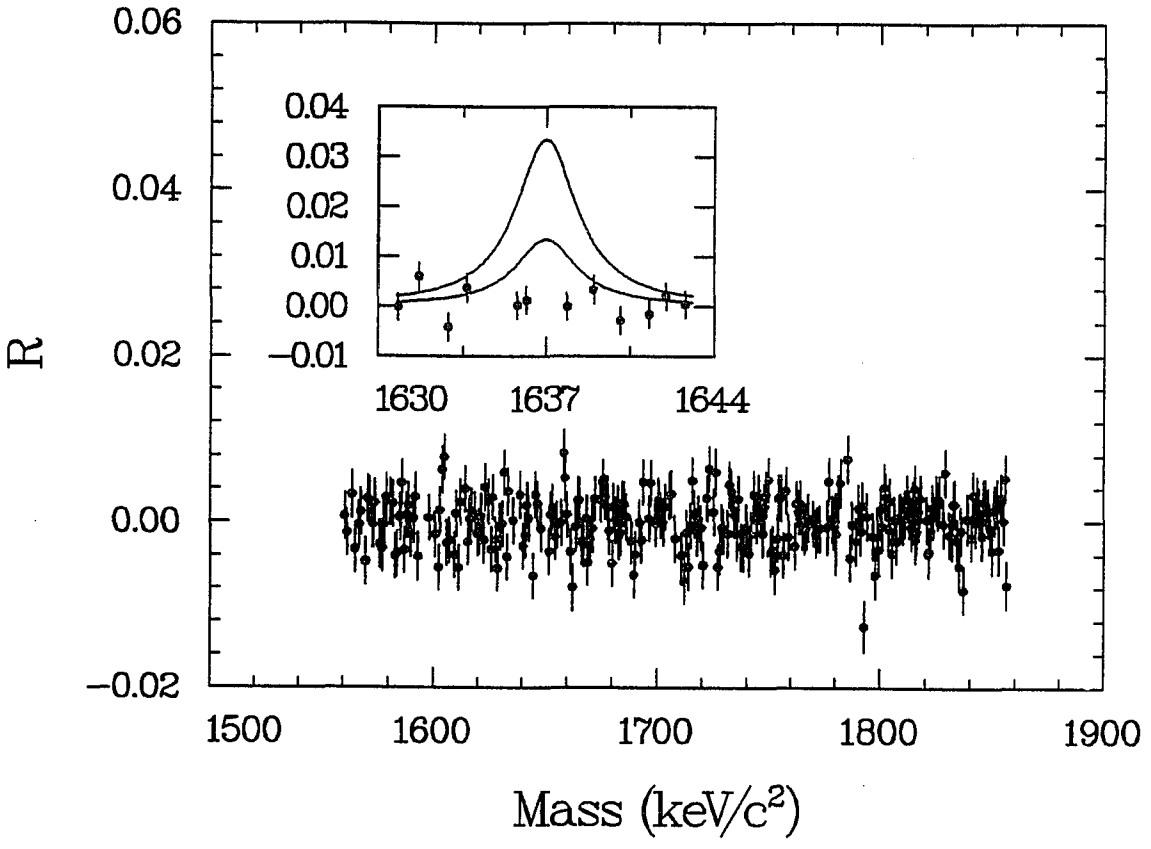

Figure 3.15: Ratio of the resonant cross section to the QED Bhabha cross section as a function of the invariant mass M_{X^0}. The inset expands the residuals at the energy corresponding to GSI 616 keV sum-energy line, and shows two simulated resonant peaks with lifetimes of 2.0×10^{-14} and 5.0×10^{-14} sec for the higher and lower curves, respectively.

having widths ~7 keV.

To study the overall systematic errors, the residuals are histogrammed, and the distribution is shown in figure 3.17. This histogram is fitted with a Gaussian function having a centroid at zero. The fitted σ for the Gaussian function is 0.27%, indicating the value of the total error bar for the measurement. This total error bar (0.27%) is dominated by statistical errors (0.26%). No significant systematic error is observed.

3.5.4 Lifetime Limits

Extraction of the Resonant Cross Section

The final resonance shape is dominated by the Compton profile of the electron momentum distribution in the target. Compared with other factors, the broadening due to the target electrons is the most significant. In order to extract the upper limit of the energy-integrated cross section, the correct shape of the resonance must be determined. Applying the detailed calculation given in reference [Hen88], section 2.63, the resonant cross section dependence on the energy is

$$\sigma(E_{CM}) = a \cdot \frac{J(q)}{p_+}. \tag{3.13}$$

In equation 3.13, the parameter E_{CM} is the total energy of the e^+e^- in the CM system, a is a term representing the peak resonant cross section in units of Bhabha scattering cross section folded with the detector acceptance, p_+ is the momentum of the positron in the lab system, and $J(q)$ is the Compton profile defined as,

$$J(q) = 2\pi Z \int_{|q|}^{\infty} n(p) p dp, \tag{3.14}$$

where $n(p)$ is the momentum distribution of the target electrons, and q is defined as,

$$q = \frac{1}{2}\left((2-(M_{X^0}/m)^2)p_+ + (E_{CM}^2/2m - m)\left((2-(M_{X^0}/m)^2)^2 - 4\right)^{1/2}\right). \tag{3.15}$$

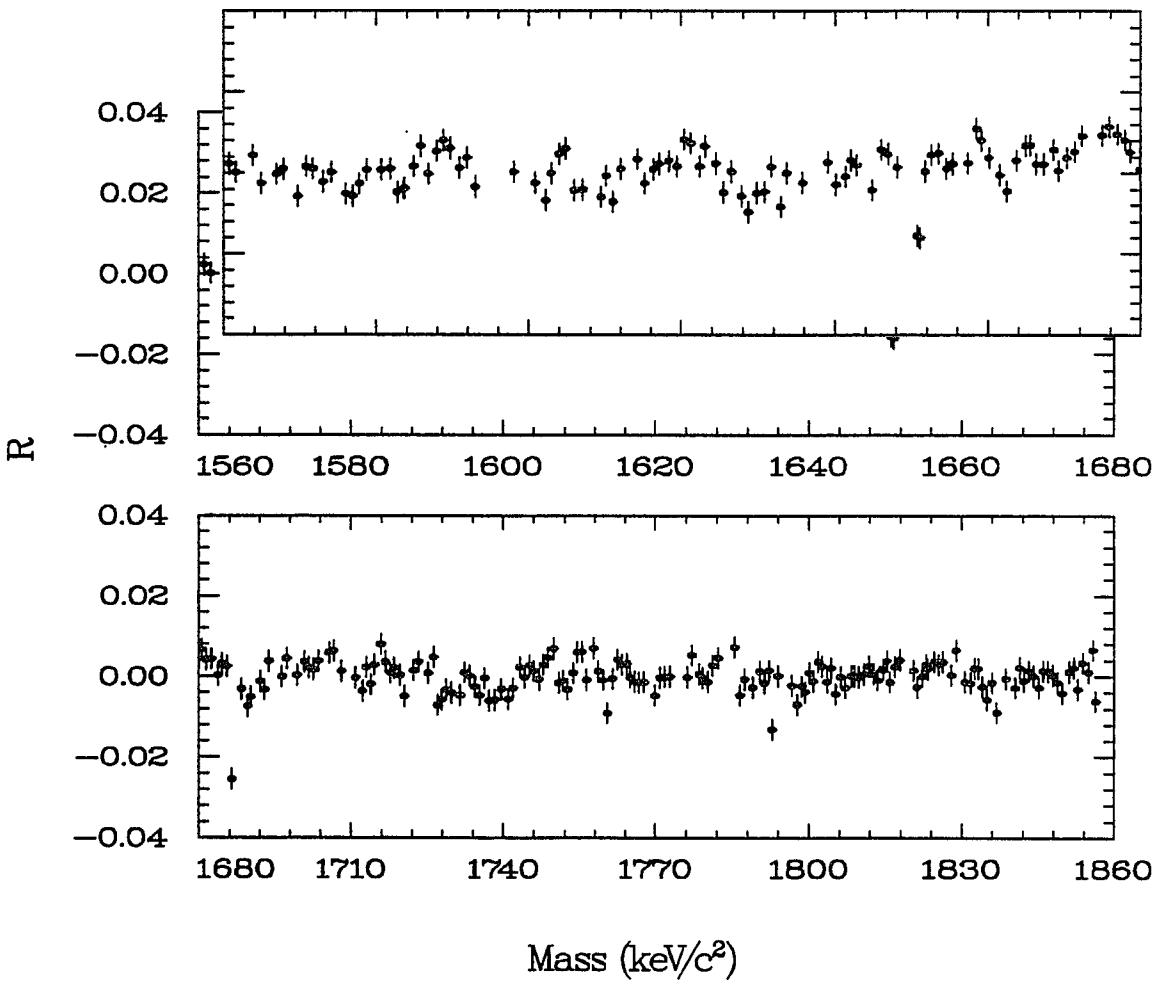

Figure 3.16: A detailed view of the residuals, the same data as in figure 3.15.

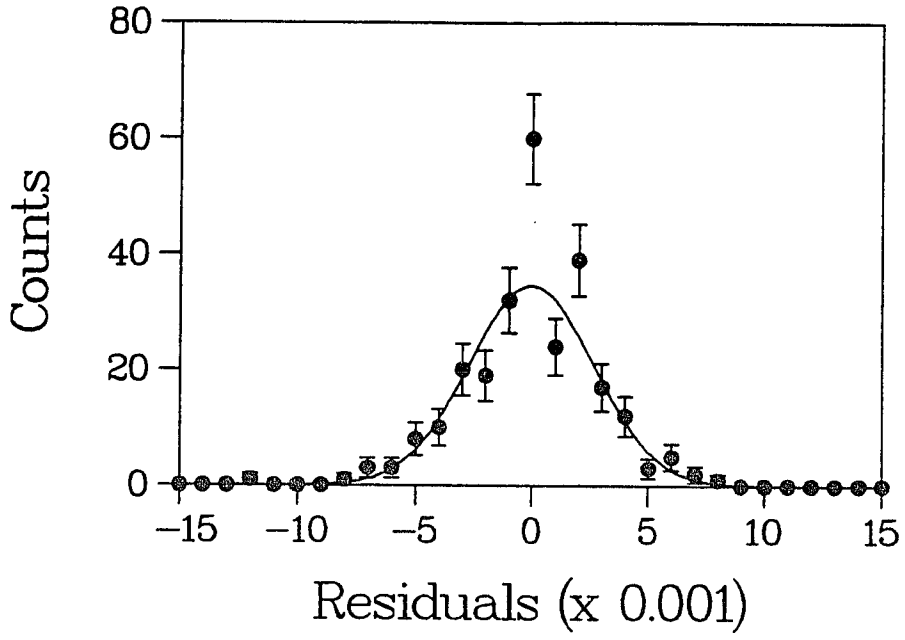

Figure 3.17: Histogrammed distribution of the residuals.

The Compton profile of metallic lithium has been studied by many groups [Eis72, Tan73, Lun71, Suz81, Dov83]. The most recent result on this issue is given by Dovesi et al. with a Hartree-Fock calculation. Both the valance and 1*s* electrons were included in their calculation. The Hartree-Fock 1*s* electron was considered beyond 3.0 atomic units (a.u.). The Compton profile for metallic lithium is shown in figure 3.18.

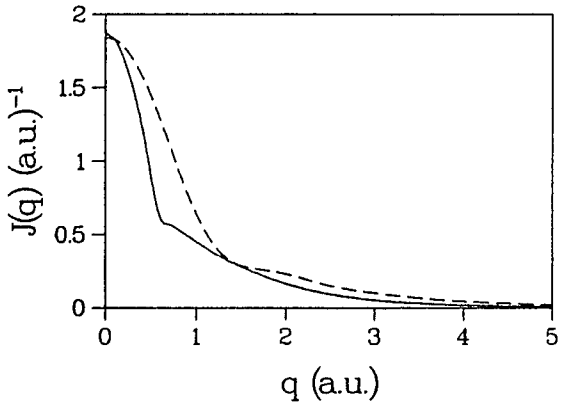

Figure 3.18: Theoretical calculated Compton profile of metallic Li by Dovesi et al.

Neglecting the small change of the QED Bhabha cross section in the narrow window of resonance width ($\sim$ 7 keV in the CM system), at a specific mass M_{X^0}, within such a resonance width, the residual spectrum (figure 3.15) represents the energy-integrated resonant cross section folded with the detector acceptance. The spectrum of residuals was fitted with the real resonance shape. By fixing the resonance mass M_{X^0} for each data point in the spectrum during the fitting, the resonance peak a (equation 3.13) and its related error bar σ_a were obtained for each point. The values of peak resonant cross sections extracted from the fitting had positive to negative values, as the original data spectrum (figure 3.15) already indicated. The negative values of peak cross sections have no physical meaning. These extracted negative peak cross sections were expected to occur in the experiment. The reason is obvious: since the data in the spectrum 3.15 are the experimentally measured deviations of the Bhabha scattering section within the sensitivity of the experiment, it is bound to have negative values due to statistical fluctuations and systematic errors. In the context of searching for the resonance, these deviations, including the overall experimental resolution, are assigned to the contributions of the resonant cross sections. Thus, the negative resonant cross sections can be interpreted to indicate that the resonance signals are so small that they are overwhelmed by the experimental resolution. In this case, the upper limits for the resonant cross section set by the data usually are dominated by the experimental resolution and result in overestimated but conservative upper limits.

The upper limits for the energy-integrated cross section of the resonance are calculated at the standard and commonly used 90% confidence level. The method involved in obtaining the 90% CL limits is described here. Assuming the measured parameter $a = a_c \pm \sigma_a$ is purely statistically distributed, obeying a Gaussian distribution, where

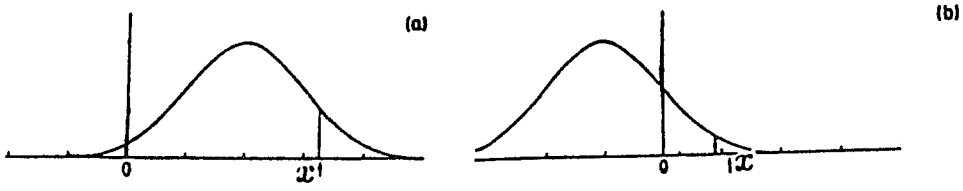

Figure 3.19: Determination of 90% Confidence Level. (a) $a_c > 0$, (b) $a_c < 0$.

a_c is the centroid and the σ_a is the error bar, then the distribution is given as,

$$g(a) = \frac{1}{\sigma_a\sqrt{2\pi}} e^{-\frac{1}{2}\left(\frac{a-a_c}{\sigma_a}\right)^2}. \tag{3.16}$$

If the parameter a only has physical meaning for $a \geq 0$, the upper limit value $a_{90\%}$ of parameter a at the 90% confidence level is determined by having 90% of the probability for the measured value satisfying $0 \leq a \leq a_{90\%}$ (illustrated in figure 3.19), ie,

$$\frac{\int_0^{a_{90\%}} g(a)da}{\int_0^{+\infty} g(a)da} = 0.9. \tag{3.17}$$

For each data point, the 90% CL value for the peak resonant cross section $a_{90\%}(M_{X^0})$ is evaluated. The energy-integrated resonance cross section within the detector acceptance in the CM system σ^d_{CM} is then calculated as,

$$\begin{aligned} \sigma^d_{CM}(M_{X^0}) &= \int_{CM} \frac{d\sigma_B}{d\Omega} d\Omega \int_0^{+\infty} \sigma(E_{CM}) dE_{CM} \\ &= \int_{CM} \frac{d\sigma_B}{d\Omega} d\Omega \int_0^{+\infty} a_{90\%}(M_{X^0}) \cdot \frac{J(q)}{p_+} dE_{CM}. \end{aligned} \tag{3.18}$$

For scalar and pseudoscalar couplings of the light neutral object X^0, the cross sections

are isotropic in space, and the total energy-integrated cross section can be scaled to the the entire solid angle simply by,

$$\sigma_{CM}(M_{X^0}) = \frac{4\pi}{\Omega_{CM}}\sigma^d_{CM}(M_{X^0}). \tag{3.19}$$

Figure 3.20(a) and (b) show the upper limits at 90% CL for the total energy-integrated resonant cross section measured by the experiment, for scalar and pseudoscalar couplings, in the entire mass region suggested by the GSI heavy-ion data. However, for the vector and axial vector couplings, the situation is more complicated, due to the θ angle dependence of the differential cross section. The resonant differential cross sections for both vector and axial vector couplings were discussed in chapter 2, section 2.2. Calculating the total energy-integrated cross section involves evaluating the ratio $\xi(M_{X^0})$ of the total resonance cross section to the resonant cross section covered by the detector acceptance of the experiment for such couplings. Equations 2.9 and 2.10 give the resonant cross section in the lab system. Transferring it to the CM system, the dependence of the resonant differential cross section on the θ_{CM} angle is

$$\left(\frac{d\sigma}{d\Omega}\right)_{CM} = C \cdot S_i(s,t,u), \tag{3.20}$$

where the $S_i(s,t,u)$, for different couplings $i = V, A$, are given in equation 2.10, C is a variable, independent of the polar angle θ_{CM}, s is the invariant mass. The Mandelstam variables t and u are related to the θ_{CM} angle of the scattered positrons according to the expression

$$u^2 + t^2 = \frac{1}{2}(s - 4m^2)^2(1 + \cos^2\theta_{CM}). \tag{3.21}$$

Integrating the detector volume in the CM system, we obtain the ratio $\xi(M_{X^0})$

$$\xi(M_{X^0}) = \frac{\int_{4\pi} S_i(s,t,u)d\Omega}{\int_{CM} S_i(s,t,u)d\Omega}. \tag{3.22}$$

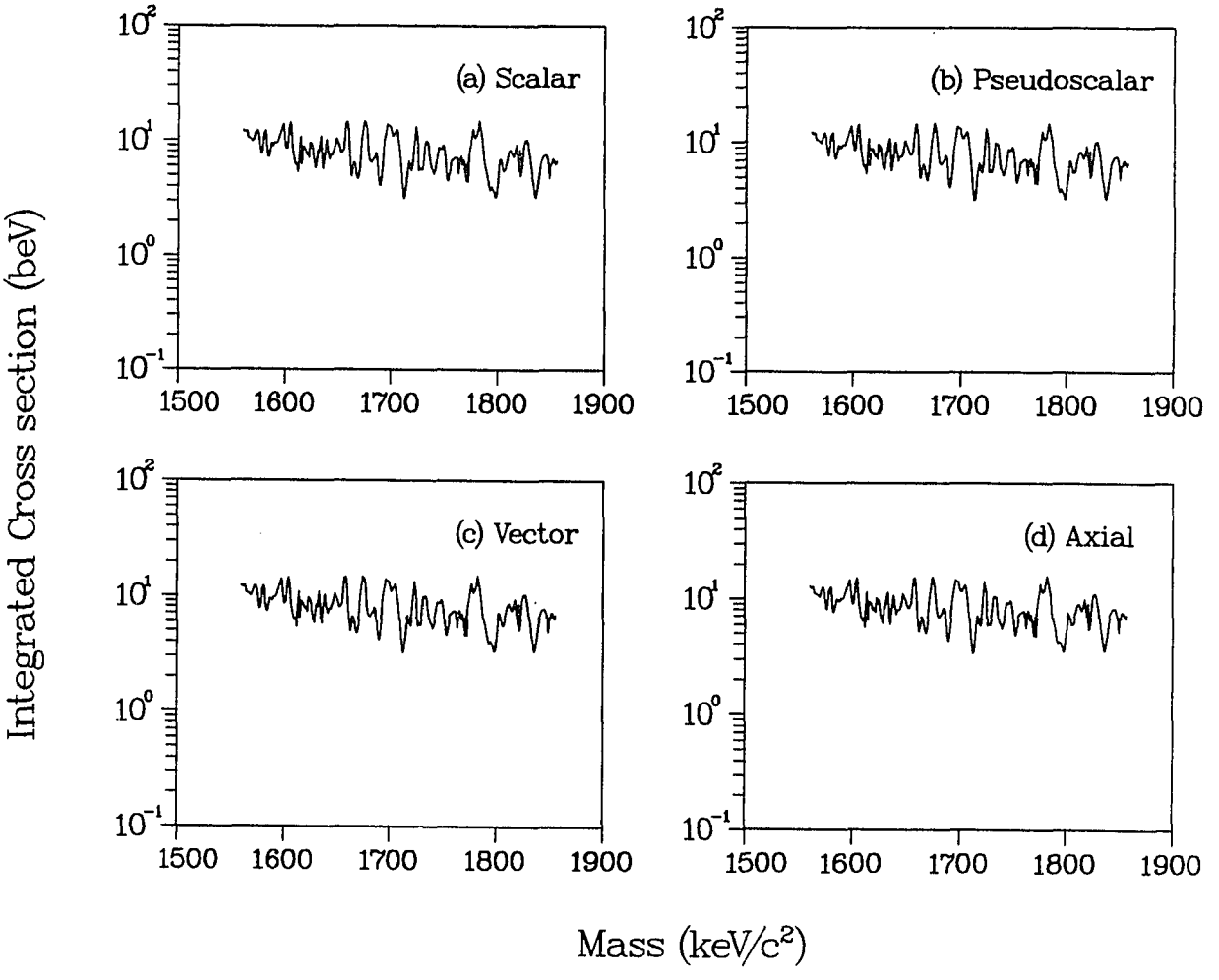

Figure 3.20: Upper limits at 90% CL for the total energy-integrated resonant cross sections for different couplings measured in the experiment. (a) Scalar coupling, (b) Pseudoscalar coupling, (c) Vector coupling, (d) Axial vector coupling.

Thus, the total resonant cross section in the CM system for vector or axial vector couplings is

$$\sigma_{CM}(M_{X^0}) = \xi(M_{X^0})\sigma^d_{CM}(M_{X^0}). \tag{3.23}$$

For vector and axial vector couplings, the 90% CL upper limits of the energy-integrated total resonant cross section set by this experiment are shown in figure 3.20(c)-(d) respectively. The corresponding intrinsic width and lifetime limits of the object are calculated in the following.

Constraints on Lifetimes of X^0s

As discussed earlier in section 2.2, the $\sim$ 10 meV intrinsic resonance width is significantly broadened by the electron momentum distribution to $\sim$ 7 keV. In turn, the total resonant cross section measured by the experiment is not the same as the initial intrinsic total resonant cross section. However, the energy-integrated resonant cross section is invariant for both the intrinsic and the experimentally observed values. Therefore, the 90% upper limits presented above for the energy-integrated resonant cross section are set to the object itself, independent of the specific experiment. Thus lifetime limits can be set for the light neutral object proposed to explain the GSI heavy-ion results.

The total intrinsic energy-integrated resonant cross section can be obtained from equation 2.6. With the energy-integrated cross section σ_{CM} measured in the experiment, the intrinsic width is obtained by

$$\sigma_{CM}(M_{X^0}) = 2\pi^2\lambda\!\!\!^{-2}\frac{2J+1}{(2s_1+1)(2s_2+1)}\Gamma_{e^+e^-}, \tag{3.24}$$

where $\lambda\!\!\!^{-} = \hbar/(M_{X^0} - 4m^2)^{1/2}$, s_1 and s_2 are the spin of the electron and of the positron, J is the spin of the object, with $J = 0$ for scalar and pseudoscalar couplings

and $J = 1$ for vector and axial vector couplings. Figure 3.21 shows the 90% CL upper limits for the intrinsic width as a function of the mass. Simply by the uncertainty principle $\tau = \hbar/\Gamma$, the 90% CL lower lifetime limits of the object can be obtained (figure 3.22).

In the entire mass region of 1560 keV $< M_{X^0} <$ 1860 keV, through elastic e^+e^-scattering, the average 90% lower limits of the lifetime for a short-lived light neutral object are $\tau > 3.3 \times 10^{-13}s$ and $\tau > 8.2 \times 10^{-13}s$ for $J = 0$ and $J = 1$ respectively, with the assumption that the e^+e^- decay channel dominates. The limits obtained are model independent, because the object is created on the mass-shell. This experiment provides the most stringent constraints on the couplings of the hypothetical object yet obtained. In the case of three-body decay of the object or some other competing decay channel openings, for instance the $\gamma\gamma$ decay channel, the experiment is not sensitive to these situations. However, for a three-body decay scenario, a discussion is given in the next section, in an attempt to isolate the three-body decay kinematics from the two-body decay kinematics of Bhabha scattering events.

3.6 Discussion

3.6.1 Two-body Decay Scenario

The aim of the experiment as well as the one described in reference [Hen88] was to search for a light neutral object decaying into the e^+e^- channel or with the e^+e^- channel having the dominant branching ratio. If decay channels other than e^+e^- open in the elastic e^+e^- scattering in the energy range of interest, the sensitivity of the experiment will certainly drop, depending on the branching ratio of the e^+e^- channel compared with the rest. The final lower limits on the lifetime of the object

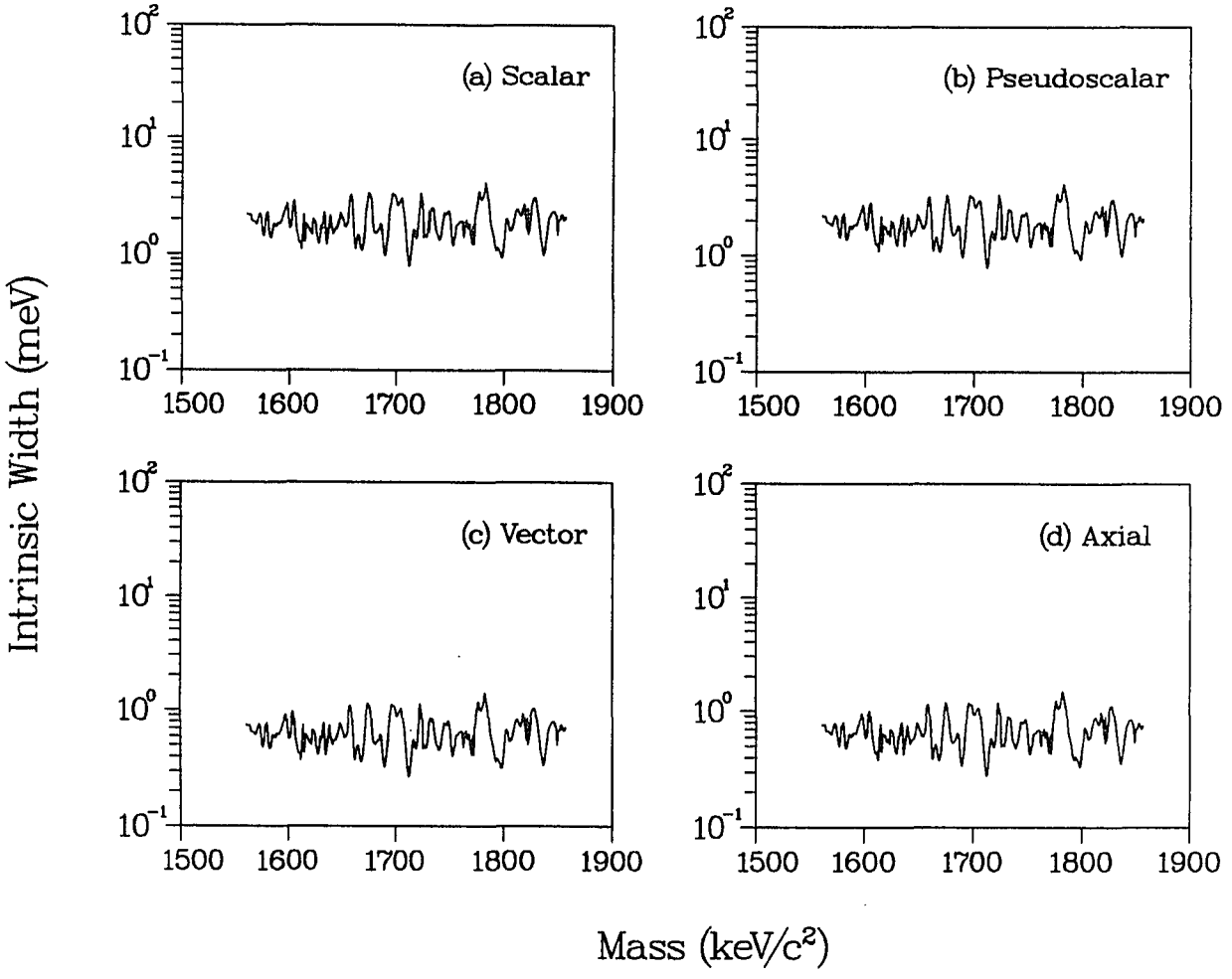

Figure 3.21: 90% CL upper limits for the intrinsic width measured by the experiment. (a) scalar coupling, (b) pseudoscalar coupling, (c) vector coupling, (d) axial vector coupling.

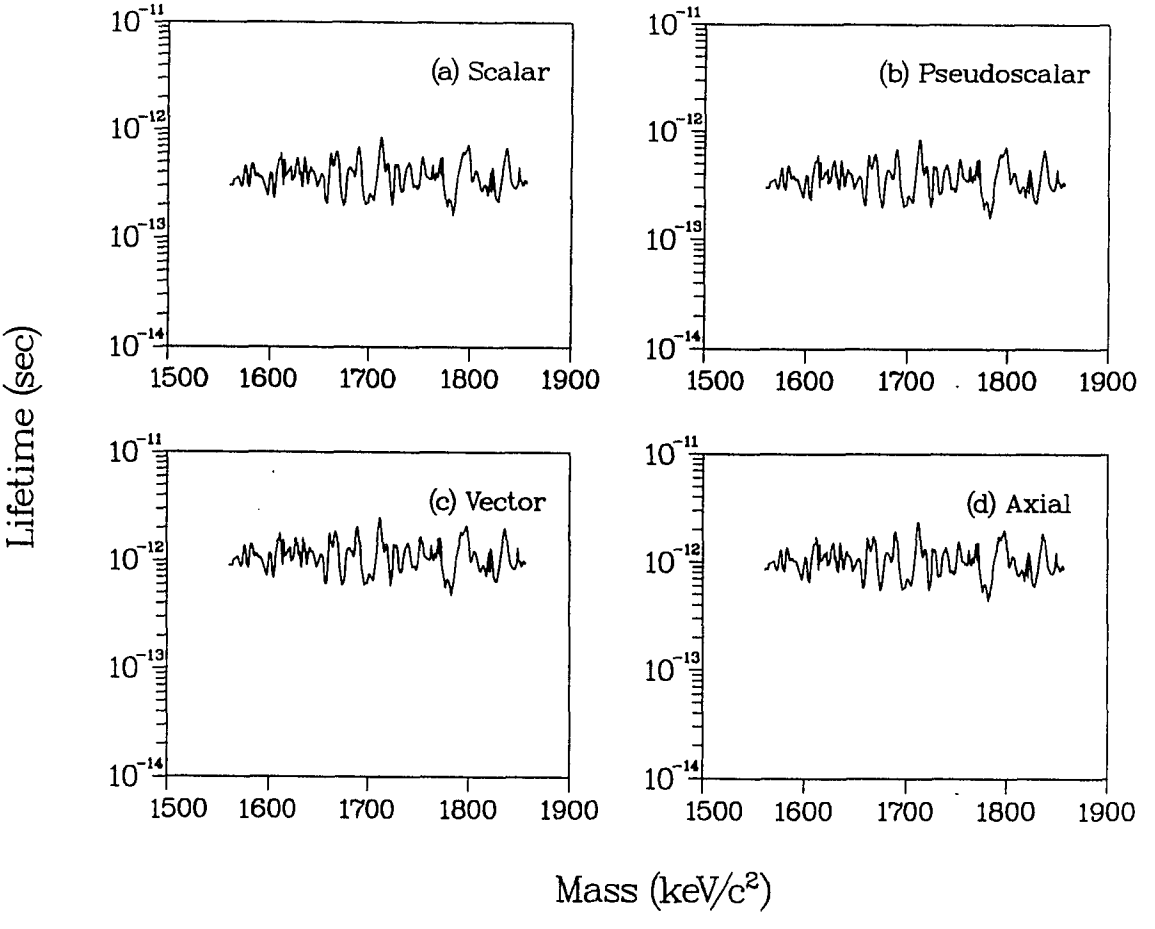

Figure 3.22: 90% CL lower limits for the lifetime measured by the experiment. (a) scalar coupling, (b) pseudoscalar coupling, (c) vector coupling, (d) axial vector coupling.

set by the experiment could be under-estimated. However, the kinematics of the GSI heavy-ion data seem to suggest a back-to-back two-body decay from a light neutral object into e^+e^-.

Recently some authors [Con88] proposed that in the case of strongly bound electron-positron pairs, the $\gamma\gamma$ decay channel might be dominant. With no bearing on the GSI e^+e^- decay channel, an experiment performed by Connell et al.[Con88] measured for the first time the structure in the two-photon annihilation-in-flight cross section of positrons . They covered the invariant mass region of $\sim$ 1222 keV $< M_{X^0} <\sim$ 1942 keV. No resonance structure was observed in their experiment. An upper limit on the ratio $\Gamma_{\gamma\gamma}/\Gamma_{e^+e^-} \leq 0.7$ at 810 keV was provided by the experiment. It is noted that this type of experiment is relatively simple compared with the e^+e^- channel measurements, since it is not necessary to use a monoenergetic positron beam. The positron energy can be determined by the photon sum energy itself. The $\gamma\gamma$ decay channel imposes the restriction of $J = 0$ state on the object by momentum conservation at the vertex.

In our experiment, the detectors are designed to suppress the γ background in order to improve the sensitivity for the e^+e^- decay channel. In the case of $X^0 \longrightarrow \gamma\gamma$, our experiment is insensitive: γ rays at the energy of interest penetrate the wire chamber without producing a signal, and the detector system is incapable of providing the necessary information.

3.6.2 Three-body Decay Scenario

The multi-line nature of the GSI heavy-ion data may indicate that the light neutral object X^0 has a few internal excited states. Transitions between these states are possible and corresponding γ rays may be emitted in the process. With such an extra

γ ray, the kinematics of the decay are totally different from those for the assumed two-body e^+e^- decay. The radiated γ ray carries both energy and momentum. In addition to the violation of the coplanarity of the debris e^+e^-, the spectrum of the e^+e^- sum energy is no longer a narrow line. Instead, in the three-body decay scenario, the energy distribution is continuous with a threshold at the high energy end.

In the context of the heavy-ion collision experiments, the specific narrow sum-energy line does not suggest multi-body decay. However, the multiple sum-energy lines could be explained naturally by the object X^0 having a few internal excited states. The consequence of these excited states is the introduction of the γ particle into the decay process. These two arguments are indeed contradictory, but it should be emphasized that the environment of the heavy-ion experiment itself is an extremely complex. In the e^+e^- scattering experiments, the situation is different from that in the heavy-ion collision experiments. A three-body decay process is not necessarily excluded.

As I have noted, our experiment was based on the two-body e^+e^- decay. Stringent constraints on the lifetime of the object were given by the experiment for the e^+e^- decay process. Within the context of the simple assumption that in the three-body decay process only a γ particle is introduced, the three-body decay scenario was also studied in our experiment. This emitted γ particle could not be seen in the detectors, but the detected e^+ and e^- would most likely be located on the edges, away from the dominant Bhabha scattering events in the histogram spectrum of the sum-energy $(T_+ + T_-)$ vs coplanarity $(|\phi_+ - \phi_-|)$. In this two-dimensional histogram, events from a two-body process were centered at $T_+ + T_- = T_{beam}$ and $|\phi_+ - \phi_-| = 180°$ (see figure 3.23). A few data points near the GSI 810 keV line were investigated for the three-body decay channel. Events having kinematics close to that of a two-body

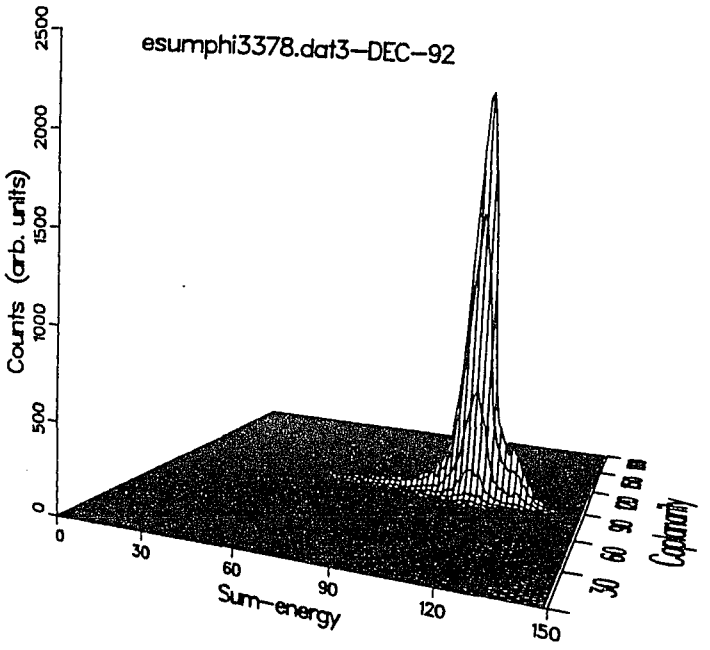

Figure 3.23: Typical sum-energy vs coplanarity spectrum from a two-body decay process. The spectrum was obtained at the beam energy of 2257.2 keV.

decay were cut out in the histogram, resulting in about $\sim$ 1200 events (see figure 3.24). These events have the largest deviation from the two-body decay kinematics. Multiple scattering in the target could cause the same kinematic deviation in the sum energy and coplanarity. Generally speaking, these events provided a smooth background. With a contribution from the three-body decay of the X^0, an excess in the event rate would be expected at the resonance energy.

The number of such events is normalized to the number of Mott scattering events, and the result is shown in figure 3.25. The actual cuts could not be placed on the sum-energy and coplanarity histogram already obtained from the two-body decay kinematics by eliminating the central two-body decay area, because the bin sizes of both energy and angle in the histogram were too large to provide good resolution for the cuts. The data displayed in figure 3.25 were obtained by re-running the original

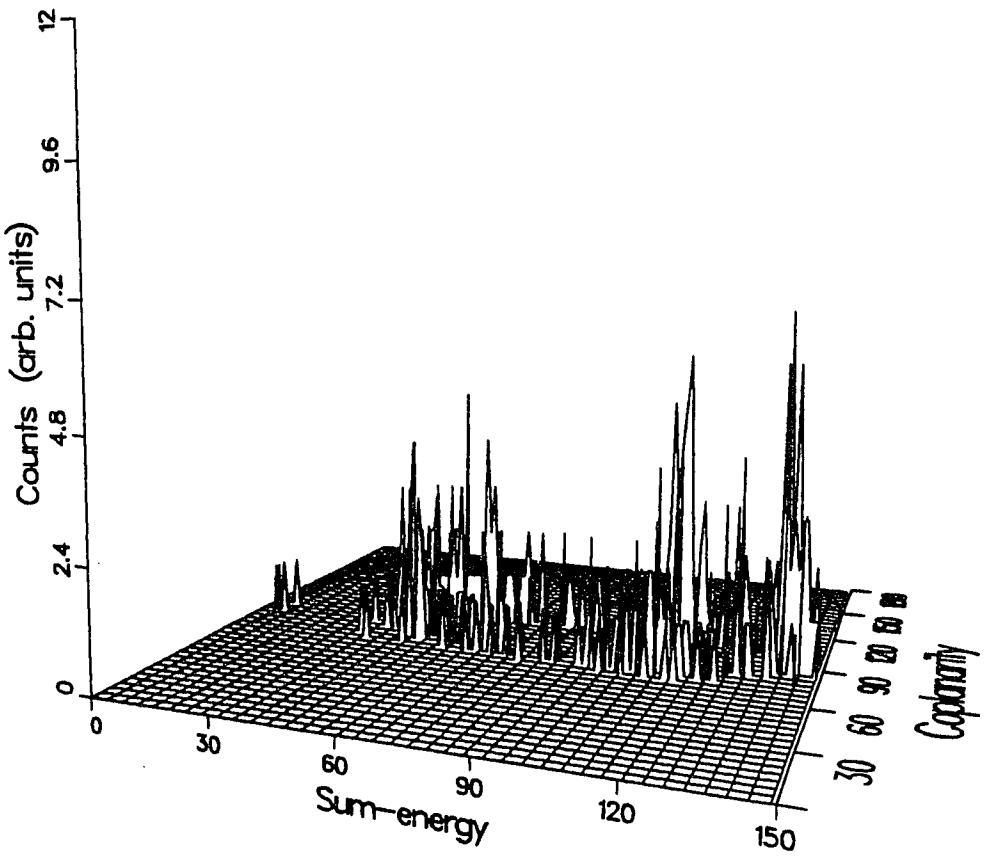

Figure 3.24: Event candidates from three-body decay process. Central two-body decay events were cut from the spectrum of sum-energy (in channels) vs coplanarity (in degrees) at an incident energy of 2257.2 keV. These residual events have the largest deviation from two-body decay kinematics in the data.

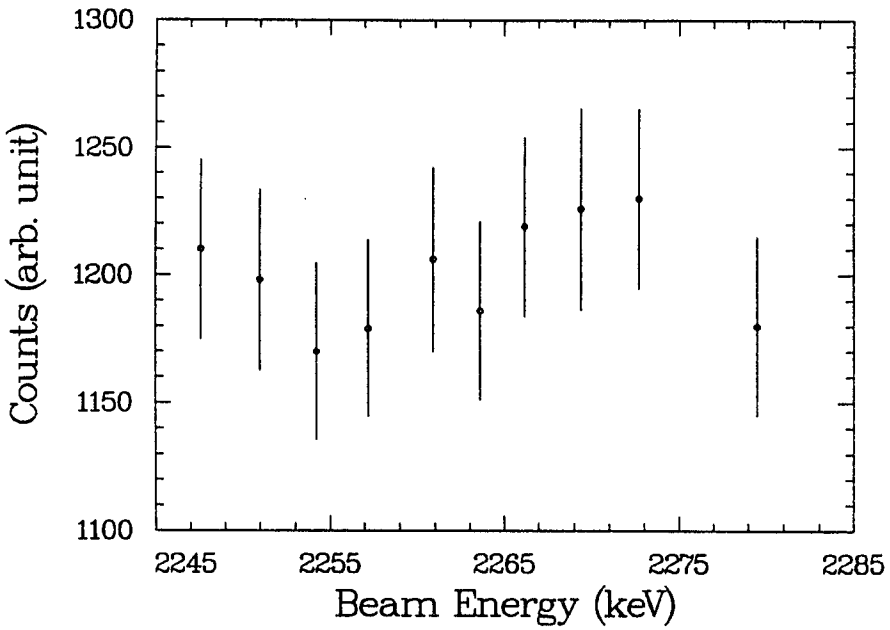

Figure 3.25: The total events with large deviation from simple two-body decay process, at energies near the GSI 810 keV sum-energy line. The area where the data cuts were applied is shown in figure 3.24. The total number of events shown here was normalized to the number of Mott events and scaled by a constant.

data tape and applying the kinematic cuts directly to all the events. Only a small region near the GSI 810 keV line was studied. No excess of counts was observed in this region within the statistical errors. It is possible that the real resonance signal is overwhelmed by the multiple scattering effects. It is hard to place a resonable lifetime limit on the three-decay of the X^0, simply because the detector system was initially designed for the two-body decay process. The statistics is rather poor after the events which obey tight two-body decay kinematics are eliminated, typically of the order of a few percent.

3.6.3 Systematic Errors

MWPC Efficiency Dependence

Stability of the wire chamber efficiency was checked for most of the runs, by measuring the centroid of the Landau distribution of each MWPC from the collected data. Changes in the wire chamber efficiency were related to a shift in the centroid. Fortunately no significant drift in the wire chamber efficiency was observed throughout the entire experiment. The wire chamber efficiency was obtained from the coincidence events. For example, if the number of good coincidence events in wire chamber 0 and its opposite wire chamber 2 is N_{02}, and the number of bad coincidence events is N_{02}^{bad}; when wire chamber 2 fired and wire chamber 0 did not fire, we have

$$\begin{aligned} N_{02} &= \epsilon_0 \epsilon_2 \sigma \\ N_{02}^{bad} &= (1-\epsilon_0)\epsilon_2 \sigma. \end{aligned} \tag{3.25}$$

Thus, knowing N_{02} and N_{02}^{bad}, the wire chamber efficiency ϵ_0 is given by

$$\frac{N_{02}}{N_{02}^{bad}} = \frac{\epsilon_0}{1-\epsilon_0}. \tag{3.26}$$

In the experiment, the wire chamber efficiency as a function of the centroid of Landau distribution was measured by varying the anode and cathode voltages. The Landau centroid was determined precisely by fitting the distribution with the formula

$$f(x) = a_3 ((x-a_1)/a_2)^{a_0-1} e^{((x-a_1)/a_2)^{a_0}}. \tag{3.27}$$

For all four wire chambers, the relationship of efficiency to Landau centroid was obtained (see figure 3.26). Generally, the efficiency reached maximum at an optimum voltage, which was then used for the actual runs. The efficiency varied a little for different wire chambers and was measured to be roughly 88%. Errors due to the wire chamber efficiency drift were correctable, since corrections could be applied to

the excitation function using the relationship shown in figure 3.26. The detector efficiency dependence of the excitation function is given by equation 3.11.

Target Position Dependence

Uncertainty in the target position also contributes to systematic errors in the final excitation function. The reason is that a shift in the target position results in uncertainty in determining the scattering kinematics. This will not change the ϕ angle since calculation of this angle does not rely on the target position, as long as the beam is well-centered on the axis. However, the target position is involved in calculating the CM θ angle. With the correct target position, the histogram of $|\theta_{e^+} - \theta_{e^-}|$ should be centered at 0°. With the experimental geometry, a 1 mm movement of the target in a direction parallel to the beam corresponds to a $\sim 1.5°$ shift in this histogram. This effect is also correctable. The target position was controlled within $\pm 25 \mu m$ with respect to the correct position, aligned with a telescope. Over months of data taking, the reproducibility of the target position was excellent. No observable target movement was found.

Beam Position Dependence

In the normal situation, the positron beam should be well-aligned with the central axis. There is no visual alignment for this. Misalignment of the beam could seriously affect the final data. This problem was solved in the initial design of the detector system by arranging the main detector system (MWPC's and scintillators) symmetrically around the beam axis. The symmetry of the detectors not only makes good beam alignment possible but also has the advantage of reducing the errors introduced by slight misalignment of the beam position. In the experiment, the correct beam

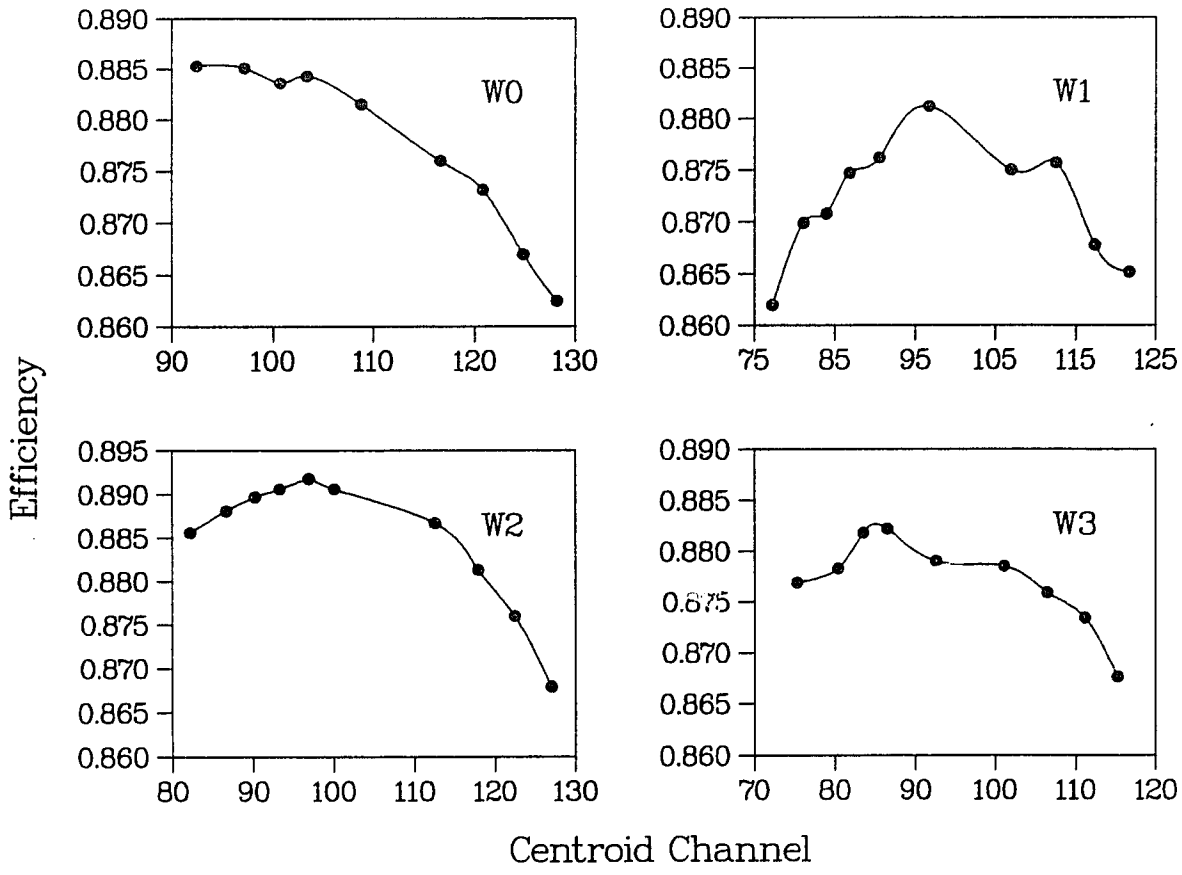

Figure 3.26: Wire chamber efficiency as a function of the centroid of the Landau distribution. The solid dots are the measured efficiency.

position was achieved by fine tuning the beam position until balanced Mott scattering count rates on the four wire chambers were reached. The count rates were monitored throughout the experiment. Slight beam position drift would appear as unbalanced count rates in the wire chambers. Moreover, the most important feature of a symmetrical detector system is error reduction. The reason is that in the case of a shift in the beam position in the direction of one wire chamber, that wire chamber becomes more effective, but the opposite wire chamber becomes less effective. Thus, the first order of deviation in the number of scattering events due to the beam position movement is cancelled in the detector system.

Beam Energy Dependence

The final excitation function was found to be insensitive to small positron beam energy drifts. In the analysis it was found that the value N_B/N_M hardly changed when the beam energy was artificially moved from its precise value by $\sim$ 2 keV. This large a drift was not expected to happen in the experiment. Hence, we conclude that the true beam energy shift, which was less than 1 keV, did not contribute to the final systematic errors significantly and could be ignored.

Gain Drift in the Electronics

A gain change in the electronics is difficult to deal with. Constantly calibrating the system might help to overcome the effect of the gain drifts on determining the energy of the scattered particles, but there is no method of stabilizing the gain of the anode resistive readouts. This type of error affects the kinematic reconstruction. Normally, gain drift in the electronics is hard to detect and is uncorrectable. No attempt was made for this type of error correction in the experiment. In fact, this error was carried

permanently into the overall systematic error of the final excitation function.

3.6.4 Where is the X^0?

A large number of experiments have been performed thus far to search for evidence of the existence of a light neutral object X^0, through various approaches. All of the results seem to exclude the possibility of the existence of such an object in the mass region of 1-2 MeV suggested by the GSI heavy-ion observations. The direct and model independent approach to investigate the issue is the e^+e^- scattering experiment. The s-channel Feynman diagram provides a resonance on the mass shell. The experiment described in this thesis systematically studied the e^+e^- scattering cross section at a sensitivity level of $\sim 0.3\%$ in a large mass region. The lifetime region of the object $\tau < 3.3\times10^{-13}$ s $(J = 0)$ was excluded by this experiment. Taken together with results from the other experiment performed by the same group [Hen88] which searched in a longer lifetime region, no evidence for the object was found in either experiment. As can see from figure 3.27, with the most sensitive e^+e^- scattering experiments performed by this group and other groups most of the previously open mass-lifetime areas for the existence of the new object have been covered.

The question now is, does the X^0exist? If the answer to the question is positive, then why have none of the experiments detected it? This question is extremely difficult to answer at this stage, since there is no detailed knowledge of the particle. The consistent and repeatable results from the heavy-ion experiments do coincide with the kinematics of a two-body decay process. However, it should be noted that the environment in the heavy-ion collision experiments is very complex. None of the experiments performed later to search for the particle had the same strong time-varying field which exists during the course of the heavy-ion collision. Celenza et al.

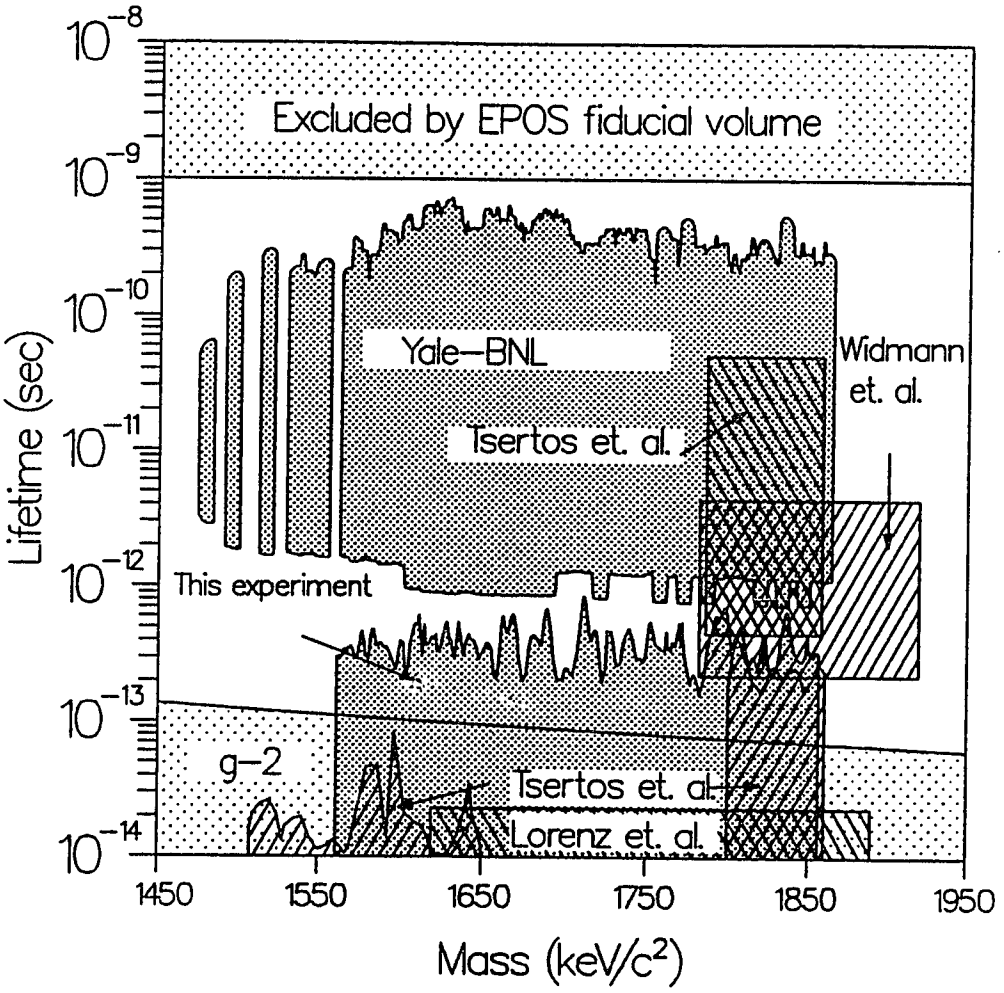

Figure 3.27: Results from the most sensitive e^+e^- scattering experiments performed thus far. The dashed areas are excluded by experiments. The results from this group cover most of the open region.

[Cel86, Cel87] pointed out that the X^0 might be produced in a new vacuum phase of QED which was provided by the heavy-ion collision environment. They predicted that while exotic states will continue to be seen in heavy-ion collisions, these states will not be excited in electron-positron collisions.

Moreover, the lifetime limits provided by the experiments using the active-target technique to suppress the non-resonant Bhabha scattering background still rely on the absorption cross section of the X^0 (for a detailed discussion on the absorption problem, see reference [Hen88]). Also, there is still a small gap in the lifetime region, $\sim 3.3 \times 10^{-13} < \tau <\sim 8 \times 10^{-13}$ sec. If experiments can be improved by another factor of 3, the gap will be filled and the entire range relevant for a particle interpretation of the correlated e^+e^- lines observed in the heavy-ion experiments would be covered.

The effects of the interaction of an extended particle with the targets is a fundamental question in all of the experiments which reached the long lifetime region. The direct elastic e^+e^- scattering experiment is a way toward a solution without involving the absorption problem. However, with a solid target the sensitivity is very limited. Experiments with better sensitivity in the e^+e^- scattering cross section were proposed. These experiments require magnetically confined free positrons at low temperature. In such cold gaseous targets, the momentum distribution of positrons is a few orders of magnitude less than that in a normal solid target, and in turn, a few orders of magnitude improvement in the resonance peak cross section is achievable. The final answer to whether a particle is the underlying cause of the GSI heavy-ion observation may be given by the next generation elastic e^+e^- scattering experiment, but technical difficulties still remain. In addition, a new heavy-ion experiment is being constructed at Argonne National Laboratory to study the detailed e^+e^- kinematics. More than an order of magnitude of improvement in the e^+e^- coincidence rate is

expected in this experiment. Also the detector system is more capable of measuring the precise kinematics of the e^+e^- coincidence events. We hope that these upcoming experiments with better sensitivity will give us a final answer to the question: **"Where is the particle X^0?"**.

3.6.5 Conclusion

In our search for a short-lived light neutral object X^0 which may be the underlying explanation of the observations in the GSI heavy-ion collision experiments, we found no evidence of the existence of the object in the entire mass range from 1560 keV to 1860 keV. To this date, among direct elastic e^+e^- scattering experiments performed utilizing solid targets, this experiment provides the the most stringent lifetime limits in the complete mass range. At invariant masses corresponding to the sum energy lines observed with heavy ions at 616, 750 and 807 keV, we obtain at the 90% CL values for the integrated cross sections of 8.44, 7.54 and 5.60 barn-eV, respectively, for the scalar coupling. These cross sections correspond to lifetimes of the object of $3.7 \times 10^{-13}, 3.2 \times 10^{-13}$ and 3.9×10^{-13} sec, for $J = 0$. In the case of $J = 1$, limits on the lifetimes then become $9.7 \times 10^{-13}, 8.1 \times 10^{-13}$ and 9.6×10^{-13} sec, respectively. On average, the existence of a light neutral object decaying into e^+e^- with lifetime $\tau < 3.3 \times 10^{-13}$ sec $(J = 0)$, and $\tau < 8.2^{-13}$ sec $(J = 1)$, has been ruled out in the mass range 1560 keV $< M_{X^0} <$ 1860 keV, at 90% confidence level. Systematic errors in the experiment are mainly those associated with the possible small efficiency drift of the detector system and the uncertainty in the target and positron beam position. These factors contribute less than $\sim$ 5% errors in the lifetime limits. Together with the earlier experiment [Hen88], the two experiments covered nearly the entire open mass-lifetime area of the particle X^0 suggested by the GSI heavy-ion observations.

Part II

Single-Quantum Annihilation of Positrons With Shell-Bound Atomic Electrons

Chapter 4

Single-Quantum Annihilation of Positrons With Shell-Bound Atomic Electrons

4.1 Overview

This chapter describes another experiment [Pal91] performed at Brookhaven National Laboratory using the 3-MeV positron accelerator. This experiment was performed during the summer of 1991. Several separate mono-energetic γ-ray peaks were observed from the annihilation of positrons with different atomic shell-bound electrons for the first time. In matter, several modes of e^+e^- annihilation are avaliable. An electron-positron pair can annihilate into one, two, three, or more photons. The cross sections for these annihilations vary by a few orders of magnitude. Among them, two-photon annihilation of the e^+e^- pair is the most favorable mode accounting for $\sim 97\%$ of the annihilation. When the positrons are stopped in the material, they will quickly

annihilate with electrons and produce two 511 keV photons. Two photon annihilation in flight takes up the remaining $\sim 3\%$ of the annihilation, in the usual condition. In the case of the $^3S_1$ state of the e^+e^- system, three-photon annihilation will take place. However, the probability is much less than that of the two-photon annihilation mode. The reason is that the $^3S_1$ state has a relatively long lifetime. In most metals, the $^3S_1$ state decays into the ground state $^1S_0$ before the three-photon annihilation takes place. Basically the three photon-annihilation mode can only happen in some gases, in which the transition from the $^3S_1$ state to the rapidly annihilating $^1S_0$ state is forbidden. In fact, applying the appropriate external magnetic field so that states with $m = 0$ can no longer be represented by pure singlet or triplet spins functions, the fraction of three-photon annihilation can be nearly 75%.

Annihilation modes resulting in more than three photons are also possible, but the cross sections decrease by powers of the fine-structure constant α as the number of emitted photons increases. In an experiment these high order annihilation modes are very difficult to observe due to their extremely small cross sections.

Free positrons and electrons cannot annihilate into one photon, because it is impossible to conserve both energy and momentum for the process. Thus this annihilation mode is forbidden by the conservation laws. But instead of the real process, the virtual process of single-photon annihilation can occur in the process of the e^+e^- interaction, in which only the momentum is balanced but not the energy. A large fraction of the positronium fine-structure splitting is caused by such virtual processes. In the process of Bhabha scattering (discussed in Part One of this thesis), this virtual process also contributes to the elastic e^+e^- scattering cross section.

However, in the presence of a third body, such as the nucleus, which will take away some of the momentum but negligible recoil energy during the annihilation process, it

becomes possible for a positron and electron pair to annihilate into only one photon. The cross section for this process is extremely small and strongly depends on the proximity of electrons to the nucleus. This process is called the Single-Quantum Annihilation of Positrons (SQA) and it was first proposed by E. Fermi [Fer33] in 1933.

Although the fundamental nature of SQA as an electrodynamic process of atomic physics has been well understood, there is no clear observation of this phenomenon experimentally. The reason is that, in addition to the extremely small cross section of the SQA process, the energy of the SQA photons depends on the energy of the incident positrons. In order to produce observable mono-energetic SQA photons, it is necessary to have an intense mono-energetic positron beam. Lacking such positron beams, all of the experiments performed previously to measure the SQA cross section utilized positrons from radioactive sources selected by spectrometers. These positrons from radioactive sources have a wide energy bandwidth. Therefore, no clear sharp SQA peaks would be expected in these experiments.

In the past decade, with the growth of positron solid state physics and the development of positron moderation, mono-energetic positron beams have been built. At Brookhaven National Laboratory, the 3 MeV Dynamitron linear accelerator is able to produce an intense mono-energetic positron beam with energy between $\sim$0.5 MeV and $\sim$2.8 MeV with an energy spread of less than 1 keV. This positron beam is ideal for the study of the SQA process. The beam characteristics were discussed in chapter 2. In our experiment, for the first time, unambiguous photon peaks from the annihilation of the positrons with K, L, and M shells of atomic bound electrons in a thin lead target were distinctly observed, and their corresponding cross sections determined. These results were published in **Physical Review Letters, 67**, 3491,

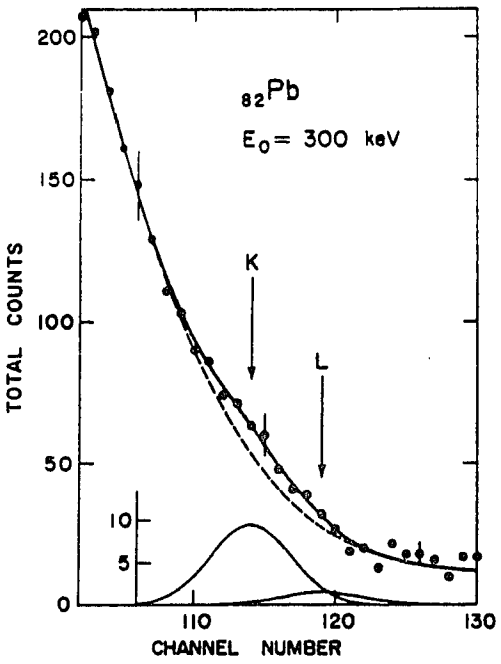

Figure 4.1: Observed SQA peaks from 300-keV positrons incident on a lead target. There is no clear observation of the K and L shell SQA photons. This figure is reproduced from reference [Muk79].

1991.

4.2 Motivation for This Experiment

This experiment was performed initially to study the SQA phenomenon as a QED process. The best existing experiments on this subject were carried out with positrons from radioactive sources, with energy selection made by magnetic spectroscopy and photon detection by NaI (Tl) scintillator-photomultiplier assemblies coupled with light pipes. The results of the cross sections were extracted from a change in the large photon background (see figure 4.1), with a possible mixture of K, L and M photons. Our initial motivation was to observe the SQA peaks clearly and measure their cross sections with better precision. During the experiment, it was realized that the SQA process cross section is very important to the lifetime of the heavy

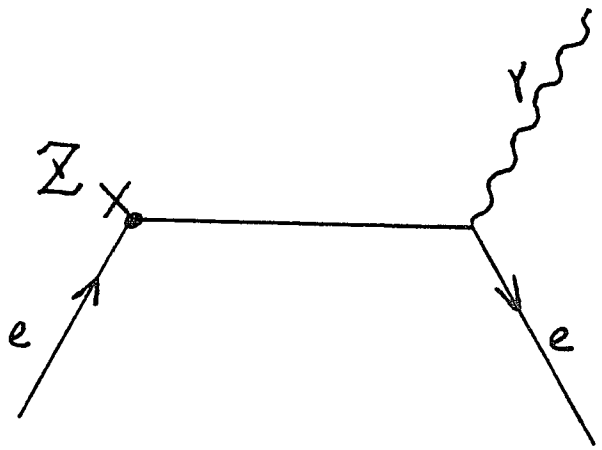

Figure 4.2: Feynman diagram for the SQA process.

ions stored in the Relativistic Heavy Ion Collider (RHIC) which is now being built at Brookhaven National Laboratory. At the collision point of two oppositely moving heavy ions in the storage ring, the two charged ions will come together close enough to produce a Coulomb field that is strong enough to create a positron-electron pair from the exchange photons. The electron will be captured by the ion, and the positron will be repelled from the ion by the Coulomb field. After the capture, the ion will lose its original charge state designed for its storage and eventually wander off the orbit. This is an important factor affecting the lifetime of the ion beam. There is no experimental cross section measured for this process. The QED calculation remains unchecked by experiments. However, since the SQA process is the time-reversed process of the one mentioned above (the Feynman diagram for the SQA process is shown in figure 4.2), the SQA cross section would be expected to be the same as the one in the case of heavy ions. Measuring the SQA cross section will help to verify the lifetime of the RHIC ions experimentally.

The SQA yield photons can be identified by their unique energy in the experiment. The energy itself is dependent on the incident positron energy. During the annihilation, the nucleus shares part of the total momentum, but it takes almost no energy because it is much heavier than the electrons and positrons. In such a case, the emitted photon has the initial total sum energy of the incident positron and the bound electron. It is given by

$$E^{\gamma} = -E^{e^-}_{shell} + E^{e^+}_{beam} + 2m_e c^2 \tag{4.1}$$

where $E^{e^-}_{shell}$ is the electron binding energy, $E^{e^+}_{beam}$ is the the kinetic energy of the incident positrons, and $2m_e c^2$ is the rest energy of the electron and positron.

The SQA differential cross section drops sharply with the angle. Thus using the features of the SQA phenomenon, it might be possible to obtain a tunable source of mono-energetic γ rays in the energy range from 1 MeV and up. It should be noted that γ rays produced by this process have some special merits: they are highly forward-peaked, have a narrow energy bandwidth, permit easy energy-tuning, and give a relatively high yield. This will be discussed in detail later in this chapter.

4.3 Theoretical Considerations

Theoretical calculations of the SQA cross section using the Born approximation and relativistic Hartree-Fock-Slater model were performed by W.R. Johnson et. al [Joh64, Bro72], with results showing a strong Z dependence. In the Born approximation, the matrix element is proportional to $Z^{5/2}$. This gives rise to an SQA cross section of magnitude $\sim \alpha^4 Z^5 r_0^2$, where α is the fine-structure constant and r_0 is the classical electron radius. It is expected that SQA accounts for $\sim$0.2% of the positron

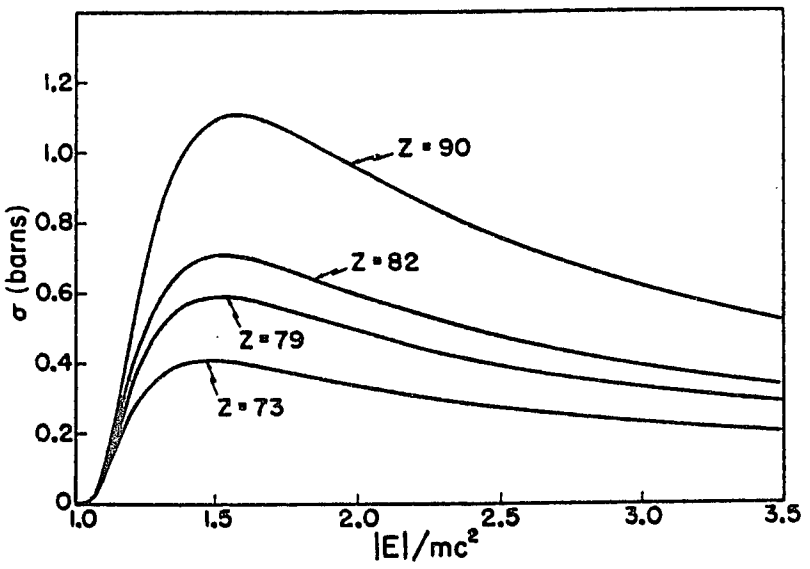

Figure 4.3: Numerical results for SQA cross sections for several high-Z elements, given by W.R. Johnson [Joh64].

annihilation in high-Z targets for a typical radioactive source. In their work, Johnson et al. noted that for elements with Z greater than 70, the Born parameter αZ is greater than 0.5 and the results of the Born approximation are no longer reliable. Instead, numerical results for the total cross section were given for a few heavy elements including lead which was used as the target in our experiment. The cross sections are depicted in figure 4.3.

A more recent calculation of the SQA cross section was carried out by H.K. Tseng and R.H. Pratt [Tse72] using the Hartree-Fock-Slater potential obtained with energy-shift screening theory for several high-Z targets. The cross sections are shown in table 4.1, and the K/L sub-shell ratio of cross sections is given in table 4.2.

Predicted simply as a result of the Coulomb potential, the emitted SQA photons are forward peaked. The differential cross section drops rapidly as the angle increases. K.W. Broda and W.R. Johnson calculated the differential cross sections for a few subshells in a lead target with unpolarized positrons at an incident energy of $E =$

E_+/m_ec^2	Z			
	47	74	82	90
	$\sigma_{HFS}(b)$			
2.00	0.0412	0.359	0.602	0.967
2.25	0.0338	0.319	0.530	0.849
2.50	0.0368	0.288	0.474	0.752
2.75	0.0351	0.263	0.429	0.677
3.00	0.0335	0.243	0.392	0.614
3.25	0.0319	0.226	0.361	0.561
3.50	0.0304	0.209	0.333	0.516

Table 4.1: K shell SQA cross section calculated with Hartree-Fock-Slater potential.

E_+/m_ec^2	Z		
	47	73	90
	σ_{1s}/σ_{2s}		
1.250	7.14	6.43	5.93
1.375	7.24	6.43	5.93
1.500	7.38	6.46	5.92
2.000	7.55	6.68	6.01
3.000	7.73	6.94	6.34

Table 4.2: Subshell ratio for K/L_I cross sections in the point-Coulomb potential.

$1.5m_ec^2$. The result is shown in figure 4.4. In addition, the spin of the positron is correlated with the polarization of the emitted SQA photon. Thus, with a polarized positron beam, the polarization of the emitted SQA photons is well defined.

4.4 Experimental Apparatus and Data Acquisition

4.4.1 The Z Dependence of the SQA Cross Section

The cross section for the SQA process is extremely small in a low Z target. This is mainly due to the weak binding of the electrons to the nucleus in the low Z target,

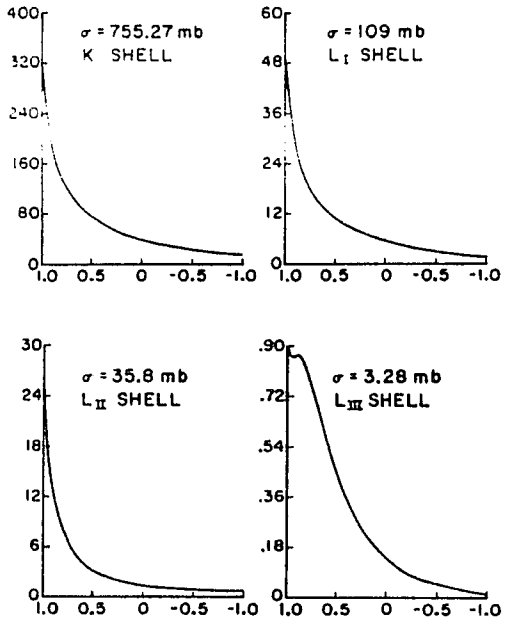

Figure 4.4: Differential cross section for SQA on Pb at the incident positron energy $E = 1.5m_ec^2$. The $d\sigma/d\Omega$ in mb/sr is plotted against $\cos\theta$. This plot is reproduced from reference [Bro72].

which makes the nucleus less favorable to participate in balancing the momentum during the SQA process. Theoretical prediction gives a Z^5 dependence of the SQA cross section. Results from experiments [Maz68] were in good agreement with the theory for $\sim$ 300-keV incident positrons. However, at higher positron energies, the exponent of the Z dependence seemed to be less than that given by theory. The result of Friedrich [Fri71] was 3.2-3.8 for incident positron energies of 760-1100 keV. It should be noted that all the cross section calculations in these experiments were based on the extraction of SQA photons from a large photon background and thus uncertainties could be introduced.

The experiment reported here did not measure the Z dependence of the SQA cross section. Instead, only a thin lead target with a thickness of 3.25 mg/cm^2 and a diameter of 2.5 cm was employed. In this thin Pb target, small energy loss ($\sim$ 3 keV) was expected, causing the energy spread in the target to be less than the L

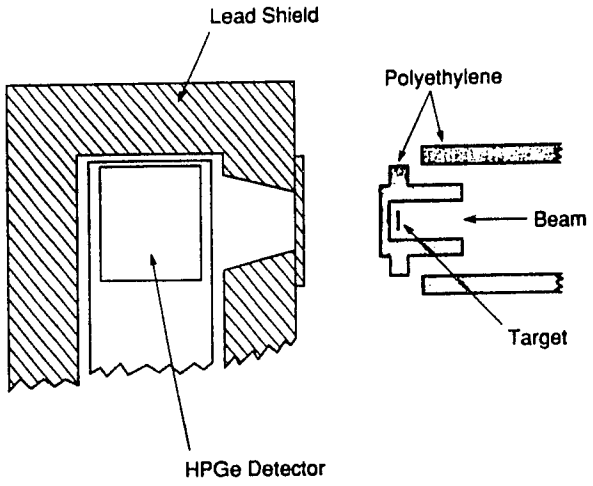

Figure 4.5: The target and detector setup for SQA measurement.

and M shell separation (12 keV). In the experiment, while choosing a high Z lead material as the SQA production target, a low Z material can be utilized as the positron beam stopper. Almost no SQA photons are expected from a low Z target such as polyethylene.

4.4.2 Experimental Setup

The beam transport and monitoring system is the same as that described in previous chapters. The detector system is however much simpler. Figure 4.5 shows the target and detector setup. The photon spectrum was recorded with a HPGe detector of 45% relative efficiency. The incoming positron beam interacts with the Pb target and is then stopped by the polyethylene lining. The detector is mounted on a rotatable table for angle dependence measurements. The natural radiation background is reduced significantly (over an order of magnitude) by having the detector surrounded by 5.1-cm-thick lead shielding with only an opening of the acceptance window of 0.160 sr.

The detector is also lined with a 0.3-mm-thick tungsten sheet inside the lead shield, which reduces the detection of low-energy photons originating from the lead shield. Pulse signals are first amplified by an ORTEC preamplifier and then amplified by an ORTEC 572 amplifier. The spectrum is recorded with the Canberra S100 MCA system. The data acquisition system is straight forward. The main effort in this experiment is focused on reducing the natural and beam-induced background in the region where the SQA photons are expected, in order to observe the relatively small SQA production cross section. The energy of the positron beam is stabilized and drifts less than 1 keV during a typical two-day data collection.

The net background was studied with care both with and without the beam to distinguish the roles of natural radiation and beam-induced processes. In the photon energy region of 1.7 MeV and up, the background is a few orders of magnitude less compared with that in the low energy region. Several peaks due to ^{214}Bi and ^{208}Bi in the concrete wall are identified in the region of interest. Since the SQA peaks depend on the beam energy, the positron beam energy is tuned to avoid these natural peaks. In the experimental runs for determining beam-induced background, the lead target is replaced with a plastic foil, which produces practically no SQA photons. The 511-keV annihilation radiation could contribute signals to the region of interest (around 2 MeV for 1-MeV position energy) due to pile-up effects. Other likely contributions could come from bremsstrahlung and two-quantum annihilation in flight produced by the polyethylene beam stopper. At a beam energy of 1 MeV, the former could yield photons with energies up to 1 MeV, and the latter between 0.30 and 1.72 MeV. The cross section for two-quantum annihilation in flight is estimated to be 6.5 times larger in lead for 1-MeV positron energy than that of the single-quantum process.

However, since the nucleus plays no role in the momentum conservation in the two-quantum annihilation process, this pair of photons is emitted with an opening angle much larger than 26°, the maximum that would permit both of the two emitted photons to be detected and to contribute to the SQA peaks. Overall, the pile-up of pulses from various single photons accounts for about 60% of the background level in the SQA region (1900 to 2070 keV). From our detailed observation, it is seen that the background is linear in the region of interest, devoid of any observable peaks. The pile-up effects are brought down to moderate levels by having the acceptance window of detector covered with thin lead sheets of total thickness of 9.73 mm. The integral count rate is reduced by a factor of 5, to 1.3 kHz. However the potential SQA detection rate is also reduced by a factor of 2. This attenuation of signals will be accounted for later in the calculation of absolute differential cross sections. Figure 4.6(a) shows the background with the positron beam at 1.007 MeV incident on a plastic target. The inset expands the region of interest.

4.4.3 Observation of the K, L and M photo-peaks

With the 3.52 mg/cm^2 Pb target, the energy spectrum of the SQA annihilation at 0° is shown in figure 4.6(b). This spectrum was obtained over 87 hours with the incident positron beam energy at 1.007 MeV. The binding energies of the K, L and M shell electrons in lead are 88.01, 15.86 and 3.85 keV, respectively. At the incident energy given above, the K, L and M SQA photo-peaks were produced at 1.941, 2.013, and 2.025 MeV, respectively. Data were also taken for SQA at 30°, 45°, 60° and 75° at a beam energy of 1.007 MeV. In addition, measurements were made with beam energies of 1.482 and 2.014 MeV at 0° and 30°. Separate photo-peaks from the three electron-shells mentioned above were seen in these measurements.

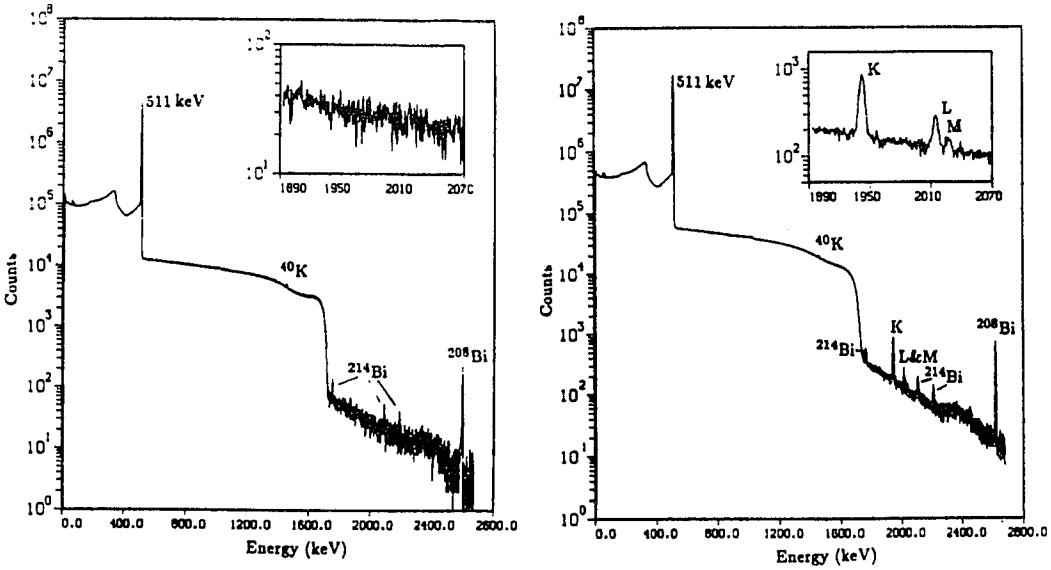

Figure 4.6: Energy spectrum measured by HPGe detector (shielded) at an incident positron energy of 1.007 MeV. (a) With the plastic target, no SQA photons were observed. (b) With the lead target, K, L and M photo-peaks were clearly resolved.

4.5 Data Analysis and Results

With the beam at 1.007 MeV incident on a 3.52 mg/cm^2 lead target, three distinct SQA peaks are clearly observed. The K peak is at 1.914 MeV. The L peak has a $\sim$72-keV shift towards higher energy, and the M peak is shifted by a further $\sim$12 keV. The centroids and widths of these three peaks are determined by fitting the peaks with a Gaussian plus a linear background. Due to the finite detector energy resolution (2.5 keV) and the energy spread in the lead target (3 keV), the width (FWHM) of SQA photons is nearly 4 keV. The precise separation of the lines and their sub-lines can be determined from atomic spectroscopic data. The observed extra shift for L and M can then be attributed to the contribution of the sub-shells. The calculation is presented in the following sections.

4.5.1 Differential cross section

Certain corrections are required in the determination of the absolute values of the differential cross sections of the SQA with K, L, and M shell electrons. An estimated 0.6% of the incident positrons are backscattered by the lead target without participating in the SQA process. Also reduction of the SQA photon intensity by the thin lead absorber covering the acceptance window of the Ge detector is a very significant correction, which is done with a 3% uncertainty. The photopeak efficiency of the detector is determined experimentally with standard gamma-ray sources positioned in front of the acceptance window of the detector-shield system at the same distance as the target. We expect an accuracy better than 5% for this measurement. Another 5% uncertainty is attributed to the determination of the beam intensity during a few days of continuous measurement. The beam intensity was measured by periodically

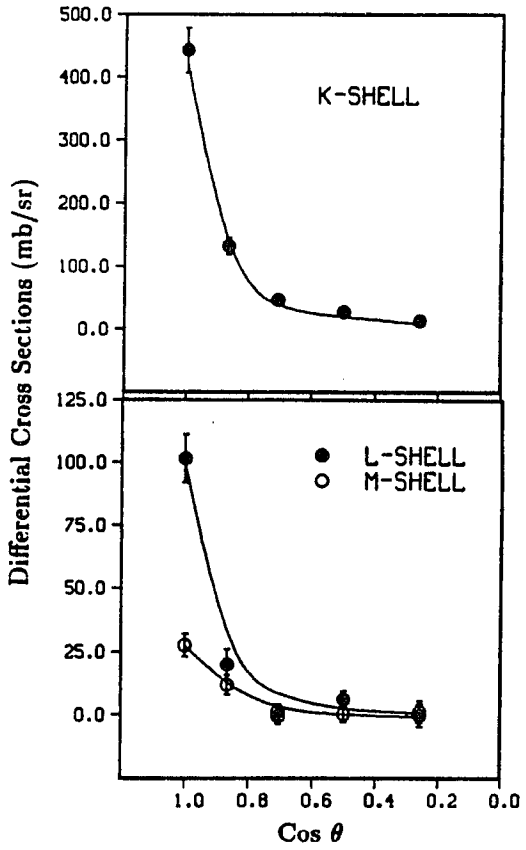

Figure 4.7: SQA differential cross sections measured by the experiment for 1.007 MeV positrons.

steering the beam onto the scintillator in the beam monitoring system. This provided a measurement of the beam rate at a specific time. Also with appropriate calibration of the system, the overall number of incident positrons could be determined by measuring the total number of 511-keV photons in the spectrum. The results were consistent.

Other factors that play a role in determining the absolute differential cross section of the SQA process are the rather large acceptance angle of the detector ($\sim 13°$) and the straggling of the positrons in the target. The former could be eliminated by moving the detector further away from the target. The proposed new experiment on SQA to measure the cross section with better precision will make this modification. This requires much longer beam time in order to obtain the same statistics. The straggling of positrons in the target can only be reduced by utilizing a thinner target, at the price of decreasing the SQA photon intensity. For the present data, corrections produced by these two factors were taken into account in the calculation. It is estimated that an overall systematic error of $\sim 8\%$ is allowed in the final result. Compared with the statistical uncertainty of 1.4% for K shell data at 0°, the systematic error dominates the total uncertainty in the cross section measurements. Nevertheless, since no other clear observation of the SQA data exists thus far, our data provide the best results for the differential cross section values. The SQA cross sections for the K, L and M peaks are depicted in figure 4.7. No theoretical data are available for the differential cross sections at this energy for a Pb target. However, the sharply forward-peaking feature of the SQA photons is in agreement with the theory.

4.5.2 Total SQA cross section

At a positron energy of 1.007 MeV, the calculation given by Johnson et. al. [Joh64, Joh67] for the total K shell SQA cross section is 397 mb, without correction for the screening effect. A 1% effect could be possible due to the screening correction.

The total cross section was evaluated by integrating the differential cross section. However, the differential cross section measurement by this experiment is only extended to 75°. With the integration only up to this angle, the K shell cross section given by the experiment is 360 mb. The theory indicates that the contribution to the total cross section for the K shell from the angle 75° and above is about 5%. With a 50% error margin allowed for this estimation, the experiment gives a K shell total cross section of 378 ± 32 mb. Within the uncertainties, our result agrees well with the theoretical prediction.

4.5.3 L/K and M/K ratios

The K, L and M SQA photon peaks are fitted with a Gaussian plus a linear background resulting in a Chi square close to 1.0 (typically 0.98 to 1.08) for the K shell. The total counts in these regions are obtained. Since only the ratio is needed, only minor corrections to the data are necessary. The shell-ratio information is directly obtainable from the fitting. The L/K and M/K ratios as well as the K differential cross sections at 0° and 30° for the three incident positron energies are listed in table 4.3. The result is consistent with the value of $L/K = 0.2$ for the theoretical integral cross section, but owing to experimental uncertainties, the ratio for angles larger than 30° is not useful for comparison. No theoretical analysis is available for the M/K ratio.

It is found from the experiment that the SQA photons are more forward peaked

Energy (MeV)		K (mb/sr)	L/K ratio	M/K ratio
1.007	0°	442 ± 36	0.23 ± 0.1	0.06 ± 0.01
	30°	132 ± 13	0.15 ± 0.05	0.09 ± 0.04
1.482	0°	495 ± 54	0.22 ± 0.03	0.07 ± 0.02
	30°	83 ± 16	0.20 ± 0.10	0.02 ± 0.07
2.014	0°	545 ± 61	0.25 ± 0.03	0.03 ± 0.02
	30°	61 ± 14	0.11 ± 0.09	-0.15 ± 0.08

Table 4.3: Measured K shell differential cross sections at 0° and 30°, and the L/K, M/K ratios.

as the energy increases. Although the total cross section decreases with increasing energy, the differential cross section at 0° actually increases.

4.5.4 Sub-shells of L and M

The K shell has no related subshells, L has three sub-shells and M has five sub-shells. The expected FWHM of the photo-peaks are much wider than the sub-shell separations. The FWHM of the photo-peak is due mainly to the contributions from the HPGe detector resolution (2.5 keV), the energy spread of the incident positrons in the lead target (3 keV), and the incident beam energy spread. The measured SQA photo-peaks have a consistent FWHM of $\sim$ 4 keV. This verifies that the long-term beam energy spread is very small ($<$ 1 keV). With a 4 keV width for the photo-peaks, the fine structure of the SQA peaks due to various sub-shell electrons is not expected to be resolved directly.

However, certain sub-shell information can be extracted from the data. The small separations in the binding energy ($\sim$ 1 keV for Pb) of the L_I, L_{II}, and L_{III} have two effects on the L photo-peak. First, a slight shift of the centroid is expected. Second, broadening in the FWHM of the L and M photo-peaks compared with the K photo-peak should be seen in the data. In fact, a slight energy shift of the L

peak toward higher energy is observed in the experiment. However, as a result of the poor statistics, the resolved FWHM of the photo-peaks has large error bars and thus cannot be used for the sub-shell measurement. Attempts were made to extract the $(L_{II} + L_{III})/L$ ratio by the peak broadening, but it turned out that this method was less sensitive than the one using the centroid shift.

The sub-shell ratio $(L_{II} + L_{III})/L$ was determined by fitting the L photo-peak with the sum of two Gaussians having a fixed separation equal to the difference of the binding energy of the sub-shell electrons, in the presence of a linear background. The two Gaussians represent SQA photons from the L_I shell and the sum of L_{II} and L_{III} sub-shells, respectively. At 0°, the fitting resulted in a ratio of $(L_{II} + L_{III})/L = 0.42 \pm 0.15$, which is in agreement with the theoretical value 0.3. Limited by the statistics in the photo-peaks, we failed to resolve any information pertaining to the L_{II} and L_{III} separately, and no sub-shell information was obtained for the M photo-peak.

4.6 Discussion

4.6.1 Possible Applications of the SQA Phenomenon

As mentioned above, the SQA photons have potentially useful characteristics. These gamma-rays are highly directional, mono-energetic and of tunable energy. In the forward direction, with the incident positron energy at 1 MeV, the yield of SQA photons is about 7×10^{-7}/sr per positron. As the energy increases, the differential cross section at 0° also increases. As an estimate, at an energy over 10 MeV, photon production of the order of 10^{-6}/sr per positron would be expected. This yield is higher by orders of magnitude than other tunable gamma-ray sources under development

[Lin91]. Positron beams with intensities of $\sim 10^{10}e^{+}/s$ can produce a large photon flux through the SQA process. The polarization of the SQA yield photons can be obtained, since only the polarization of the incident positrons is required. A gamma-ray source with these merits could find many applications in research and other areas.

4.6.2 Outlook of the Future SQA Experiment

At Brookhaven National Laboratory new experiments on SQA have been proposed. The new set of experiments will study the Z dependence with better accuracy. The Z^5 dependence of the SQA cross section given by the Born approximation will be tested in the energy range 0.8-2.8 MeV. Also, the effect of SQA on channeling will be studied. It is expected that in the channeling direction of a thin crystal, no SQA photons will be produced. At the same time, work on polarizing the incident positron beam will be done to study the polarization of the yield SQA photons.

4.6.3 Conclusion

The single-quantum annihilation of positrons with shell-bound atomic electrons was studied experimentally with the Brookhaven 3 MeV mono-energetic positron beam and a thin lead target. For the first time the SQA photo-peaks from three different atomic shell electrons were observed distinctly. At 1.007 MeV, the differential cross sections of the positrons annihilating with K, L and M shell electrons were measured. The ratios of L/K and M/K cross sections were also determined. The sub-shell ratio $(L_{II} + L_{III})/L$ was analyzed using the centroid shift of the L^{-} photo-peak. The results were all in agreement with theory. The observation indicated the possibility of applying the SQA phenomenon to the development of a tunable, highly directional gamma-ray source.

Bibliography

[Ash54] Arthur Ashkin, Lorne A. Page, and W.M. Woodward. Electron-electron and positron-electron scattering measurements. *Physical Review*, 94:357, 1954.

[Bab86] C.V.K. Baba, D. Indumathi, Amit Roy, and S.C. Vaidya. Search for a light neutral particle in the decay of the 3.68 MeV state in ^{13}C. *Physics Letters B*, 180:406, 1986.

[Bar87] Chr. Bargholtz, L. Holmberg, K.E. Johansson, D. Liljequist, P.-E. Tegnér, L. Bergström, and H. Rubinstein. Investigation of anomalous spectral structure in low-energy positron scattering. *Journal of Physics G*, 13:L265, 1987.

[Bar89] Chr. Bargholtz, L. Holmberg, K.E. Johansson, D. Liljequist, P.-E. Tegnér, and D. Vojdani. Spectral structure of 245–445 keV electrons and positrons in positron-Thorium scattering. *Physical Review C*, 40:1188, 1989.

[Bec79] D.J. Bechis, T.W. Dombeck, R.W. Ellsworth, E.V. Sager, P.H. Steinberg, L.J. Tieg, J.K. Yoh, and R.L. Weitz. Search for axion production in low-energy electron bremsstrahlung. *Physical Review Letters*, 42:1511, 1979.

[Bla52] J.M. Blatt and V.F Weisskopf. *Theoretical Nuclear Physics.* Wiley, New York, 1952.

[Bod85] G.T. Bodwin, D. Yennie, and M. Gregorio. *Rev. Mod. Phys.*, 57:723, 1985.

[Boe86] F.W.N. De Boer, K. Abrahams, A. Balanda, H. Bokemeyer, R. Van Dantzig, J.F.W. Jansen, B. Kotlinski, M.J.A. De Voigt, and J. Van Klinken. Search for short-lived axions in a nuclear isoscalar transition. *Physics Letters B*, 180:4, 1986.

[Bro72] K.W. Broda and W.R. Johnson. Single-quantum annihilation of positrons by screened k- and l-shell electrons. *Physical Review A*, 6:1693, 1972.

[Bro86] C.N. Brown, W.E. Cooper, D.A. Finley, A.M. Jonckheere, H. Jostlein, D.M. Kaplan, L.M. Lederman, S.R. Smith, K.B. Luk, R. Gray, R.E. Plaag, J.P. Rutherfoord, P.B. Straub, K.K. Young, Y. Hemmi, K. Imai, K. Miyake, Y. Sakai, N. Sasao, N. Tamura, T. Yoshida, A. Maki, J.A. Crittenden, Y.B. Hsiung, M.R. Adams, H.D. Glass, D.E. Jaffe, R.L. McCarthy, J.R. Hubbard, and Ph. Mangeot. New limit on axion production in 800-GeV hadronic showers. *Physical Review Letters*, 57:2101, 1986.

[Cel86] L.S. Celenza, V.K. Mishra, C.M. Shakin, and K.F. Liu. Exotic states in QED. *Physical Review Letters*, 57:55, 1986.

[Cel87] L.S. Celenza, Chueng-Ryong Ji, and C.M. Shakin. Nontopological solitons in strongly coupled QED. *Physical Review D*, 36:2144, 1987.

[Cle84] M. Clemente, E. Berdermann, P. Kienle, H. Tsertos, W. Wagner, C. Kozhuharov, F. Bosch, and W. Koenig. Narrow positron lines from U-U and U-Th collisions. *Physics Letters B*, 137:41, 1984.

[Con88] S.H. Connell, R.W. Fearick, R.F.A. Hoernlé, E. Sideras-Haddas, and J.P.F. Sellschop. *Physical Review Letters*, 60:2242, 1988.

[Cow86] T. Cowan, H. Backe, K. Bethge, H. Bokemeyer, H. Folger, J.S. Greenberg, K. Sakaguchi, D. Schwalm, J. Schweppe, K.E. Stiebing, and P. Vincent. Observation of correlated narrow-peak structures in positron and electron spectra from superheavy collision systems. *Physical Review Letters*, 56:444, 1986.

[Cow88] T. Cowan. *Monoenergetic Positrons and Correlated Electrons from Superheavy Nuclear Collisions.* PhD thesis, Yale University, 1988.

[Dav86] M. Davier, J. Jeanjean, and H. Nguyen Ngoc. Search for axion-like particles in electron bremsstrahlung. *Physics Letters B*, 180:295, 1986.

[Dov83] R. Dovesi, E. Ferrero, C. Pisani, and C. Roetti. Ab initio study of the electron momentum distribution of metallic Lithium. *Zeitschrift für Physik B*, 51:195, 1983.

[Dyc84] Jr. R.S. Van Dyck and E.N. Fortson. World Scientific, Singapore, 1984.

[Eis72] P. Eisenberger, L. Lam, P.M. Platzman, and P. Schmidt. X-Ray Compton profiles of Li and Na: Theory and experiments. *Physical Review B*, 6:3671, 1972.

[Erb86] K.A. Erb, I.Y. Lee, and W.T. Milner. Evidence for peak structure in e^+ + Th interactions. *Physics Letters B*, 181:52, 1986.

[Fer33] E. Fermi and G.E. Uhlenbeck. *Physical Review*, 44:510, 1933.

[Fri71] H. Friedrich. *Z. Phys.*, 246:407, 1971.

[Gre85] W. Greiner, B. Müller, and J. Rafelski. *Quantum Electrodynamics of Strong Fields.* Springer-Verlag, Berlin, 1985.

[Hal86] A.L. Hallin, F.P. Calaprice, R.W. Dunford, and A.B. McDonald. Restrictions on a 1.7 MeV axion from nuclear pair transitions. *Physical Review Letters*, 57:2105, 1986.

[Hen88] S.D. Henderson. *A Search for Low-Mass Long-Lived States Coupling to e^+e^-, Ph.D. thesis.* PhD thesis, Yale University, 1988.

[Hen92] S.D. Henderson, P. Asoka-Kumar, J.S. Greenberg, K.G. Lynn S., McCorkle, J. McDonough, B.F. Phlips, and M. Weber. Search in s channel for production of 1-2 mev long-lived e^+e^- resonances. *Physical Review Letters*, 69:1733, 1992.

[Ion88] D.C. Ionescu, J. Reinhardt, B. Müller, W. Greiner, and G. Soff. Nonlinear interactions and poly-positronium bound states. *Journal of Physics G*, 14:L143, 1988.

[Jac80] P.F. Jacques, M. Kalelkar, P.A. Miller, R.J. Plano, P. Stamer, E.B. Brucker, E.L. Koller, S. Taylor, C. Baltay, H. French, M. Hibbs, R. Hylton, K. Shastri, and A. Vogel. Search for prompt and penetrating neutral particles in a beam-dump experiment at brookhaven national laboratory. *Physical Review D*, 21:1206, 1980.

[Joh64] W.R. Johnson, D.J. Buss, and C.O. Carroll. Single-quantum annihilation of positrons. *Physical Rewiew*, 135:1232, 1964.

[Joh67] W.R. Johnson. *Physical Rewiew*, 159:61, 1967.

[Jud90] S.M. Judge, B. Krusche, K. Schreckenbach, H. Tsertos, and P. Kienle. Search for long-lived neutral resonances in Bhabha scattering around 1.8 MeV/c^2. *Physical Review Letters*, 65:972, 1990.

[Kin81] T. Kinoshita and W.B. Lindquist. Eighth-order anomalous magnetic moment of the electron. *Physical Review Letters*, 47:1573, 1981.

[Kin84] T. Kinoshita and et al. *Physical Review Letters*, 52:717, 1984.

[Kin87] Toichiro Kinoshita. The anomalous magnetic moment of the electron and the quantum electrodynamics determination of the fine-structure constant. *IEEE Transactions on Instrumentation and Measurement*, 36:201, 1987.

[Kon86] A. Konaka, K. Imai, H. Kobayahsi, A. Masaike, K. Miyake, T. Nakamura, N. Nagamine, N. Sasao, A. Enomoto, Y. Fukushima, E. Kikutani, H. Koiso, H. Matsumoto, K. Nakahara, S. Ohsawa, T. Taniguchi, I. Sato, and J. Urakawa. Search for neutral particles in electron-beam-dump experiment. *Physical Review Letters*, 57:659, 1986.

[Kra86] Lawrence M. Krauss and Frank Wilczek. A short-lived axion variant. *Physics Letters B*, 173:189, 1986.

[Kum89] Palakkal P.V. Asoka Kumar. *Search for a Particle at 1.8 MeV Through Resonant Bhabha Scattering.* PhD thesis, The City University of New York, 1989.

[Lin91] S. Lindenstruth and et al. *Nuclear Instruments and Methods A*, 300:293, 1991.

[Lor88] E. Lorenz, G. Mageras, U. Stiegler, and I. Huszár. Search for narrow resonance production in Bhabha scattering at center-of-mass energies near 1.8 MeV. *Physics Letters B*, 214:10, 1988.

[Lun71] B.I. Lundqvist and C. Lydén. Calculated momentum distributions and Compton profiles of interacting conduction electrons in Lithium and Sodium. *Physical Review B*, 4:3360, 1971.

[Mai87] K. Maier, W. Bauer, J. Briggmann, H.D. Carstanjen, W. Decker, J. Diehl, V. Heinemann, J. Major, H.E. Schaefer, A. Seeger, H. Stoll, P. Wesolowski, E. Widmann, F. Bosch, and W. Koenig. Experimental limits for narrow lines in the excitation function of positron-electron scattering around $E^* = 620$ keV and $E^* = 810$ keV. *Zeitschrift für Physik A*, 326:527, 1987.

[Mai88a] K. Maier, E. Widmann, W. Bauer, F. Bosch, J. Briggmann, H.-D. Carstanjen, W. Decker, J. Diehl, R. Feldmann, B. Keyerleber, D. Maden, J. Major, H.-E. Schaefer, A. Seeger, and H. Stoll. Evidence for a resonance in positron-electron scattering at 810 keV centre-of-mass energy. *Zeitschrift für Physik A*, 330:173, 1988.

[Mai88b] K. Maier, E. Widmann, W. Bauer, F. Bosch, J. Briggmann, H.-D. Carstanjen, W. Decker, J. Diehl, G. Fabritius, B. Keyerleber, J. Major, H.-E. Schaefer, A. Seeger, and H. Stoll. A study of the e^+e^- interaction in the MeV region. In L. Dorikens-Vanpraet, M. Dorikens, and D. Segers, editors, *Positron Annihilation*, page 171, Singapore, 1988. World Scientific.

[Maz68] Hirmasa Mazaki, Masatsugu Nishi, and Salae Shimizu. Single-quantum annihilation of positrons. *Physical Review*, 171:408, 1968.

[Mil87] A.P. Mills, Jr. and J. Levy. Search for a Bhabha-scattering resonance near 1.8 MeV/c^2. *Physical Review D*, 36:707, 1987.

[Muk79] Takeshi Mukoyama, H. Mazaki, and Sakae. Shimizu. Single-quantum annihilation of positrons with k-shell electrons. *Physical Review A*, 20:82, 1979.

[Mül86] B. Müller, J. Reinhardt, W. Greiner, and A. Schäfer. Is there a tightly bound poly-positronium state? *Journal of Physics G*, 12:L109, 1986.

[Pal91] J.C. Palathingal, P. Asoka-Kumar, K.G. Lynn, Y. Posada, and X.Y. Wu. Single-quantum annihilation of positrons with shell-bound atomic electrons. *Physical Review Letters*, 67:3491, 1991.

[Pec77] R.D. Peccei and Helen R. Quinn. CP conservation in the presence of pseudoparticles. *Physical Review Letters*, 38:1440, 1977.

[Pec86] R.D. Peccei, Tai Tsun Wu, and T. Yanagida. A viable axion model. *Physics Letters B*, 172:435, 1986.

[Pec87a] R. Peckhaus, Th. W. Elze, Th. Happ, and Th. Dresel. Search for peak structure in e^+ + Th collisions. *Physical Review C*, 36:83, 1987.

[Pec87b] R. Peckhaus, T.W. Elze, T. Happ, and T. Dresel. *Physical Review C*, 36:83, 1987.

[Phl93] B.F Phlips. *Resonances in Elastic e^+e^- Scattering.* PhD thesis, Yale University, 1993.

[Rei87] J. Reinhardt, A. Scherdin, B. Müller, and W. Greiner. Resonant Bhabha scattering at MeV energies. *Zeitschrift für Physik A*, 327:367, 1987.

[Rio87] E.M. Riordan, M.W. Krasny, K. Lang, P. de Barbaro, A. Bodek, S. Dasu, N. Varelas, X. Wang, R. Arnold, D. Benton, P. Bosted, L. Clogher, A. Lung,

S. Rock, Z. Szalata, B.W. Filippone, R.C. Walker, J.D. Bjorken, M. Crisler, A. Para, J. Lambert, J. Button-Shafer, B. Debebe, M. Frodyma, R.S. Hicks, G.A. Peterson, and R. Gearhart. Search for short-lived axions in an electron-beam-dump experiment. *Physical Review Letters*, 59:755, 1987.

[Sak88] M. Sakai, Y. Fujita, M. Imamura, K. Omata, S. Ohya, and T. Miura. Electron peaks in e^+ + Th, U and Ta interactions. *Physical Review C*, 38:1971, 1988.

[Sal90] P. Salabura, H. Backe, K. Bethge, H. Bokemeyer, T.E. Cowan, H. Folger, J.S. Greenberg, K. Sakaguchi, D. Schwalm, J. Schweppe, and K.E. Stiebing. Correlated e^+e^- peaks observed in heavy-ion collisions. GSI preprint, 1990.

[Sav86] M.J. Savage, R.D. McKeown, B.W. Filippone, and L.W. Mitchell. Search for a short-lived neutral particle produced in nuclear decay. *Physical Review Letters*, 57:178, 1986.

[Sav88] M.J. Savage, B.W. Filippone, and L.W. Mitchell. New limits on light scalar and pseudoscalar particles produced in nuclear decay. *Physical Review D*, 37:1134, 1988.

[Sch83] J. Schweppe, A. Gruppe, K. Bethge, H. Bokemeyer, T. Cowan, H. Folger, J.S. Greenberg, H. Grein, S. Ito, R. Schule, D. Schwalm, K.E. Stiebing, N. Trautmann, P. Vincent, and M. Waldschmidt. Observation of a peak structure in positron spectra from U+Cm collisions. *Physical Review Letters*, 51:2261, 1983.

[Sch85] J. Schweppe. *A Search for Spontaneous Positron Production in Heavy Ion-Atom Collisions.* PhD thesis, Yale University, 1985.

[Sch86] A. Schäfer, J. Reinhardt, W. Greiner, and B. Müller. Elementary light neutral bosons: New limits from precision experiments. *Modern Physics Letters A*, 1:1, 1986.

[Sch88a] Andreas Schäfer. Bremsstrahlung production of light extended particles. *Physics Letters B*, 211:207, 1988.

[Sch88b] P.J. Schultz and K.G. Lynn. Interaction of positron beams with surface, thin files, and interface. *Rev. Mod. Phys.*, 60:701, 1988.

[Sch89] A. Schäfer. New particles in strong fields? *Journal of Physics G*, 15:373, 1989.

[Sch91] A. Scherdin, J. Reinhardt, W. Greiner, and B. Müller. Low-energy e^+e^- scattering. *Pep. Prog. Phys.*, 54:1, 1991.

[Sie65] Kai Siegbahn. *Alpha-, Beta- and Gamma-Ray Spectroscopy.* North-Holland Publishing Company, Amsterdam, 1965.

[Suz81] T. Suzuki and H. Nagasawa. X-Ray Compton profile of Lithium in low momentum transfer region. *Journal of Physics C*, 14:783, 1981.

[Tan73] B.W. Tan. The influence of electron correlation and crystal structure on the Compton profiles of Lithium, Sodium and Potassium. *Journal of Physics F*, 3:1716, 1973.

[Tsa86] Yung Su Tsai. Axion bremsstrahlung by an electron beam. *Physical Review D*, 34:1236, 1986.

[Tse72] H.K. Tseng and R.H. Pratt. Comments on screening and shell-ratio effects in single-quantum pair annihilation. *Physical Review A*, 7:1423, 1972.

[Tse88a] H. Tsertos, C. Kozhuharov, P. Armbruster, P. Kienle, B. Krusche, and K. Schreckenbach. Sensitive search for neutral resonances in Bhabha scattering around 1.8 MeV/c^2. *Physics Letters B*, 207:273, 1988.

[Tse88b] H. Tsertos, C. Kozhuharov, P. Armbruster, P. Kienle, B. Krusche, and K. Schreckenbach. New limits for resonant Bhabha scattering around the invariant mass of 1.8 MeV/c^2. *Zeitschrift für Physik A*, 331:103, 1988.

[Tse89] H. Tsertos, C. Kozhuharov, P. Armbruster, P. Kienle, B. Krusche, and K. Schreckenbach. High-sensitivity measurements of the excitation function for Bhabha scattering at MeV energies. *Physical Review D*, 40:1397, 1989.

[Wan87] T.F. Wang, I. Ahmad, S.J. Freedman, R.V.F. Janssens, and J.P. Schiffer. Search for sharp lines in $e^+ - e^-$ coincidences from positrons on Th. *Physical Review C*, 36:2136, 1987.

[Wid91] W. Widmann, W. Bauer, S. Connel, K. Maier, A. Seeger, H. Stoll, and F. Bosch. Limits for tow-photon and e^+e^- decay wodths of positron-electron scattering resonances for $\sqrt{s} = 1.78$ to 1.92 mev. *Zeitschrift für Physik A*, 340:209, 1991.

[Wil78] F. Wilczek. Problem of strong P and T invariance in the presence of instantons. *Physical Review Letters*, 40:279, 1978.

[Wim87] U. Wimmersperg, S.H. Connell, R.F.A. Hoernlé, and E. Sideras-Haddad. Observation of Bhabha scattering in the center-of-mass kinetic-energy range 342 to 845 keV. *Physical Review Letters*, 59:266, 1987.

[Wu90] X.Y. Wu, P. Dull, and K.G. Lynn. Enhanced slow positron reemission with new thin foil moderator geometry. *Appl. Phys. Lett.*, 57:10, 1990.

[Wu92] X.Y. Wu, P. Asoka-Kumar, J.S. Greenberg, S.D. Henderson, H. Huomo, K.G. Lynn, M.S. Lubell, R. Mayer, J. McDonough, B.F. Phlips, and A. Vehanen. Search for low-mass states in elastic e^+e^- scattering. *Physical Review Letters*, 69:1729, 1992.